Imperial College London

Investigation of Controlled Salinity Waterflooding Mechanisms in Carbonate Rocks using Micro-Computed Tomography

Ahmed Moustafa Mohamed Selem

A doctoral thesis submitted in fulfilment of the requirements for the degree of

Doctor of Philosophy

of

Imperial College London

March 2023

Statement of Originality

I declare that this thesis work, which is entitled "Investigation of Controlled Salinity Waterflooding Mechanisms in Carbonate Rocks Using Micro-Computed Tomography", has been completed by myself and under the supervision of Prof. Martin J. Blunt and Dr. Branko Bijeljic. This work has been performed, analysed and written at Imperial College London in the Department of Earth Science and Engineering. Full acknowledgement has been made to any cited work in this thesis. This work has not been previously submitted, in whole or in part, to any other academic institution for a degree, diploma, or any other qualification.

Ahmed M. Selem

Department of Earth Science and Engineering

Imperial College London

Copyright Declaration

Ahmed M. Selem

Department of Earth Science and Engineering

Imperial College London

Dedication

This PhD thesis is dedicated to:

My beloved father and mother

My beloved wife, Sonia

My children, Yusuf, Laila and Aya

My brothers and sister

Supervisors - Prof. Martin Blunt and Dr. Branko Bijeljic.

Colleagues

Friends

Humanity

Acknowledgments

"This is by the grace of my lord" – Quran [27:40]

I am ever so grateful to my supervisors, Prof. Martin J. Blunt and Dr Branko Bijeljic for their invaluable and continuous guidance and support from the very beginning of my PhD journey.

I am also grateful to my sponsor TotalEnergies for their generous contribution. I would like to extend my sincere thanks to Dr Nicolas Agenet, my industrial supervisor, Richard Rivenq and Alexandra Klimenko for their precious advice and guidance.

I am also extremely thankful for my Imperial College colleagues and Alumni for their support throughout the journey, especially, Dr Abdulla Alhosani, Dr Amer Alhammadi, , Dr Ying Gao Dr Alessio Scanziani, Dr Qingyang Lin, Dr Ali Raeini, Dr Sajjad Foroughi and Dr Guanglei Zhang.

I would also like to thank my examiners Prof. Matthew Jackson and Dr Yukie Tanino for dedicating their time and expertise to assess my work and provide valuable feedback.

Finally, I would like to take this opportunity to thank my number one supporter, my family, especially my parents, who inspired me to go down this path, and my wife who has been very patient and supportive. Their belief in me kept my spirit and motivation high throughout my journey.

Abstract

Low salinity waterflooding can improve oil recovery from reservoir rocks by changing the wettability from oil-wet towards more water-wet conditions. To investigate the underlying mechanisms of this process, high-resolution X-ray imaging combined with high-pressure and temperature flow apparatus were used to compare secondary and tertiary low salinity waterflooding in carbonate rock samples. Two different crude oil, brine, and rock (COBR) systems were examined.

In the experiments on Estaillades quarry limestone, low salinity waterflooding caused a decrease in average contact angle to 102°, indicating a wettability change from oil-wet to more water-wet conditions. The shift in mean curvature and capillary pressure to positive values further supported this change. Micro-droplets of water were observed within the oil phase and oil layers detached from the rock surface after tertiary low salinity waterflooding. Similar mechanisms were observed in the secondary low salinity waterflooding experiment, with a faster pace and recovery of 85% of the oil initially in place in the resolved porosity. Pore and throat occupancy analysis revealed a redistribution of fluids as more brine was injected.

In the experiments on a reservoir limestone with another crude oil, emulsification of oil was observed with the injection of reduced salinity brine. An intermediate phase that appeared to be a mixture of oil and brine was imaged when low salinity brine was injected, and more emulsification was observed when only low-salinity brine was injected initially. The formation of this intermediate phase is the mechanism by which the oil is mobilized.

Overall, the analysis captured the *in situ* mechanisms and processes associated with the low salinity effect and ultimate increase in oil recovery. The study found that improved recovery

was associated with a change in contact angle and pore occupancy, as well as the formation of micro-dispersions of water in oil and the emulsification of oil.

List of Publications

Journal Articles and Chapters

1. **Selem, A.M.**, Agenet, N., Gao, Y., Raeini, A.Q., Blunt, M.J., Bijeljic, B., 2021. Pore-scale imaging and analysis of low salinity waterflooding in a heterogeneous carbonate rock at reservoir conditions. Scientific Reports, 11(1):15063
2. **Selem, A.M.**, Agenet, N., Blunt, M.J., Bijeljic, B., 2022. Pore-scale processes in tertiary low salinity waterflooding in a carbonate rock: micro-dispersions, water film growth, and wettability change. Journal of Colloid and Interface Science, 628, 486-498
3. **Selem, A.M.**, Agenet, N., Foroughi, S., Blunt, M.J., Bijeljic, B., 2023. Pore-scale imaging of emulsification of oil during tertiary and secondary low salinity waterflooding in a reservoir carbonate. Energy & Fuels, 37 (21), 16368-16377
4. **Selem, A.M.,** Agenet, N., Blunt, M.J., Bijeljic, B., 2023. Formation of Water Micro-Dispersion in Oil as a Mechanism for Efficient Displacement in Low Salinity Waterflooding. In: Médici, E.F., Otero, A.D. (eds) Album of Porous Media. Springer, Cham

Contributed Publications

1. Gao, Y., Raeini, A.Q., **Selem, A.M.**, Blunt, M.J., & Bijeljic, B., 2020. Pore-scale imaging with measurement of relative permeability and capillary pressure on the same reservoir sandstone sample under water-wet and mixed-wet conditions. Advances in Water Resources, 146, 1-18.
2. Alhosani, A., Scanziani, A., Lin, Q., **Selem, A.M.**, Pan, Z., Blunt, M.J. and Bijeljic, B., 2020. Three-phase flow displacement dynamics and Haines jumps in a hydrophobic porous medium. Proceedings of the Royal Society A, 476(2244), p.20200671.

3. Alhosani, A., **Selem, A.M.**, Lin, Q., Bijeljic, B. and Blunt, M.J., 2021. Disconnected Gas Transport in Steady-State Three-Phase Flow. Water Resources Research, 57(12), p.e2021WR031147.

4. Alhosani, A., **Selem, A.M.**, Foroughi, S., Bijeljic, B. and Blunt, M.J., 2021. Steady-state three-phase flow in a mixed-wet porous medium: A pore-scale X-ray microtomography study. Advances in Water Resources. 2023;172:104382.

Conference Proceeding Papers

1. **Selem, A.M.**, Agenet, N., Blunt, M.J., Bijeljic, B., 2021. Pore-Scale Imaging of Tertiary Low Salinity Waterflooding in a Heterogeneous Carbonate Rock at Reservoir Conditions. SPE Annual Technical Conference and Exhibition; 2021. D031S059R003.

2. **Selem, A.M.**, Agenet, N., Gao, Y., Lin, Q., Blunt, M.J., Bijeljic, B., 2021. Pore-Scale Imaging of Controlled-Salinity Waterflooding in a Heterogeneous Carbonate Rock at Reservoir Conditions. 82nd EAGE Annual Conference & Exhibition; Oct 2021, Volume 2021, p.1 - 5.

3. **Selem, A.M.**, Agenet, N., Blunt, M.J., Bijeljic, B., 2022. Observations of water-in-oil micro-dispersions as a displacement mechanism in secondary and tertiary low salinity waterflooding. Fourth EAGE WIPIC Workshop, Mar 2022, Volume 2022, p.1 - 4.

Conference Proceedings

1. **Selem, A.M.**, Agenet, N., Gao, Y., Raeini, A. Q., Lin, Q., Blunt, M.J., Bijeljic, B. Pore-Scale Imaging of Controlled-Salinity Waterflooding in a Carbonate Rock at Reservoir Conditions. Interpore Online 2020.

2. **Selem. A.M.**, Gao, Y., Raeini, A. Q., Bijeljic. B., Blunt. M.J. Comparison between secondary and tertiary low salinity waterflooding in carbonates: pore-scale processes, wettability changes and recovery. Interpore. Online 2021. (Poster Presentation)

3. **Selem. A.M.**, Gao, Y., Raeini, A. Q., Bijeljic. B., Blunt. M.J. Pore-Scale Imaging of Tertiary Controlled-Salinity Waterflooding in a Heterogeneous Carbonate Rock at Reservoir Conditions. Interpore. Abu Dhabi, UAE 2022.

4. **Selem, A.M.**, Agenet, N., Blunt, M.J., Bijeljic, B. Investigation of Low Salinity Waterflooding in Carbonates: Using Pore-Scale Imaging to Capture Recovery Mechanisms and Characterize Wettability. Gordon Research Conference on Flow and Transport in Permeable Media. Les Diablerets, Switzerland 2022. (Poster Presentation)

5. Bijeljic, B., Alhosani, A., **Selem, A.M.**, Oliveira, R. and Blunt, M.J. Imaging and Modeling of Multiphase Flow and Reactive Transport in Geological Storage and Oil Recovery. AGU Fall Meeting. New Orleans, USA 2021.

6. Alhosani. A., Scanziani. A., Lin. Q., **Selem. A.M.,** Alhammadi. A., Foroughi. S., Bijeljic. B., Blunt. M.J. Optimizing Carbon Dioxide Storage in Oilfields at the pore-scale. In *Interpore 2021*.

Nomenclature

Symbol	Description	SI unit
q	Darcy velocity	$m.s^{-1}$
g	Acceleration due to gravity	$m.s^{-2}$
K	Absolute Permeability	m^2
μ	Viscosity	Pa.s
ρ	Density	$kg.m^{-3}$
Q	Volumetric flow rate	$m^3.s^{-1}$
A	Area	m^2
L	Length	m
x	Distance	m
σ	Interfacial tension between *w* and *nw* phases	$N.m^{-1}$
P_c	Capillary pressure	Pa
κ	Total curvature	m^{-1}
κ_m	Mean curvature (κ/2)	m^{-1}
r	Radius of curvature	m
k_r	Relative permeability	
Ca	Capillary number	
I	Transmitted beam intensity	
I_o	Incident beam intensity	
μ_x	Linear attenuation coefficient	m^{-1}
t	Thickness	m
a	Specific surface area	m^{-1}
θ	Contact angle	Degrees

ΔP	Pressure drop across the system	Pa
ϕ	Porosity	
S	Saturation	
CT	Grey-scale peak value	
PV	Pore volume	mL
T	Temperature	^{o}C
P	Pressure	Pa

Table of Contents

List of Tables

List of Figures

Chapter 1

Introduction

In this chapter, we will discuss the rationale for choosing low salinity waterflooding in carbonate rocks as the subject of this PhD research. The chapter starts by addressing the importance of hydrocarbons as a source of energy in the world. Then, it describes controlled salinity waterflooding as an enhanced oil recovery (EOR) technique which can be deployed to extract additional oil from reservoirs. Moreover, the significance of combining this technique with other methods such as CO_2 injection is highlighted. Furthermore, it emphasizes the need for better understanding of the pore-scale physics during low salinity waterflooding which can be achieved by using recent advances in X-ray imaging and image analysis. Finally, the chapter outlines the unique contributions of this PhD study, which uses pore-scale X-ray imaging, and provides the structure of the thesis.

1.1 Hydrocarbons, carbonates, and energy demand

Hydrocarbons comprise the world's main source of primary energy. The uses of hydrocarbons are not only limited to providing a fuel that can be converted into energy but, through refining, petroleum provides a wide range of derivative materials that play critical roles in the world economy, such as plastics, solvents and lubricants. Even if all machinery were to switch into using renewable energy today, hydrocarbon extraction would still be required for these derivative products. One of the scenarios suggested by the International Energy Agency (IEA) in its World Energy Outlook report shows a continuous demand for oil and gas (Figure 1.1) based on the current policy settings stated by governments (IEA, 2022). Moreover, with the increase in global demand for energy and derivative products, and the decline in hydrocarbon reserves, technology to enhance and increase production from

oil resources is becoming increasingly important. Moreover, the need to improve efficiency and reduce carbon emissions with production operations is more urgent than ever. Hence the need to understand the processes that control fluid flow and distribution in reservoir rocks, especially in carbonate reservoirs. These reservoirs are critical for the current and future production of hydrocarbons as they host nearly half of the world's conventional oil and gas reserves (Knebel and Rodriguez-Eraso, 1956, Burchette, 2012, Akbar et al., 2000). This can be achieved by conducting advanced research studying complex reservoir systems at the pore-scale. The objective of such research is to characterise these complex reservoirs and help design reservoir management plans to enhance oil production from existing fields.

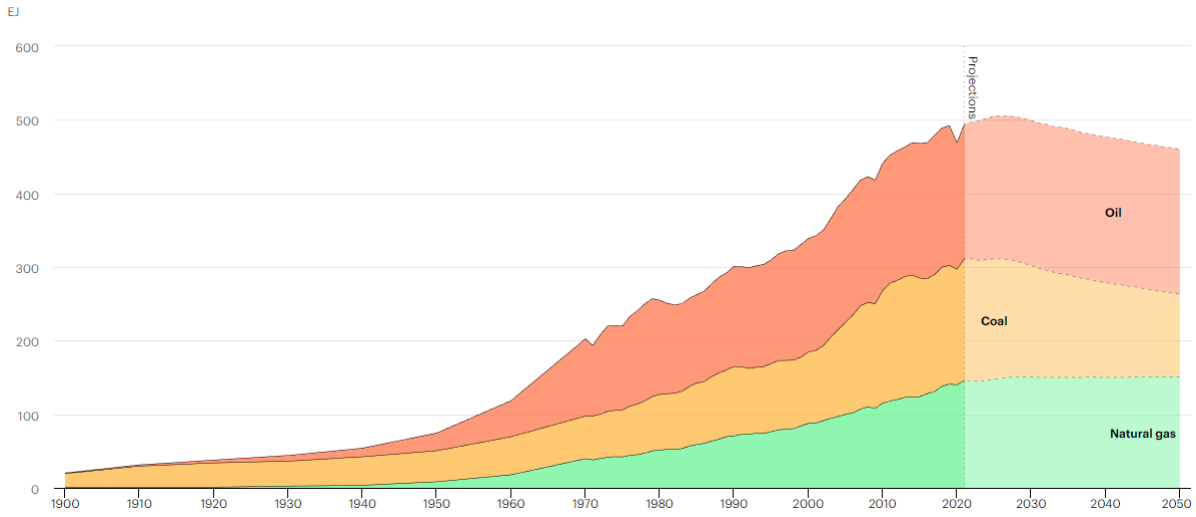

Figure 1.1: Fossil fuel demand based on the trajectory implied by today's policy settings as suggested in the World Energy Outlook report by the IEA (*IEA, Fossil fuel demand in the Stated Policies Scenario, 1900-2050, IEA, Paris https://www.iea.org/data-and-statistics/charts/fossil-fuel-demand-in-the-stated-policies-scenario-1900-2050, IEA. Licence: CC BY 4.0*).

The number of mature oil fields is growing globally, and the output from these fields is decreasing because standard oil recovery from primary production and waterflooding is a rather inefficient process that leaves more than half of the oil reserves unrecovered in the reservoir. The average recovery factor from mature oil fields is between 20% and 40% (Sandrea and Sandrea, 2007). Improving the oil recovery from mature basins has been an area of great interest especially with the new discoveries are becoming smaller and less frequent (Muggeridge et al., 2014).

1.2 Enhanced oil recovery (EOR) and low/controlled salinity waterflooding

The oil field, throughout its lifetime, goes through several recovery stages, namely primary, secondary and tertiary recovery. At the early stage in some fields, oil flows to the surface by one or combination of natural driving mechanisms including pressure decline, the influx of water from the underlying aquifer, gas cap expansion or the release of dissolved gas. After a certain period of oil production by primary recovery mechanisms, reservoir pressure drops due to the depletion in drive energy and the production could then become uneconomic. To address this, water or gas can be injected to displace oil and maintain pressure. This is the secondary recovery stage which relies mainly on physical displacement to recover additional oil. Applying only these two recovery stages can still leave up to 80% of the oil reserves in the reservoir (Muggeridge et al., 2014). Once the water and/or gas injection does not result in any further oil production, a variety of tertiary methods can then be utilised. These methods fall into three main categories: thermal recovery, chemical flooding, and miscible displacement. A more common name for secondary/tertiary recovery is enhanced oil recovery (EOR). Unlike the secondary recovery techniques, EOR methods entail altering the interaction between the reservoir fluids and rock as well as the crude oil properties. Conventional EOR processes include waterflooding, gas injection, water alternating gas (WAG) injection, chemical flooding with surfactants or alkalis, polymer injection and thermal steam injection (Muggeridge et al., 2014).

EOR techniques have been widely studied. A portfolio of new EOR technologies has made it possible to reach high recovery factors, e.g. ultimate recoveries between 50% and 70% have been achieved in some oil fields in the UKCS (Toole and Grist, 2003) which is significantly higher than the global average of 35%. The potential for EOR is remarkable as EOR is considered the new frontier in the redevelopment of existing oil fields (Bin Selamat et al., 2008). The key to realising this potential lies within the various EOR methods which can be applied at any stage within the oilfield lifecycle and, if technically and economically feasible, they have the potential to be used globally.

Waterflooding is the most used secondary production process. It is widely implemented in oil fields to maintain reservoir pressure and improve oil recovery (Craig, 1971). Large carbonate oil reservoirs in the Middle East and the North Sea are flooded with seawater to maintain reservoir pressure and sweep oil to the producing wells. Injecting seawater, for offshore fields, or re-injecting formation brine, for onshore fields, may still leave behind a significant residual oil saturation (Mahani et al., 2011). It was discovered that desalinating the injected brine can further improve the oil recovery (Morrow et al., 1998, Tang and Morrow, 1997, Tang and Morrow, 1999). The commonly used term for this process is low salinity waterflooding (LSW) due to the reduced salinity and/or ionic composition of the formation water in the reservoir. The impact associated with this process in terms of changes to the reservoir rock and crude oil is termed the low salinity effect (LSE).

Early experiments found that changing the salinity of the injected brine can have an impact on oil recovery. Tang and Morrow (1997) have reported an increase in crude oil recovery by flooding low-salinity brine through a Berea sandstone core sample. Morrow and co-workers explored the potential of this promising technique (Jadhunandan and Morrow, 1995b, Morrow et al., 1998, Tang and Morrow, 1999) and initiated the interest in this research area. Further research studies discussed the various LSW mechanisms and LSE (Dang et al., 2013, Jackson et al., 2016b, Derkani et al., 2018, Tetteh et al., 2020). In addition to the research and experimental work conducted in the last decade, some field trials have also shown that modifying the composition of the injected brine can increase oil recovery from carbonate reservoirs (Seccombe et al., 2008). Al-Attar et al. (2013) conducted a LSW experiment on carbonate core samples extracted from a field in the UAE. Various dilutions and compositions of seawater, as well as field injection waters, were used to examine the effect of altering the brine salinity and composition on wettability and most importantly on oil recovery. An increase in oil recovery during waterflooding was recorded.

It is now widely acknowledged that reducing injected brine salinity is not the only way to observe the LSE. Academic and industrial research have been exploring various processes to enhance recovery by introducing different types of additives to the injected water. By adjusting the ionic composition or the concentration of particular ions, or even increasing the overall salinity or ionic strength of the injection

brine, enhanced oil recovery can still be achieved. Considering these findings, the process is frequently referred to more broadly as "controlled salinity waterflooding (CSW)" or "modified salinity waterflooding (MSW)". Oil companies have shown interest in further developing this technique. This EOR method is also known as LoSal^{TM}, by BP, Smart Water Injection Methods (SWIM), by TotalEnergies, Designer Waterflood, by Shell, and Smart WaterFlood, by Saudi Aramco. In this research the term LSW will be used more often for simplicity and consistency and to show the contrast with high salinity waterflooding (HSW), which is also studied in this project.

LSW can be conducted in two modes: (i) secondary mode which depicts the injection of low salinity brine directly after primary depletion, and (ii) tertiary mode in which a secondary waterflood of high salinity brine (seawater or formation brine) precedes the low salinity brine injection. In this project, we will investigate both recovery modes at the pore scale to understand the physics behind oil recovery and compare the two methods in terms of performance. Further literature review on this topic is presented in Chapter 2.

1.3 Low salinity waterflooding (LSW) as a competitive EOR method

Low salinity waterflooding has several advantages over other EOR methods. It has relatively low cost and environmental impact compared to other chemical-based methods. In an exemplar study, a screening tool was developed by the Norwegian Petroleum Directorate, in partnership with Imperial College, trying to map and assess the possible EOR potential for 53 reservoirs belonging to 27 oil fields on the Norwegian Continental Shelf (NCS). The most attractive processes are identified as low salinity with polymer, surfactant with polymer, and the injection of miscible hydrocarbon (HM) and CO_2 water alternating gas (WAG) (Smalley et al., 2018). In this study a new approach was applied to 14 EOR processes across 85 reservoirs from 46 oil fields and discoveries on the offshore. The expanded analysis has evaluated how factors besides subsurface parameters can impact EOR projects and is based on reservoir data provided by operators. The screening was expanded to capture operational, environmental, and economic criteria (Figure 1.2). When considering these criteria, the overall potential

recovery increment was reduced from 698 to 282 million standard cubic metres, leaving the most promising processes as HC miscible, low salinity/polymer, low salinity, CO_2 miscible, and gels (Smalley et al., 2020). The results of the study gave low salinity a high environmental score. Low salinity, along with gas injection, were believed to have negligible pollution effects. Moreover, low salinity, when combined with polymer, could have a positive effect in reducing CO_2 emission per unit volume of oil produced.

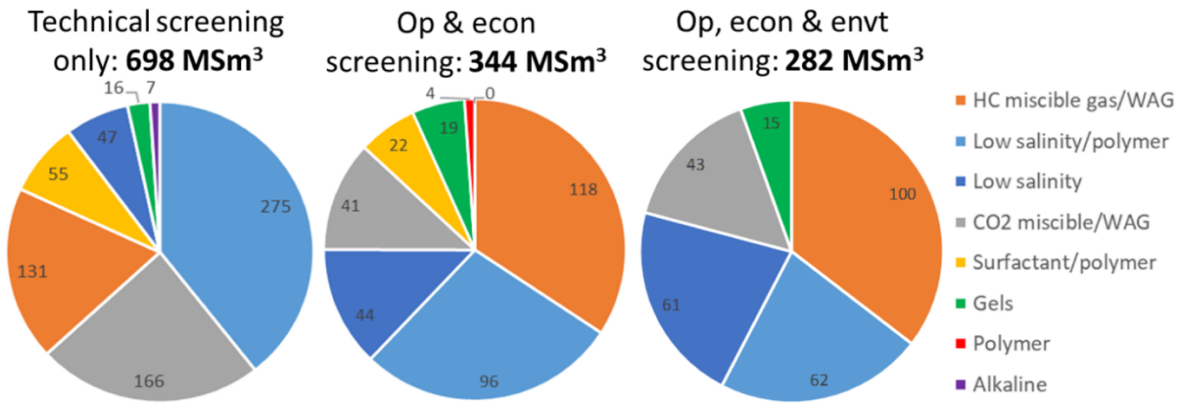

Figure 1.2: The NCS EOR potential incremental oil volumes (MSm³ is million standard cubic metres). The first chart displays the results of technical screening only, without considering advanced screening factors. The second chart displays the results of advanced screening, taking into account only operational and economic factors. The third chart shows the results of advanced screening, considering operational, economic, and environmental factors. The numbers in each sector indicate the incremental volumes for each process. The middle and right-hand charts have these volumes multiplied by the Feasibility Factor, which adjusts the volumes to account for the likelihood of implementation, as in Smalley et al. (2020).

The North Sea is a well-established oil-producing region where many of the oilfields are close to the end of their profitability. For every barrel of oil produced, approximately 9 barrels of water must be extracted in some cases (Walsh, 2015), which requires significant energy. The energy is needed to bring the water and oil to the surface from depths of thousands of metres beneath the ocean floor, as well as to inject water into the oilfields to maintain pressure and help extract the oil from the rock formations. Therefore, more efficient and economically viable methods need to be developed.

In this work, in agreement with some previous studies (Morrow et al., 1998, McGuire et al., 2005, Seccombe et al., 2008, Morrow and Buckley, 2011, Yousef et al., 2012a, Nasralla et al., 2016), low salinity waterflooding results showed higher efficiency than conventional waterflooding, i.e., higher oil

recovery for the same amount of water injected. In addition to the increase in efficiency, LSW could potentially reduce the CO_2 intensity of the waterflooding process by reducing the invested energy spent on injection and lift pumps compared to other EOR applications such as polymer and surfactant flooding (Farajzadeh et al., 2021).

1.4 CO_2 - Low Salinity Water alternating Gas EOR

One of the tertiary recovery methods, highlighted previously, in section 1.2, is miscible injection in which a miscible fluid is injected in the subsurface to displace the remaining oil. Supercritical CO_2 is deployed to improve oil recovery by dissolving in and hence reducing the oil viscosity, this process is known as CO_2-EOR. Around 140 operating CO_2-EOR projects are producing approximately an additional 100 million barrels of oil per year globally (Bui et al., 2018). However, in most of these projects, the main objective is to enhance oil production and little thought is given to the entrapment of CO_2. These projects could store around 75 million tonnes of captured carbon dioxide per year. Carbon capture and storage (CCS) is one of the most promising technologies that can mitigate global warming. The oil and gas industry has pioneered the development and deployment of CCS and this has been driven by combining CCS and EOR in one process. In this process, the CO_2 injected to displace the remaining oil will be residually trapped and permanently stored in the oil reservoir (Mungan, 1981, Van Poollen, 1980).

The Weyburn project is the first project in Canada with the primary objective of injecting CO_2 for additional oil recovery as well as for carbon sequestration to help mitigate climate change. Scottish Carbon Capture & Storage (SCCS), the Scottish Government, and other companies have been investigating the possible application of CCS-EOR in the North Sea. If applied in the North Sea, CCS-EOR has the possibility to improve oil production and store large amounts of captured CO_2 in offshore oil fields (Sweatman et al., 2011). It is estimated that there is the potential to recover 24 billion barrels of additional oil in the North Sea alone using the CO_2-EOR process (El-Hoshoudy and Desouky, 2018). Preliminary work and several studies have examined the possibility and potential of combining LSW

and CO_2 flooding as an efficient EOR method to increase recovery and store CO_2 (Teklu et al., 2017, Wilson, 2015, Dang et al., 2016, AlQuraishi et al., 2019). The results showed that CO_2 low salinity water-alternating-gas (CO_2 LSWAG) injection combines the various mechanisms associated with these methods including wettability alteration, ion-exchange, and CO_2 miscible displacement. This multi-mechanism process can result in oil recovery enhancement as well as CO_2 entrapment. Dang et al. (2014) proposed a novel concept comprising CO_2 LSWAG injection. The simulation results from this study showed that CO_2-LSWAG has the highest oil recovery compared to conventional high salinity waterflood, high salinity WAG injection, and low salinity waterflood. Since most of the work on LSWAG so far has been numerical and rarely done on carbonates, therefore there is a great opportunity to validate these simulations experimentally as well as produce new observations from LSWAG experiments on carbonate rocks utilising the X-ray micro-CT technology.

1.5 Research motivation and aim

Understanding low salinity waterflooding mechanisms is of key importance for its design yet relatively few studies can be found in the literature that address the pore-scale physics on natural systems at reservoir conditions. This is due to several reasons including (i) the complexity of *in situ* experiments on a natural system in terms of pore geometry and wettability, (ii) the availability of sophisticated experimental equipment capable of providing in-situ observations, and (iii) the acquisition of high-quality three-dimensional X-ray images to distinguish the phases within the pore space. Therefore, even with multiple attempts to address those challenges, there is still a gap in the complete predictive understanding of low salinity waterflooding.

Nonetheless, with the recent development of three-dimensional X-ray microtomography, which allows for the *in situ* visualization of the fluids in the pore space, there is finally a tool which enables a better understanding of low salinity waterflooding pore-scale processes. Although this non-invasive technology has been previously deployed in the context of enhanced oil recovery its scope has been limited. Hence, there is a clear knowledge gap in understanding the physics of low-salinity waterflooding in the literature. We plan to bridge this gap by developing approaches to extend the reach

of this tool and shed light on the underlying mechanisms of low salinity waterflooding by providing direct visualizations of the displacement processes. To achieve this, we will simultaneously combine X-ray imaging with coreflooding in both secondary and tertiary recovery for different crude oil-brine-rock (COBR) systems. Using image analysis, we will make novel observations of the processes during low-salinity waterflooding and support this evidence with quantitative analysis of geometry and wettability. To this end we will use a suite of tools developed by the Pore-scale Imaging and Modelling Group at Imperial College such as differential imaging to characterize microporosity in carbonates and measurements of contact angle, curvature and pore occupancy to provide evidence of change in surface and flow properties.

The aim of this PhD is therefore to use X-ray microtomography to expand on the knowledge of the pore-scale physics that controls LSW in carbonate rocks at reservoir conditions. We mainly focus on the underlying mechanisms and pore-scale processes, which will be visualized, for the first time, using X-ray imaging in this work. The insights from this work are used to advise on the design of the optimal LSW to maximize the amount oil recovery and reduce the amount of water injection and energy consumption in the waterflooding process in oil fields.

1.6 Scientific achievements

We perform four *in situ* waterflooding experiments combined with pore-scale X-ray imaging. These experiments include the preparation of different carbonate rock samples to similar conditions found in oil reservoirs prior to flooding them with brines of different salinities while acquiring static images using a laboratory X-ray scanner at the end of the displacement. To investigate the impact of rock geometry (quarry versus reservoir rock) , wettability and injection mode (secondary versus tertiary) on low-salinity waterflooding we performed four flooding experiments on two different carbonate rocks, quarry and reservoir limestone, using two different crude oils and various brine recipes. Two different formation brine and low salinity brine recipes were used with each rock type whereas the same sea water, or high salinity brine, recipe was used across all experiments. The experiments are highlighted in table 1. More details on the properties of the rocks and fluids used are provided in chapter 3.

Table 1.1: Details of the four experiments performed in this research.

		Crude oil, brine and rock (COBR) system				
Experiment	**LSW mode**	**Rock type**	**Crude oil**	**Formation brine (FB)**	**High salinity brine (HSB)**	**Low salinity brine (LSB)**
1	Tertiary	Quarry	Crude 1	FB1	HSB	LSB1
2	Secondary	Quarry	Crude 1	FB1	-	LSB1
3	Tertiary	Reservoir	Crude 2	FB2	HSB	LSB2
4	Secondary	Reservoir	Crude 2	FB2	-	LSB2

The novelty of those experiments includes:

(i) performing the low-salinity waterflooding experiments on natural systems at conditions representative of oil reservoirs;

(ii) visualizing the pore-scale processes associated such as formation of micro-dispersions and emulsification with reduced salinity waterflooding;

(iii) quantification of wettability change through measurement of contact angle, curvature and pore occupancy as shown in Figure 1.3;

(iv) highlighting the differences between the two LSW modes and the impact on ultimate oil recovery and displacement efficiency;

(v) establishing a combined imaging and quantitative image analysis methodology that can be readily used to establish the most efficient COBR systems and injection modes in design of low-salinity waterflooding.

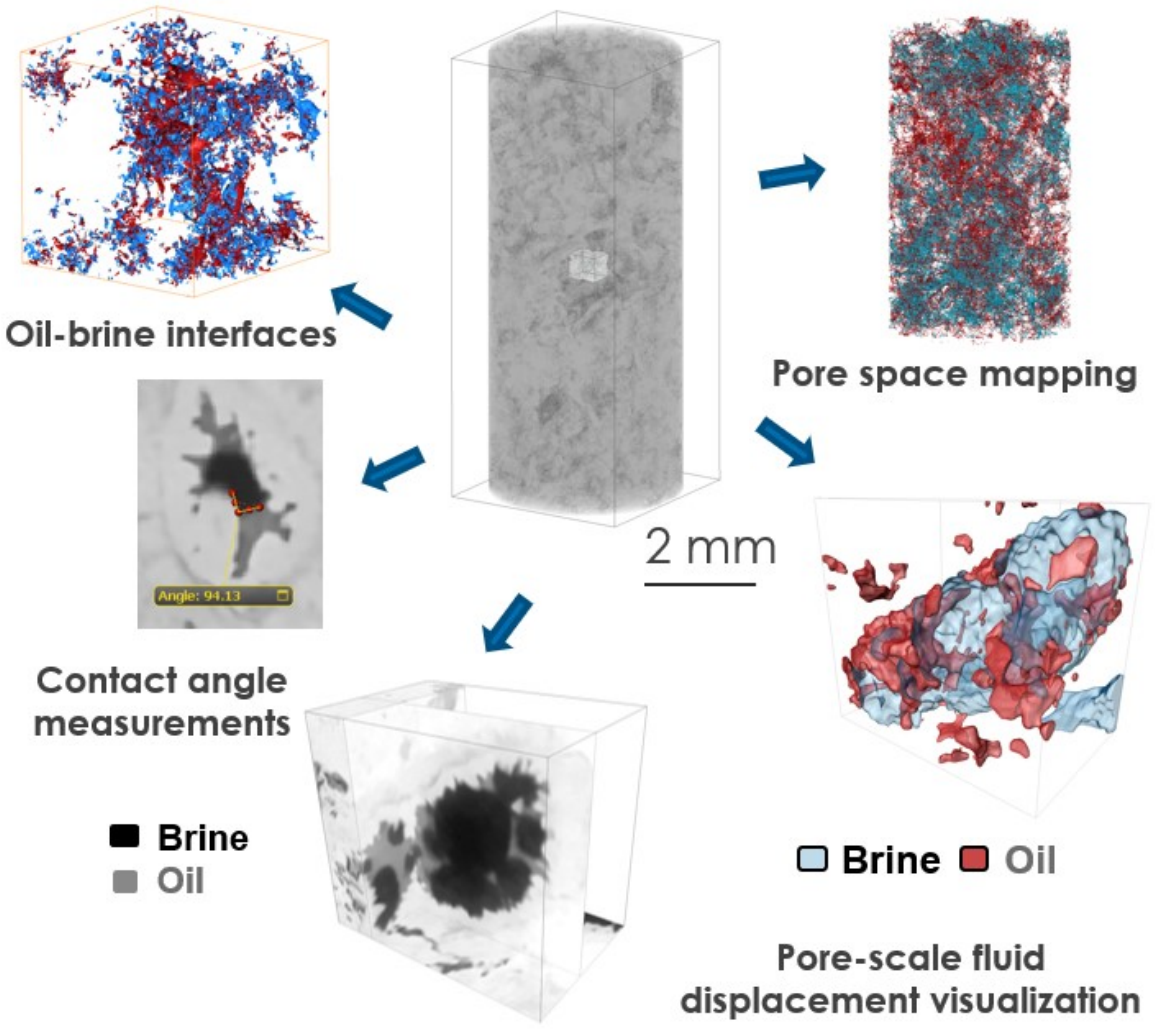

Figure 1.3: Summary of the suite of analyses performed in this work.

This project investigated the underlying LSW mechanisms in carbonates by studying two complex dual-porosity limestone rocks with different geometries. Two different crude oils with physical and geochemical properties and brines with different compositions were used to investigate the impact of fluids properties on the LSE. We injected brine at various steps, flow rates and sequences to build a better understanding of the displacement process associated with high and low salinity waterflooding.

This work will help design the waterflooding process by understanding:

(1) the interactions between oil and brine at the pore-scale;

(2) the variations in LSW response based on the COBR system in question;

(3) understanding the key mechanisms for oil recovery in different injection modes;

(4) the difference in efficiency between the LSW modes and the impact that can have on recovery rates and overall project economics.

1.7 Thesis outline

The thesis is structured as follows:

Chapter 2 describes the underlying concepts of fluid flow in porous media and X-ray imaging followed by a literature review on LSW studies. The importance of our work will be clearly highlighted in the literature review.

Chapter 3 presents the materials used in this work and the experimental methods; flooding procedures, and image acquisition, processing and analysis techniques deployed.

Chapter 4 presents the results, discussion, and conclusions of the tertiary LSW experiment on Estaillades limestone along with displacement processes visualization and wettability characterization elements.

Chapter 5 highlights the secondary LSW results on Estaillades limestone along with discussion and conclusions.

Chapter 6 addresses the results, discussion, and conclusions of the tertiary and secondary LSW experiments on reservoir rocks.

Chapter 7 will highlight the final remarks of this research and suggest topics for future work.

Chapters 4,5 and 6 are based on published work (journal articles) highlighted under the "List of Publications" sections. Ahmed M. Selem is the first author on all three publications contributing to conceptualization, investigation, methodology, formal analysis, visualization, writing- original drafts.

Chapter 2

Scientific background and literature review

The opening section of this chapter will provide an overview of the fundamental physics that govern the movement of fluids in porous media. Subsequently, attention will be given to the current state-of-the-art X-ray imaging technology and its potential application in enhancing our understanding of multiphase flow processes. Section 2.2 will feature a comprehensive review of published research on low/controlled salinity waterflooding, followed by an analysis of the gaps in the literature and how our experiments contribute to addressing these gaps.

2.1 Background theory

In many subsurface applications, comprehending multiphase flow in porous media is crucial. Studies at the pore scale can reveal the fluid flow mechanisms that underlie models at the core and field scales (Blunt et al., 2013). Recent advancements in imaging methods have greatly aided pore-scale research in visualizing pore-by-pore fluid behaviour, generating benchmark data, and offering insight for larger-scale modelling.

This chapter will provide an overview of fundamental concepts of multiphase flow at the pore scale, including a description of the main forces that control multiphase flow in porous media, as well as an introduction to Darcy's law, which governs flow at the larger (or core) scales. We will then examine displacement processes, such as imbibition and drainage, which explain fluid mobility. Additionally, we will explore the principles of mobilization of oil ganglia and describe the flow regimes that X-ray imaging technology has revealed. The section will conclude with a discussion of the Euler characteristic and its use in assessing connectivity of the non-wetting phase.

2.1.1 Multiphase flow in porous media: Interfacial tension, capillary pressure and capillary number

The distribution of fluids in complex pore spaces during the simultaneous flow of multiple fluid phases in porous media is controlled by various forces (Blunt, 2017). The interplay between viscous and capillary pressures governs multiphase flow in porous media. Our focus is on the permeable rock where the concurrent flow of oil and water takes place, and we consider interfacial tension, capillary pressure, and viscous pressure. This section provides further details on these parameters, their definitions, and the factors that affect their characteristics.

Interfacial tension, or surface energy density, is the property of a fluid surface that causes it to minimize its surface area, and it is defined as the energy per unit area of the surface between two phases or the change in free energy, F, for a given area, A, as expressed by the equation $\sigma = dF/dA$. This phenomenon is attributed to the fluid-fluid interface, which maximizes intermolecular bonding within a fluid and minimizes it between dissimilar fluids.

The local capillary pressure or the difference in pressure between two phases at the pore scale is typically defined as the pressure gradient that depends on the equilibrium curvature and interfacial tension. This relationship is expressed by the Young-Laplace equation (Morrow, 1970).

$$P_c = P_0 - P_w \ = \sigma \left(\frac{1}{r_1} + \frac{1}{r_2}\right) \tag{2.1}$$

where P_c [Pa] is the capillary pressure, σ [N/m] is the interfacial tension between the two phases, P_o [Pa] is the pressure in the oil, P_w [Pa] is the pressure in the water phase, and r_1 [m] and r_2 [m] are the principal radii of the curvature of the interface. Suppose we examine a pore or throat with a circular cylinder shape and a radius of r that contains two phases, and the contact angle θ is measured through the denser phase, water. In that case, the capillary pressure can be defined as follows:

$$P_c = \frac{2\sigma}{r} \cos\theta \tag{2.2}$$

The capillary number is a dimensionless ratio between the viscous pressure drop and capillary pressure, and it is utilized to differentiate between flow behaviours. The magnitude of viscous pressures is directly related to the rate of change in fluid velocity within a given space. The capillary number is normally expressed as

$$Ca = \frac{q\mu}{\sigma} \tag{2.3}$$

where q [m/s] is the Darcy velocity, μ [Pa·s] is the viscosity, and σ [N/m] is the interfacial tension.

At low capillary numbers, flow is impeded in narrow throats or small pores due to capillary pressure. An increase in the capillary number represents a rise in relative viscous pressures, compelling oil (the non-wetting phase) to pass through the pore space when water (the wetting phase) is injected. The saturation distribution at the local level is influenced by the balance between viscous and capillary pressures. For instance, the residual oil saturation varies with a change in flow rate (Abrams and Prausnitz, 1975). The capillary number is commonly used to quantify the relative magnitude of viscous and capillary pressures. At reservoir conditions, the typical values for σ_{ow} are in the order of 10^{-3} N/m, and q is about 10^{-6} m/s (Blunt, 2017). Capillary pressures usually dominate the displacement process when $Ca < 10^{-6}$ (Niu et al., 2015), while viscous pressures are dominant when $Ca > 10^{-3}$ (Blunt, 2017). Most natural flows have Ca in the range of 10^{-8} - 10^{-5}, although flows near wells and during miscible flow can have Ca as high as 10^{-3} (Blunt, 2017).

2.1.2 Wettability and contact angle

Wetting forces lead to an equilibrium condition between at least three phases: a solid and two fluids. The wettability of a porous rock is described as the affinity of the rock surface to be in contact with one fluid over another immiscible fluid. In a porous medium saturated with water and oil, water-wet is the case in which the surface of the grain prefers contact with water whereas oil-wet is when the surface prefers contact with oil. Most reservoir rocks have a mix of wetting conditions; the small pores are strongly water wetting whereas the larger pores have a range of wettability from less water wetting to oil wetting (Abdallah et al., 1986). Understanding the wettability of reservoir rocks is essential for oil

recovery optimisation. The rock wetting preferences, (whether oil-wet, water-wet or mixed-wet) have a great impact on the reservoir performance extending from the pore scale to the reservoir scale. The characterization of wettability is typically achieved by examining the contact angle between the grain surface, oil, and water. This angle is dependent on various factors, including mineralogy (Treiber and Owens, 1972, Gomari et al., 2006), formation brine chemistry (Wagner and Leach, 1959, Strand et al., 2006), oil composition (Morrow et al., 1973, Wu et al., 2006), and reservoir temperature (Strand et al., 2006, Zhang and Austad, 2006, Hamouda and Gomari, 2006, Mahani et al., 2017). Wettability is quantified directly by contact angle from 0° (strongly water-wetting) to 180° (strongly oil-wetting). The angle is measurement in the denser, aqueous, phase at the three-phase contact lines (Figure 2.1).

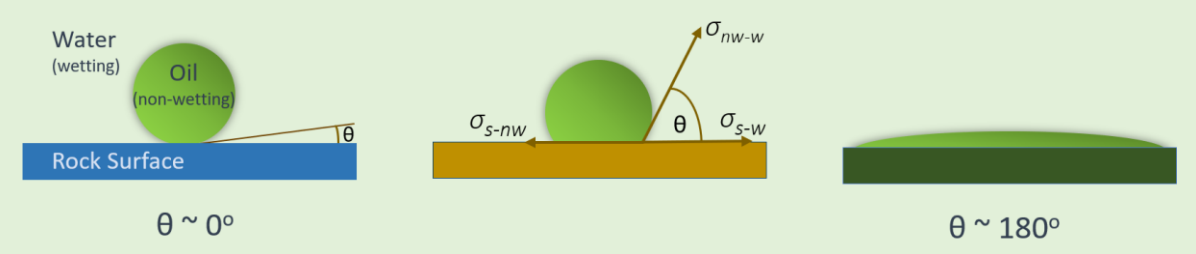

Figure 2.1: Three wettability states in a brine-oil-rock system. Water-wet, neutral-wet, and oil-wet (from left to right). On a strongly water-wet rock surface, the contact angle θ is nearly zero whereas on a strongly oil-wet surface the oil droplet spreads (contact angle is nearly 180°). In the intermediate-wet case, the contact angle is influenced by the balance between the interfacial tensions. From Abdallah et al. (1986).

Wettability is a balance of forces at the interfaces between the different phases described by the interfacial tensions, as shown in Figure 2.1. The interfacial tensions are related by Young's equation:

$$\sigma_{s-o} = \sigma_{s-w} + \sigma_{o-w} \cos\theta \qquad (2.4)$$

where σ_{s-o} is the interfacial tension between solid and oil fluid, (mN/m), σ_{s-w} is the interfacial tension between solid and water (mN/m), σ_{o-w} is the interfacial tension between oil and water fluids, (mN/m), and θ is the contact angle, (degree, °).

In recent times, advancements in high-resolution imaging techniques have resulted in the development of novel approaches to characterize wettability in the pore space. By using microtomography, micro-

CT, imaging, it is now possible to obtain a direct visualization of the pore space and measure the contact angle of the COBR interface on surfaces within the rock under reservoir conditions (Andrew et al., 2014a, Khishvand et al., 2016, Khishvand et al., 2017b, Singh et al., 2016, AlRatrout et al., 2017, Ibekwe et al., 2020). This type of measurement provides a more precise depiction of the contact angle as it considers the geological textures, roughness, and displacement effects that are often absent in ideal flat surfaces. Additionally, it is now possible to measure contact angles at numerous points across multiple pores, further improving the accuracy of the characterization (Klise et al., 2016, AlRatrout et al., 2017, Scanziani et al., 2017, Ibekwe et al., 2020). Figure 2.2 provides a workflow of an automated in situ contact angle measurement (Alhammadi et al., 2017). The contact angle distribution offers a wider view of the wetting behavior of the porous media. Additionally, alterations in the contact angle distribution resulting from changes in system parameters can provide valuable information on the mechanism of wettability alteration. By identifying the specific pores and wetting states that contribute to the overall change in wettability, insights into the mechanism of wettability alteration can be gained.

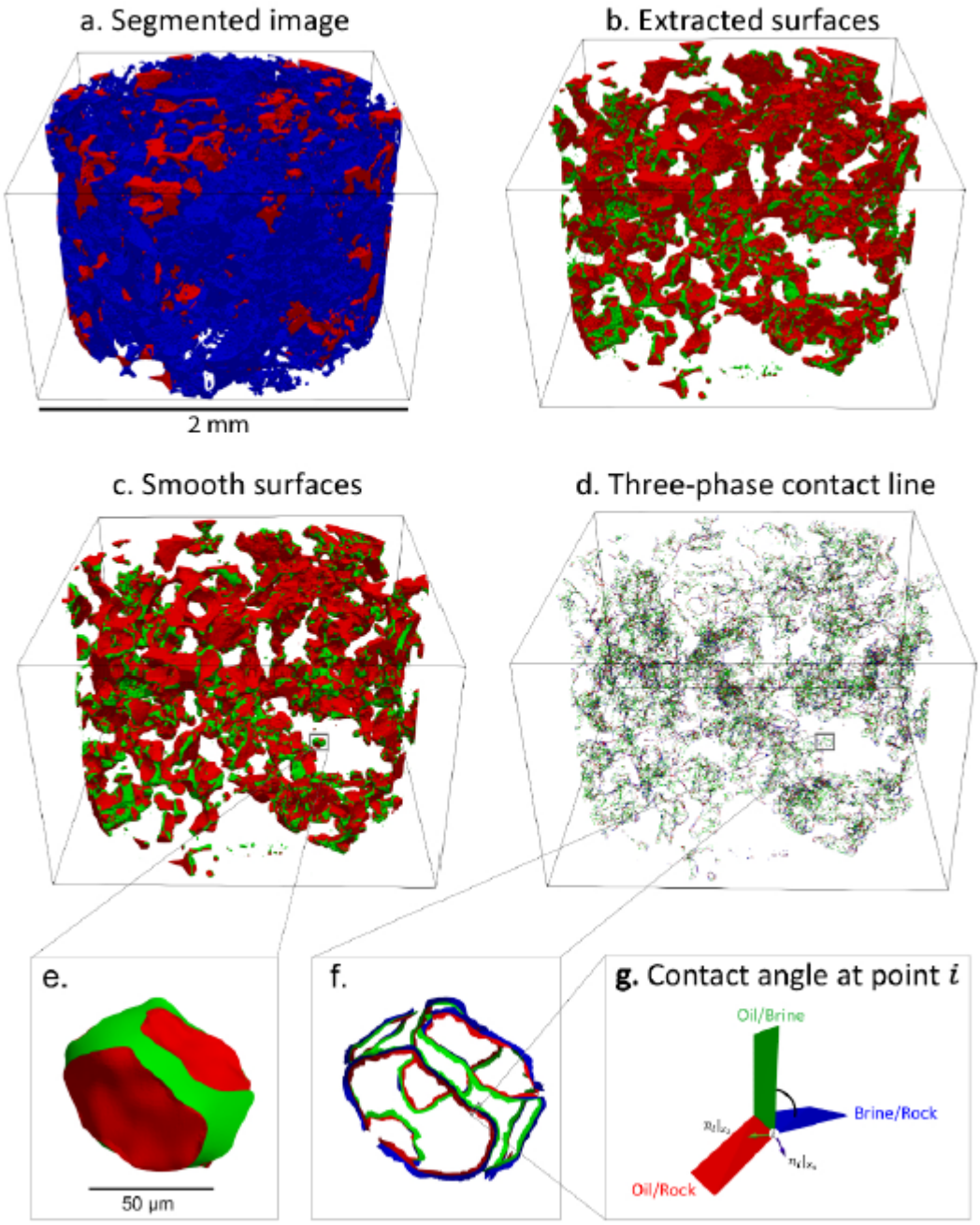

Figure 2.2: Automated *in situ* contact angle measurement workflow from AlRatrout et al. (2017), Alhammadi et al. (2017). (a) The image displays brine in blue and oil in red in a three-dimensional segmented form, while the rock is transparent. (b) The extracted surfaces of the complete image are visible in this panel, where the oil/brine surfaces are green, and the oil/rock surfaces are red. (c) Smoothed surfaces of the entire image are presented in this panel. (d) The three-phase contact line of the whole image is illustrated in this panel. (e) The square highlights an oil ganglion in the smoothed surfaces of the image. (f) The three-phase contact line of the highlighted oil ganglion is shown in this panel. (g)

This panel depicts a single contact angle measured at point i, highlighted in panel f, where the oil/brine, oil/rock, and brine/rock surfaces are colored green, red, and blue, respectively.

2.1.3 Conductivity and trapping

The organization of phases within the pore space, which is influenced by their wettability, has implications for both flow conductivity and trapping. When a phase occupies larger or intermediate-sized pores, it will have greater flow potential compared to occupying smaller pores. However, this assumption requires that the phases are interconnected through the pore space. If a phase exists as a disconnected bubble in the centre of the pores, surrounded by a more wetting phase, it may become trapped due to capillary action. In general, for a fluid phase to become trapped by another phase, it must be less wetting than the surrounding phase. Thus, the phase with the lowest wetting potential could potentially have the highest flow conductivity when it is connected through the wider regions of the pore space. However, it could also have the largest residual saturation if the flow pathways become blocked by more wetting phases.

Tanino and Blunt (2012) investigated the remaining state of waterflooding under low capillary number by utilizing the porous plate technique and estimated the pore coordination number and pore body-throat aspect ratio by using X-ray micro-CT images of sandstone and carbonate rocks. The results showed that the residual saturation diminishes as the porosity increases, and there is no notable contrast in the residual saturation between sandstones and limestones. Moreover, the residual saturation decreases as the conditions become less favourable for snap-off, with declining pore aspect ratio and increasing coordination number. These findings shed light on capillary trapping with implication in EOR and CCS. They indicated that capillary trapping can effectively store carbon dioxide in both sandstones and carbonates, provided that the systems are strongly water wet.

2.1.4 Pore-Scale X-ray Imaging

Flannery et al. (1987) utilized both laboratory and synchrotron X-ray sources to acquire micron-resolution images of a porous rock for the first time. Several leading groups in this area (Iglauer et al., 2010, Andrew et al., 2013, Blunt et al., 2013, Andrew et al., 2014a, Andrew et al., 2014b, Andrew et

al., 2015, Menke et al., 2015, Singh et al., 2016, Alhammadi et al., 2017, AlRatrout et al., 2017, Arns et al., 2005, Jones et al., 2007, Liu et al., 2017, Wildenschild and Sheppard, 2013, Schlüter et al., 2014) adapted more advanced techniques, including in the area of core analysis called digital core analysis. This involves investigating multiphase flow in porous media, especially in rock pore spaces using X-ray microtomography (Blunt, 2017). This non-destructive tool can capture three-dimensional images of processes and variables within the pore space, making it crucial to the study of multiphase flow in various systems such as rocks, batteries, fuel cells, microfluidic devices, etc. Digital core analysis can typically achieve micron resolution at the pore-scale, making it ideal for exploring rock properties and transport phenomena at a representative elementary volume (REV) scale ranging from millimetres to centimetres.

2.1.4.1 X-ray sources and applications

The cutting-edge technique for microtomographic imaging combines synchrotron and laboratory-based facilities. Synchrotron sources emit X-rays by accelerating electrons around a circular ring at almost the speed of light, enabling high-resolution imaging and faster acquisition times. This allows for time-resolved studies with high temporal resolution, making it possible to capture the dynamics of pore-scale displacement during fluid invasion. However, access to these facilities is limited compared to the more accessible and user-friendly laboratory-based facilities.

Although laboratory facilities require longer times to acquire X-ray images, they are still an attractive solution for generating reliable three-dimensional images of pore space. Laboratory-based X-ray microtomography can be used to investigate various pore-scale flow properties such as micro and macro porosity, fluid saturations, interfacial areas, curvatures, pore occupancy, contact angles, layer formation, displacement processes, connectivity, and trapping (Blunt et al., 2013, Cnudde and Boone, 2013, Wildenschild and Sheppard, 2013, Ibekwe et al., 2020). Therefore, in this PhD project, we will employ lab X-ray microtomography in our experiments to gain a comprehensive understanding of LSW.

2.1.4.2 X-ray attenuation

Typically, the creation of a three-dimensional digital image of a rock sample involves a sequence of steps. X-rays are conventionally generated in a highly evacuated glass tube where a high voltage accelerates free electrons between the heated cathode filament and target anode (typically made of tungsten). This interaction between the electrons and the anode produces X-rays. The significance of X-rays arises from their capability to penetrate materials in varying degrees based on their densities. As X-rays traverse the object, the sample image undergoes geometric magnification and is transformed into visible light through a scintillator camera, which is subsequently optically magnified. This sequence yields a single two-dimensional image. Multiple 2D projection images are then captured from various angles as the sample completes a 360-degree rotation. These images are later reconstructed using a computer program to generate a comprehensive 3D model.

Throughout this process, the X-ray beam experiences a reduction in intensity as it passes through the material, and this attenuation follows the Lambert-Beer law. Lambert-Beer law expresses the transmitted intensity *I* of a monochromatic X-ray:

$$I = I_0 \times e^{-\mu x} \tag{2.5}$$

where *I* is the transmitted beam intensity, I_0 is the incident beam intensity, μ is the linear attenuation coefficient and *x* is the thickness of the material, or the length of the X-ray path through the material (Ketcham and Carlson, 2001). If the scanned object is composed of a number of different materials, then the equation becomes:

$$I = I_0 \times e^{\sum_i -\mu_i x_i} \tag{2.6}$$

2.1.4.3 Microcomputed tomography (Micro-CT)

Micro-CT is distinguished from the conventional medical-CT by the rotational movement mechanism. In medical CT, the object (patient) remains stationary while the X-ray source and detector rotate around the object. On the other hand, in micro-CT scanners, the source and detector are fixed, and it is the object that rotates (Figure 2.3). This setup is critical to achieving the mechanical stability necessary for high-resolution imaging. Spatial resolution is the other distinctive feature between both techniques; 200

nm resolution can be achieved by micro-CT but not medical CT scanners. Moreover, the typical sample sizes for micro-CT in geosciences range from less than a millimetre to several centimetres. Lab-based micro-CT is characterised by a standard cone-beam arrangement in which the conical X-ray beam achieves geometrical magnification by positioning the studied object between the X-ray source and detector (Cnudde and Boone, 2013). This way, the highest achievable resolution is mainly limited by the focal spot size of the X-ray source, which is one of the important variables that determine how effective an X-ray source will be for a scanning task.

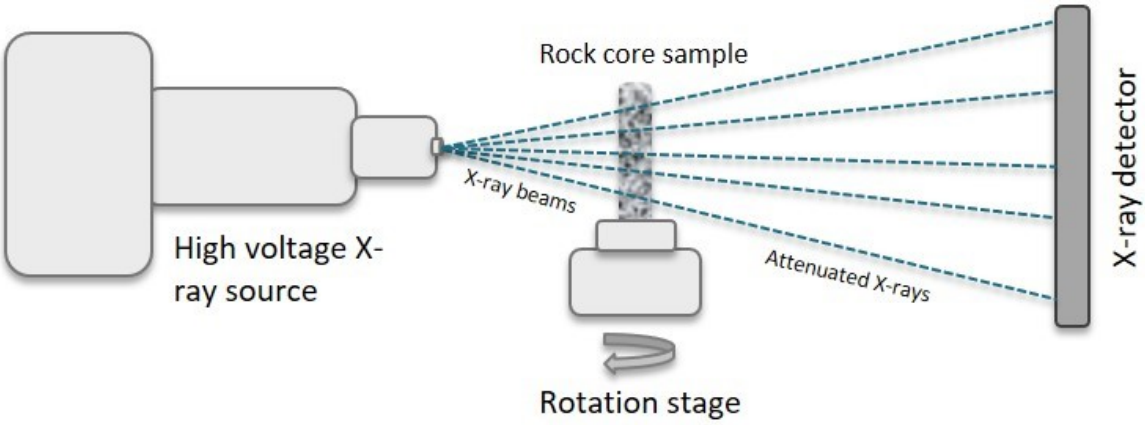

Figure 2.3: Schematic diagram of a basic lab-based conical X-ray beam micro-CT apparatus.

All X-ray sources currently used in micro-CT generate a polychromatic beam which, unlike the monochromatic beam, is composed of a spectrum of photon energies and wavelengths. In general, more energetic beams have higher penetrating power because the attenuation coefficient of a material decreases with photon energy. Hence, as a polychromatic X-ray beam travels through dense material, the softer X-rays (with low energies) are absorbed more resulting in an increase in mean X-ray energy, i.e. the "hardening" of the X-ray beam. As this harder beam travels further into the scanned material, it will be attenuated less (Wildenschild and Sheppard, 2013). Beam hardening, the most frequently encountered artefact in CT scanning (Ketcham and Carlson, 2001), where the scanned object appears more attenuating near its edges and artificial darkening at the centre is shown in figure 2.4.

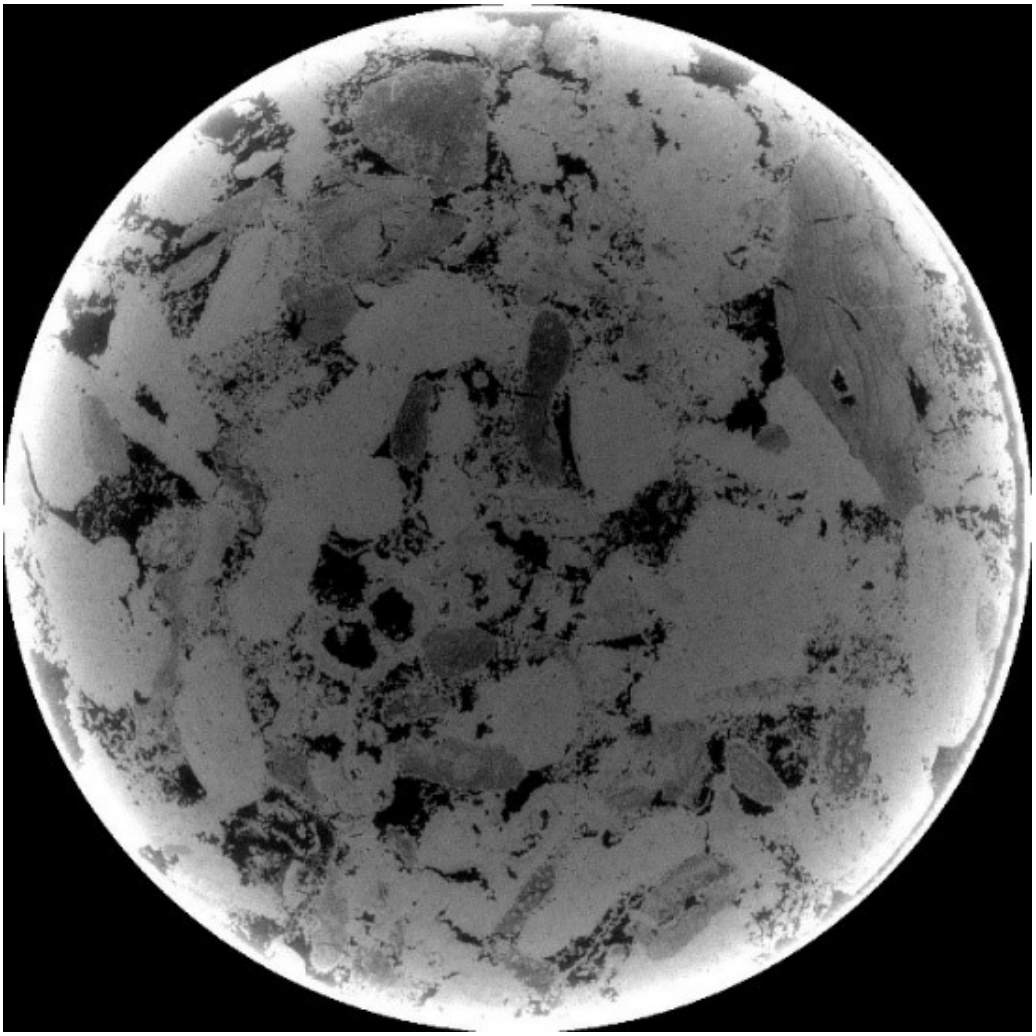

Figure 2.4: . A high-resolution micro-CT image of Estaillades limestone showing the beam hardening artefact (the image is darker near the centre).

A possible remedy to beam hardening is to use filters to attenuate X-ray beams after passing through the scanned object. The filters used are typically flat pieces made of aluminium, copper or brass. Although beam filtration can degrade the X-ray signal and cause noise, this can be overcome by increasing scanning times (Ketcham and Carlson, 2001).

2.2 Literature Review

2.2.1 LSW mechanisms in carbonates

Previous experimental work showed that changing the salinity of the seawater – normally to be more dilute – can enhance oil recovery (Morrow and Buckley, 2011, Yousef et al., 2012a, Mahani et al.,

2017, Mahani et al., 2015, Mahani et al., 2014, Selem et al., 2021b, Yousef et al., 2012b). Reducing brine salinity could cause changes induced by physio-chemical mechanisms in sandstone (Jadhunandan and Morrow, 1995b, Tang and Morrow, 1997, Morrow et al., 1998, Vledder et al., 2010, Kumar et al., 2011, Mahani et al., 2014, Abdolmohsen et al., 2015) and carbonate rocks (Strand et al., 2006, Zhang and Austad, 2006, Fathi et al., 2010, Yousef et al., 2011, Al-Attar et al., 2013, Jackson et al., 2016a, Li et al., 2020), increasing the oil recovery factor. Field trials have reinforced these findings (Yousef et al., 2012a, Mahani et al., 2011, Seccombe et al., 2008, Vledder et al., 2010, Yousef et al., 2012b). The change in the rock surface wettability from oil-wet to a more water-wet state is considered the primary mechanism for the incremental increase in oil recovery (Tang and Morrow, 1999, McGuire et al., 2005, Mahani et al., 2015, Sohrabi et al., 2017, Selem et al., 2021b). However, the wettability shift could be driven by different underlying pore-scale processes and mechanisms, which are yet to be explored and understood (Bartels et al., 2019). Figure 2.5 highlights some of the main LSW mechanisms in carbonates discussed in the literature.

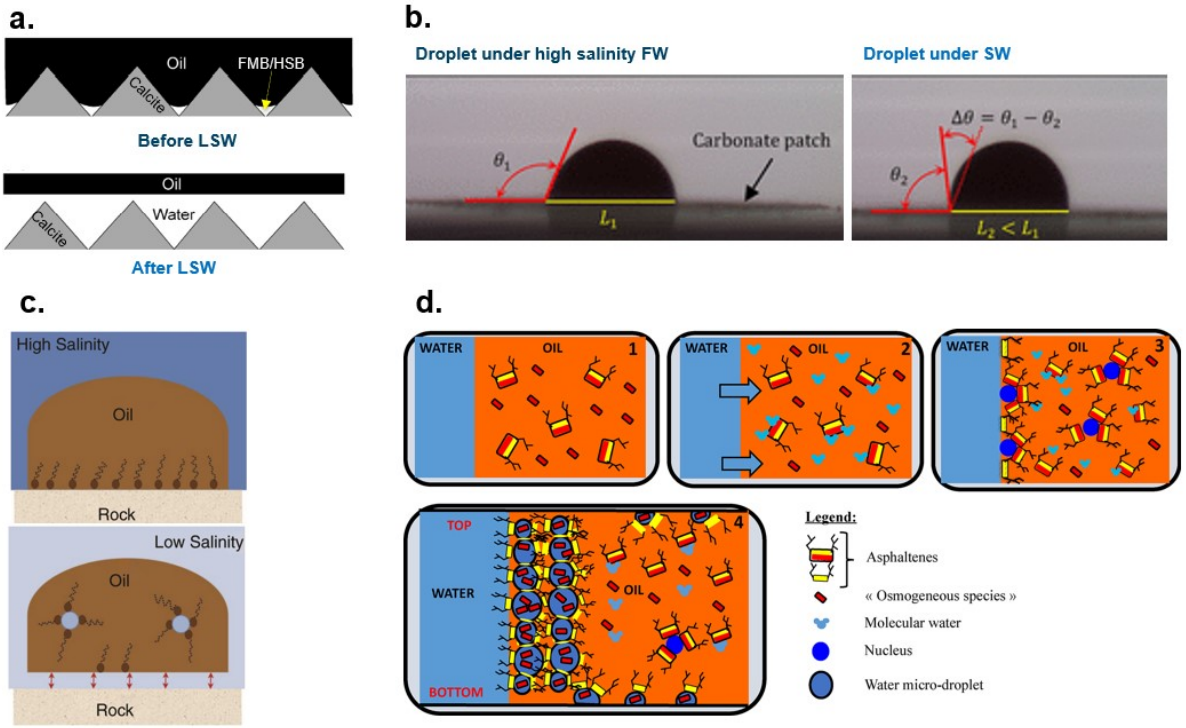

Figure 2.5: Schematic of the key mechanisms of LSW in carbonates. (a) The stability of the water film at the interface between mineral and oil is determined by the surface charge and polarity of the oil, from Jackson et al. (2016a). (b) Change in contact angle and the diameter of the oil-carbonate contact line (L)

indicate a wettability change resulting from reducing brine salinity from formation water (FW) to seawater (SW), from Mahani et al. (2015). (c) The dewetting impact of water-in-oil microdispersions attracting the surface active material detaching the oil from the rock surface under low salinity, from Sohrabi et al. (2017) (d) Spontaneous emulsification and formation of water microdroplets driven by osmosis depending on the salinity concentration of the brine and asphaltene in the crude oil, from Duboué et al. (2019).

The low salinity effect (LSE) is believed to be governed by the pore-scale interactions between crude oil, brine and rock (COBR), with this effect resulting in enhanced oil recovery at the larger core and reservoir scales. The low salinity mechanisms take place at the COBR interfaces and include multi-ion exchange (MIE), a local rise in pH (ΔpH), and double layer expansion (DLE) (Jackson et al., 2016b). While other potential mechanisms, including clay swelling, fines migration, the formation of natural surfactants at elevated pH, the reduction in oil/brine interfacial tension, and increased solubility of polar oil compounds in brine, have been proposed, they do not seem to be essential for observing improved oil recovery. The experimental work by Lager et al. (Lager et al., 2008) on a reservoir sandstone suggested that emulsification is a low salinity effect rather than a cause. They proposed that the interplay between the crude oil, low salinity water and mineral surface in the form of multi-component ionic exchange is the primary mechanism for additional recovery. They explained that due to the lack of clay minerals this mechanism does not work on carbonate reservoirs. Other work showed interfacial reaction-related response in carbonates consisted with double-layer expansion (Yousef et al., 2011, Yousef et al., 2012a). A study exploring the relationship between injected brine salinity and interfacial viscoelasticity showed a correlation between oil recovery and interface elasticity, which holds true for various salt concentrations in the injected brine and extremely low concentrations of surfactants (Kar et al., 2022). The researchers proposed that the system would yield greater oil recovery if the oil and brine created an interface with high viscoelasticity. Reducing injected brine salinity results in increased interface viscoelasticity which in turn suppresses oil trapping by snap-off and enhances oil recovery (Alvarado et al., 2014).

Effects induced by salinity concentration gradients and water-oil emulsions can impact the pore-scale flow (Chakravarty et al., 2015, Wei et al., 2017, Bartels et al., 2019). This can lead to a change in rock wettability and mobilize oil over a relatively short period of a few days. Osmosis and water-in-oil

emulsions have been proposed as the main underlying mechanisms for the LSE (Emadi and Sohrabi, 2013, Mahzari and Sohrabi, 2014, Sandengen et al., 2016, Sohrabi et al., 2017, Fredriksen et al., 2018, Duboué et al., 2019). LSW experiments in both carbonates (AlHammadi et al., 2018b) and sandstones (Mahzari et al., 2019) showed a correlation between increased oil recovery and the ability of the crude oil to form micro-dispersions when exposed to low salinity water. Moreover, further tests of LSW using micromodels observed the mobilization of oil by spontaneous emulsification when in contact with diluted brine (Alzahid et al., 2019, Aldousary and Kovscek, 2019). If a solid interface is in close proximity to the water-oil interface, spontaneous emulsification at the crude oil/water interface might contribute to certain dewetting occurrences at the oil-solid interface during reduced salinity waterflooding (Bartels et al., 2017a). Their hypothesis suggests that the merging of these dewetting patterns results in a continuous water film, potentially elucidating the observed increased oil recovery in certain instances. It is plausible to consider that the "dewetting patterns" may refer to water microdroplets formed spontaneously when crude oil is gently introduced to water.

A lack of consistent experimental conditions across length-scales has hindered our understanding of these mechanisms. Typically, core-scale measurements are conducted at reservoir conditions of pressure, temperature, brine salinity, and crude oil composition (Nasralla et al., 2014, Austad et al., 2015, Austad et al., 2012, Yousef et al., 2011, Zahid et al., 2012, Shehata et al., 2014). In contrast, pore- and mineral-surface-scale measurements, such as atomic force or scanning electron microscopy, contact angle and wetting surface, adsorption, and adhesion, are typically conducted at laboratory temperature and pressure, lower brine salinity, and/or simplified crude composition (Kumar et al., 2021, Chandrasekhar and Mohanty, 2018). To date, pore-scale mechanisms have been identified and visualized merely in microfluidics studies in micro-models (Aldousary and Kovscek, 2019, Alzahid et al., 2019, Fattahi Mehraban et al., 2020, Sohrabi et al., 2017, Mohammadi and Mahani, 2020). However, these are idealized systems and the mechanisms in a representative complex reservoir rock have not been observed except in a very few studies (Selem et al., 2021b, Selem et al., 2021a, Selem et al., 2022, Khishvand et al., 2017a, Qin et al., 2019, Khishvand et al., 2019). These differing experimental conditions may account for the conflicting data that has been obtained thus far.

The field of X-ray microcomputed tomography has developed remarkably over the years and pore-scale characterization studies with high resolution have become possible (Arns et al., 2005, Wildenschild and Sheppard, 2013). This technique was utilised in multiple research and industrial applications, e.g. EOR and gas storage (Iglauer et al., 2010, Blunt et al., 2013, Selem et al., 2022, Alhammadi et al., 2017, Alhosani et al., 2020a, Selem et al., 2021b). The merger between high-pressure and high-temperature flow apparatus and X-ray imaging has resulted in large improvements in our understanding of multiphase flow in natural systems at the pore scale (Andrew et al., 2013, Schlüter et al., 2014, Alhammadi et al., 2018a, Alhosani et al., 2020b).

LSW mechanisms were previously investigated using micro-CT (Lebedeva and Fogden, 2011, Bartels et al., 2016, Khishvand et al., 2017a, Shabaninejad et al., 2018, Andrews et al., 2021, Andrews et al., 2023), however few studies have looked at carbonate rocks (Bartels et al., 2017b, Mirchi, 2018, Tawfik et al., 2019). Moreover, there is an incomplete understanding of how the displacement mechanisms inter-relate. Unsal et al. (2019) compared conventional waterflooding to surfactant flooding highlighting the miscible displacement of oil by surfactant via the formation an emulsion. However, this study did not test whether diluting the salinity of injected brine could cause a similar effect.

In Chapters 4 and 5, we will describe pore-scale studies that investigate the low salinity effect and recovery from secondary and tertiary (where both high and low salinity brines were injected) LSW in Estaillades carbonate, which is a quarry limestone. Multiple observations and measurements indicated wettability changes after the low salinity brine injection towards a more water-wet state. Furthermore, the formation of micro-dispersions was visualised in the pore space and played a significant role in facilitating displacement. However, dependent on the COBR system, the mechanisms for recovery can be very different. Hence, there is a need for better characterisation of LSW in reservoir rock and different crude oils and brines, which can shed light on new mechanisms for recovery. We extend this work in two ways: firstly, to study a reservoir rock, rather than the quarry samples studied hitherto; and secondly to investigate the formation and development of emulsions in detail and their potential contribution to recovery.

2.2.2 Wettability alteration and oil recovery

The drive to better understand the physico-chemical mechanisms underlying LSW in carbonates has led many researchers to attempt to characterise the properties that make a given COBR system susceptible to LSW. Regardless of the conditions required to observe the LSE, it is commonly accepted that wettability alteration is most likely the main underlying mechanism of LSW (Mahani et al., 2015, RezaeiDoust et al., 2009, Strand et al., 2006, Zhang and Austad, 2006, Zhang et al., 2007).

It is generally believed that the majority of hydrocarbon reservoirs were originally wetted by water during the deposition of sediments in aqueous environments (Anderson, 1986). After the formation of the reservoir, crude oil moves upwards from the underlying source rock under the influence of buoyancy forces, displacing water from the pore space (Abdallah et al., 1986). The constituents and conditions for the rock and fluid phases influence the wetting preference. Thus, the crude oil properties, the brine chemistry, and the mineral surface, as well as the system temperature, pressure and saturation history must be considered (Buckley et al., 1998). Oil composition is key to changing the wettability of a naturally water-wet surface because of the wettability-altering polar components in resins and asphaltenes contained in the oil phase. The solubility of these polar components is determined by the bulk-oil composition. The lower the crude oil ability to dissolve the polar components, the greater its tendency to change wettability (Abdallah et al., 1986).

Exposure of rocks to oil is believed to change the wettability status towards increased oil-wetness. There's a theory suggesting that reservoirs typically exhibit a mixed-wet wettability state. In this state, some areas of the pore space are water-wet, while others, due to direct contact with surface-active components of crude oil, transition to an oil-wet condition (Salathiel, 1973, Buckley et al., 1998).

During controlled salinity waterflooding, further wettability alteration occurs towards increased water-wetness (Morrow and Buckley, 2011). The shift in the oil-wet system towards a more water-wet state releases more oil and results in higher oil recovery. This is achieved by manipulating the brine salinity and ionic composition to an optimum level (Vledder et al., 2010, Yousef et al., 2011). Maximum recovery from waterflooding at the pore scale is obtained when a certain state in rock wettability is

achieved. Strongly water-wet conditions cause snap-off events across the pore network, immobilising the oil (non-wetting phase) in large pores. On the other hand, strongly oil-wet conditions result in a very low conductance, i.e. relative permeability, in the oil phase as it connects in thin layers and between the smallest pores and throats (Blunt, 2017).

Alhammadi et al. (2017) characterised the in-situ wettability alteration in cores obtained from a producing carbonate reservoir utilising contact angle measurement from X-ray micro-CT images. The study concluded that the oil-wet samples showed the lowest oil recovery whereas the water-wet samples showed fast oil recovery but at intermediate recovery factors. The partial recovery is ascribed to capillary trapping (highlighted in section 2.1.3), a naturally occurring phenomenon where the non-wetting phase within the larger pores of a porous medium is immobilized against advection. This immobilization occurs in the form of pore-scale ganglia due to capillary forces. The highest recovery was observed in the samples that are mixed wet.

Many oil recovery techniques depend on pore-level interactions involving crude oil-brine-rock (COBR) system properties. In waterflooding, water is injected on a macroscopic scale to push the oil from injection wells towards production wells. Oil blobs can be trapped within the reservoir pore space due to high capillary forces. The amount of immobile oil trapped depends on a range of physical properties of the COBR system. One of the main physical properties that affect the microfluidic displacement efficiency within reservoir rocks is the rock's wettability. In fact, the maximum oil recovery that can be achieved by waterflooding is strongly influenced by the pore-level physics of wettability as well as the oil viscosity. However, the sensitivity of two-phase flow to oil saturation in a mixed-wet rocks make this topic a complex one to study (Salathiel, 1973, Graue et al., 1999, Jadhunandan and Morrow, 1995b).

Christensen and Tanino (2017) studied the dependence of waterflood oil recovery from mixed-wet limestone upon contact angle. The study found that in all mixed-wet conditions, remaining oil saturation decreased with the progression of waterflood until it reached a constant value, with a power law accurately describing the approach to residual oil saturation. The study also revealed that the cumulative volume of water necessary to attain residual saturation increased in a linear fashion with the contact

angle. They also showed that the residual oil saturation exhibits a continuous decrease as the contact angle increases in a monotonic fashion (Christensen and Tanino, 2018, Tanino and Christensen, 2019).

The aim of the various EOR methods is to overcome the wetting forces that cause oil entrapment. The idea is to either alter the rock wettability preferences or decrease the interfacial tension between the different phases. In waterflooding EOR, the injected brine has different dissolved solid contents or pH from those of the formation brine to bring about wettability changes. Lowering the brine salinity could cause a change in the system wettability towards intermediate wettability (Al-Attar et al., 2013). If a correlation can be established between the contact angle, fluid distribution, multiphase flow, and recovery, then it may be feasible to enhance oil recovery by manipulating the reservoir's wettability through a prudent selection of injection brine.

Chapter 3

Materials and methods

In this chapter we will present the materials and methods used in the experimental studies and laboratory work.

3.1 Materials

3.1.1 Rocks

The rock used in the first set of experiments (in chapters 4 and 5) was a carbonate quarry rock, Estaillades, composed of 97 weight% calcite with traces of dolomite (Bijeljic et al., 2013, Alyafei and Blunt, 2016). Estaillades has a bimodal pore size distribution, prolific intergranular macro-porosity, and abundant micro-porosity in the bioclasts. A cylindrical rock sample, up to 6 mm in diameter and 12 mm in length, was used in the coreflooding experiment. The sample had a porosity of 0.293 ± 0.003, measured using a helium porosimeter (AccuPyc II 1340), and an absolute permeability of 0.11 ± 0.03 Darcy calculated from pressure drop measurements during brine injection.

The rock used in the second set of experiments (in chapter 6) was a reservoir carbonate composed predominantly of limestone with pyrite. It has a bimodal pore size distribution, prolific inter- and intragranular macro-porosity, and abundant micro-porosity. The rock extracted from the reservoir has porosity and permeability ranges of 0.17-0.20 and 0.05 – 0.20 mDarcy, respectively. A cylindrical rock sample, 6 mm in diameter and 12 mm in length, was drilled out from a larger sample. The extracted sample had a porosity of 0.199 ± 0.003, measured using a helium porosimeter (AccuPyc II 1340), and an absolute permeability of 0.12 ± 0.03 Darcy calculated from pressure drop measurements during brine injection. Figure 3.1 shows a 2D X-ray image of the rocks used in the experimental work. Both rock samples have been provided by the sponsor.

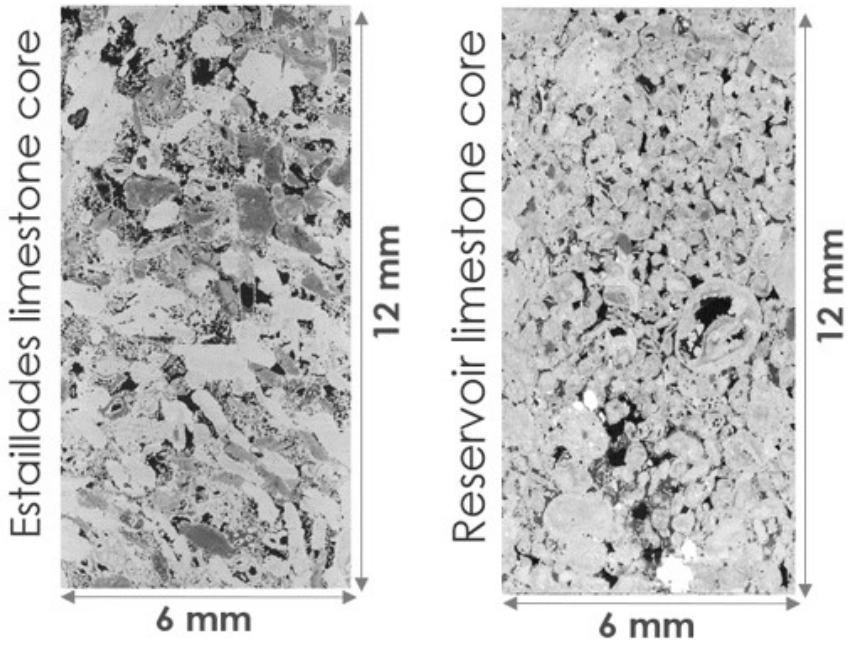

Figure 3.1: The carbonate limestone rock samples used in this work: Estaillades (left) and reservoir rock (right).

3.1.2 Fluids

Table 1 shows the composition and salinity of each brine used in the experiments on Estaillades rock and the total acid and base numbers and the SARA (Saturates, Aromatics, Resins, Asphaltenes) analysis results for the crude oil used on those experiments. Formation brine (FB), high salinity brine (HSB) and low salinity brine (LSB) were formulated in the Imperial College London lab as synthetic solutions of several pure salts (supplied by Sigma-Aldrich) in deionized water. HSB was prepared as desulphated seawater, and LSB as a more dilute salt solution. The viscosity values, at 70 °C, of HSB and LSB are 0.448 and 0.426 mPa·s, respectively. The oil was provided by the sponsor and was previously dehydrated and filtered to remove any residue or dispersed solid. The interfacial tension (IFT) between oil and, FB and LSB is 16.3 and 22.3 mN/m, respectively, measured at 35 °C.

Table 3.1: Composition and properties of the fluids used in the Estaillades experiments.

	Salt concentration (g/L)						
	NaCl	KCl	$CaCl_2 \cdot 2H_2O$	$MgCl_2 \cdot 6H_2O$	Na_2SO_4	$NaHCO_3$	**Total dissolved solids**
Formation brine (FB1)	109.55	0.00	46.070	11.240	0.140	0.200	**167.200**
High salinity brine (HSB)	29.00	0.90	0.605	0.405	0.026	0.156	**31.092**
Low salinity brine (LSB1)	0.76	0.035	0.020	0.296	0.087	0.0007	**1.200**

For the reservoir rock experiments, brines were prepared in the same manner. There are slight differences between FB and LSB whereas the same HSB was used in both experiments to represent seawater. The viscosity of FB, at 80 °C, was measured to be 0.501 mPa·s. The oil was dehydrated and filtered to remove any residue or dispersed solid. The interfacial tension (IFT) between oil and FB is 26.3 mN/m, measured at 45 °C. The geochemical properties of the crude oils used in this work are shown in Table 3.3.

Table 3.2: Composition of the brines used in reservoir rock experiments.

	Salt concentration (g/L)						
	NaCl	KCl	$CaCl_2 \cdot 2H_2O$	$MgCl_2 \cdot 6H_2O$	Na_2SO_4	$NaHCO_3$	**Total dissolved solids**
Formation brine (FB2)	90	6.40	50	10	0.150	0.000	**156.550**
High salinity brine (HSB)	29.00	0.90	0.605	0.405	0.026	0.156	**31.092**
Low salinity brine (LSB2)	0.77	0.00	0.23	0.058	0.038	0.003	**1.100**

Table 3.3: Geochemical properties of crude oil 1 and 2 used in Estaillades and reservoir rocks, respectively. Both oils were prepared and provided by the sponsor.

	Crude oil 1	Crude oil 2
TAN (mg KOH/g)	0.34	0.57
TBN (mg KOH/g)	0.41	3.22
Saturates (w%)	48.40	0.00
Aromatics (w%)	48.10	
Resins (w%)	2.80	
Asphaltenes (w%)	0.70	
Viscosity (cP) at 70 °C	1.56	4.14
Density (g/cc) at 70 °C	0.80	0.84

3.2 Methods

3.2.1 Experimental apparatus and procedure

The experimental apparatus consisted of a carbon fibre flow cell connected to syringe pumps (Teledyne ISCO) via PEEK tubing and valves to control the pressure and flow rate inside the sample (Figure 3.2). The rock sample was centred in the middle of the coreholder and connected to the flow lines by two steel end pieces placed at the inlet and outlet. Flow lines are thermoplastic $1/16^{th}$ inch (1.6 mm) PEEK tubing which can withstand high pressures and temperatures. The main stages of this experimental study were: (i) cleaning with isopropanol and fully saturating the sample with formation brine, (ii) injecting crude oil for 3 weeks, at high temperature, to alter the rock wettability, and (iii) studying the *in situ* effects of changing the injected brine salinity during waterflooding through the acquisition of X-ray images.

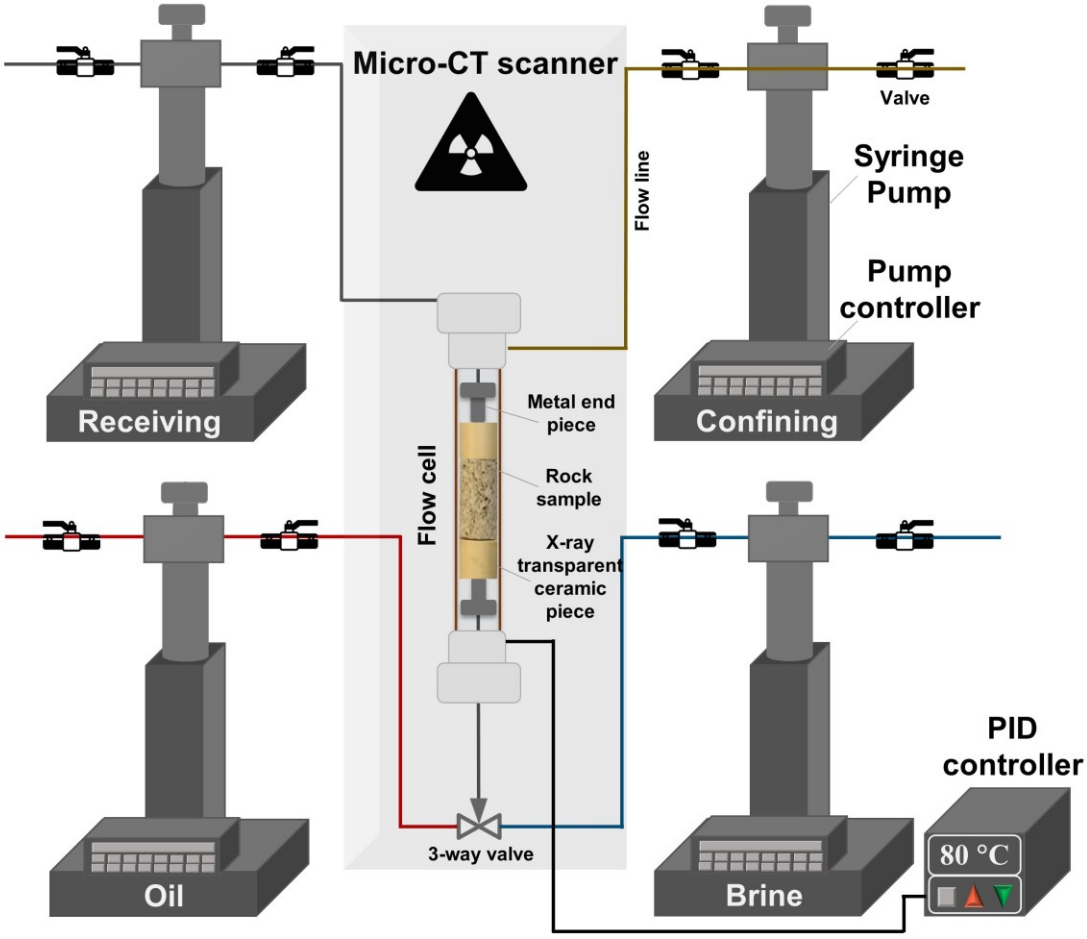

Figure 3.2: The experimental apparatus consisting of the flow apparatus and micro-CT scanner used in this study.

The experimental procedure was developed with the sponsor and is as follows:

1. A confining pressure of 2 MPa was applied in the isolated space between the Viton sleeve containing the rock sample and the carbon fibre sleeve of the coreholder. The confining pressure, applied with de-ionised water, squeezed the sleeve onto the sample to avoid fluid side flow.
2. The dry cylindrical sample (called a core) was imaged using a micro-CT scanner. Figure 3.3 shows the interior of the micro-CT used with the various components: X-ray source, flow-cell, rotation stage and detector.
3. The sample was then cleaned by injecting four-times diluted formation brine followed by isopropanol, both for 10 pore volumes (PVs). It was dried with a gentle nitrogen flux for 24 hours then vacuumed for 3 hours.

4. The formation brine was then injected for 200 pore volumes to saturate the rock sample thoroughly. The absolute permeability of the sample was measured.
5. Drainage was performed with the injection of viscous synthetic oil, Marcol 52, at increasing flow rates to reach irreducible water saturation. This synthetic oil has a density and dynamic viscosity of 836 kg/m^3 and 12 mPa·s, respectively, measured at 20 °C.
6. Toluene was injected for 10 PVs to avoid mixing synthetic and crude oils. Crude oil was then introduced at an increased temperature, 50 °C, to avoid wax precipitation. The wax appearance temperature is 31 °C.
7. The coreholder assembly was then moved to an oven at 80 °C and 11 MPa back pressure, with 13 MPa confining pressure, to change the rock wettability to a similar state found in oil reservoirs (this process is called ageing). Crude oil was injected at a low flow rate (2 µL/min) for three weeks. The flow direction reversed after 1.5 weeks.
8. After ageing, the temperature in the system was kept at 80 °C using an Omega flexible heating tape and a PID controller, as shown in Figure 3.2.
9. Before waterflooding, crude oil mixed with a 20 weight% of 1-iododecane, as a high contrast dopant, replaced the crude oil in the sample to distinguish the oil phase from the brine in the X-ray images to calculate the initial water saturation. A 20 wt% of dopant was the optimum concentration providing sufficient contrast when compared with 10 wt% (too low) and 30 wt% (too high). The dopant addition has a limited impact on the IFT between oil and brine (Selem et al., 2022). The oil asphaltene content remains unchanged when the dopant is used (Qin et al., 2019).
10. The sample was flooded with HSB and then LSB in the tertiary mode experiment.
11. The same experimental procedure was followed in the secondary mode experiments on another identical sample from the same core plug but without the injection of HSB during the waterflooding process. More details of the waterflooding procedure in both experiments are highlighted in the next section.

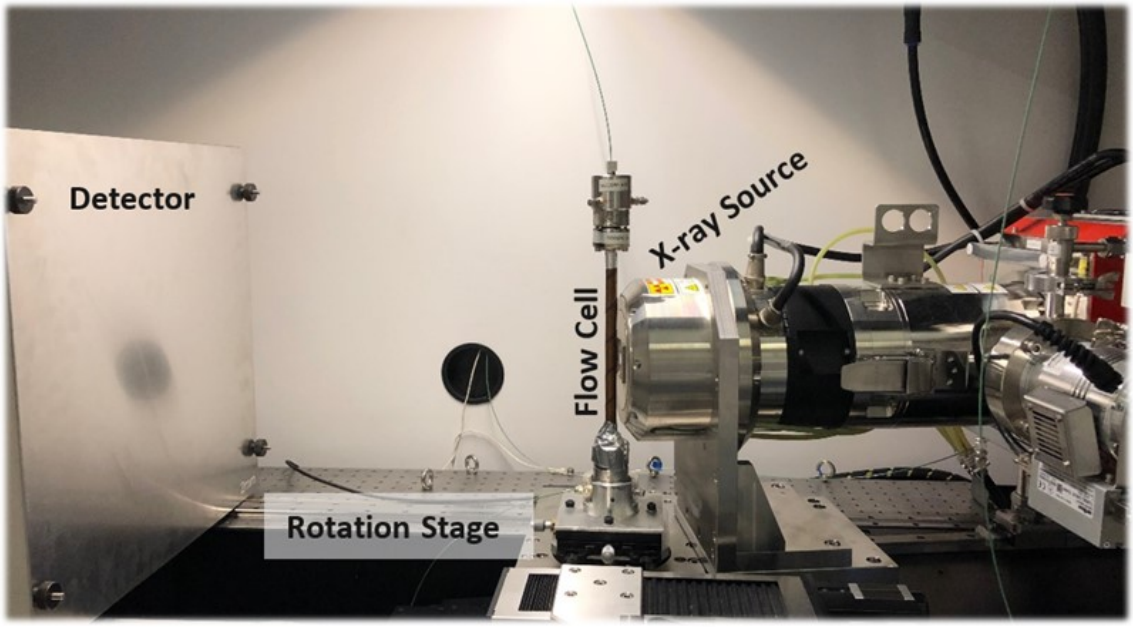

Figure 3.3: The interior of the micro-CT scanner used in this study.

3.2.2 Waterflooding sequence

The flooding experiment was performed in two modes, low salinity flooding at the residual oil saturation after high salinity flooding (tertiary mode), and low salinity flooding at initial oil saturation (secondary mode). In tertiary mode, HSB was injected at a sequence of increasing flow rates; 1, 2, 4, 11, 22 and 42 µL/min at 70 °C. 10 pore volumes were injected at each rate. LSB was then injected following the same procedure.

The capillary numbers associated with the flow rates indicate capillary force dominated flow conditions with values ranging from approximately 10^{-8} to 10^{-7} at the lowest and highest rates respectively. Table 3.4 lists the capillary number values for all flow rates used in both secondary and tertiary LSW experiments on Estaillades. The sample was scanned after the 1, 4, 11 and 42 µL/min injection rates during both the high and low salinity floods. A total of 8 images were acquired throughout waterflooding. The inlet was placed at the bottom of the sample.

Table 3.4: Waterflooding injection steps with calculated capillary numbers on Estaillades rock.

Injection rate (μL/min)		**1**	**2**	**4**	**11**	**22**	**42**
Capillary number	**High salinity**	1.02×10^{-8}	2.05×10^{-8}	4.09×10^{-8}	1.13×10^{-7}	2.25×10^{-7}	4.30×10^{-7}
	Low salinity	9.72×10^{-9}	1.94×10^{-8}	3.89×10^{-8}	1.07×10^{-7}	2.14×10^{-7}	4.08×10^{-7}

In the secondary mode, however, only LSB was injected. The same flow rates and pore volumes as in the tertiary mode were used. . The sample was scanned after the 1, 2, 4, 11 and 42 μL/min injection rates resulting in a total of 5 images acquired throughout waterflooding.

In the waterflooding experiments performed on the reservoir sample, discussed in chapter 6, brine was injected at 1 and 10 μL/min with 5 pore volumes (PVs) injected at each rate in the tertiary mode experiment. An additional 5 PV were injected towards the end. In the secondary mode experiment, only LSB was injected following the same procedure in terms of flow rates and number of PVs injected, as shown in Table 3.5.

Table 3.5 Waterflooding sequence details in the experiments on reservoir rock.

Experiment	**Waterflooding sequence**	**Brine injected**	**Injection rate (μL/min)**	**Number of pore volumes injected**
Tertiary mode	HS1	HSB	1	5
	HS2	HSB	10	5
	HS3	HSB	10	5
	LS	LSB	1	5
Secondary mode	LS1	LSB	1	5
	LS2	LSB	10	5
	LS3	LSB	10	5

3.2.3 Image acquisition, processing, and segmentation

A micro-CT scanner, HeliScan manufactured by Thermo Fisher. was used to acquire 3D tomograms with 95 keV energy, exposure time of 0.8 s and 3600 projections with the continuous helical movement of the sample and 360° rotation. X-ray images were taken at different points through the experiment: a dry scan before fluid injection (reference image), after ageing and before waterflooding, and during HS and LS waterflooding. Each acquisition took nearly a day, and the size of the acquired images was 2880×2880×5200 voxels, with a resolution of 2.3 µm/voxel. This is the optimum resolution that can be achieved in a reasonable timeframe and not a very large image size that requires significant computational power. The images were filtered using non-local means edge-preserving filter to remove image noise (Buades et al., 2005). A watershed algorithm was used for image segmentation. This algorithm is based on generating a seed using a two-dimensional histogram of both the greyscale and the greyscale gradient images (Jones et al., 2007, Andrew et al., 2014b), as shown in Figure 3.4. A mask of segmented pores from the dry scan was applied on all subsequent images to separate the macro-pores from the rest of the rock and to simplify the segmentation of the oil and brine within, Figure 3.5. The processing of the images was performed using Avizo 9.5 software.

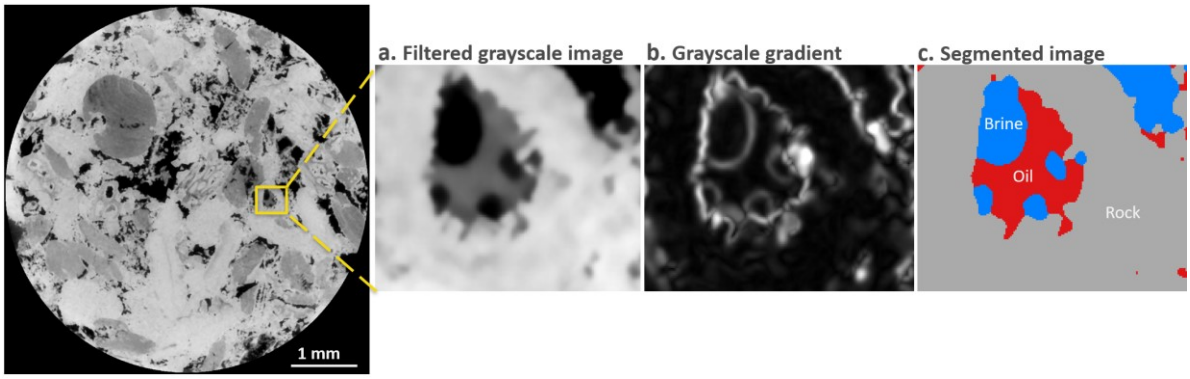

Figure 3.4: An example showing the segmentation workflow using seeded watershed algorithm. A seed is generated using a two-dimensional histogram of both the greyscale (a) and the greyscale gradient (b)

images to produce a labelled image (c) showing the different phases: brine, oil and rock. The segmentation was performed using Avizo 9.5 software (https://www.fei.com/software/amira-avizo/)

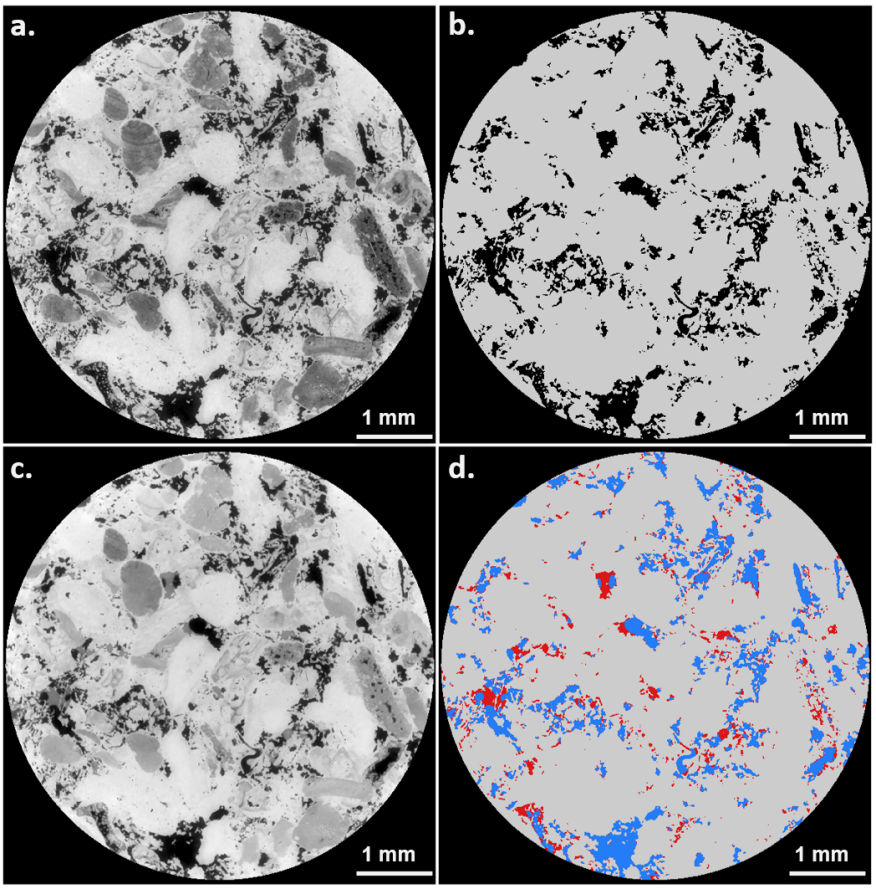

Figure 3.5: Image segmentation workflow. A filtered two-dimensional cross-section of the three-dimensional micro-CT dry image (a), which is segmented into resolved pores (black) and grains (grey) in (b). An orthogonal slice from an image of the sample saturated with brine and doped oil at the end of low salinity waterflooding (c). The pores mask was applied to the saturated sample image to separate the pore space and segment it into oil and brine shown in red and blue respectively, and then the rock phase in grey was added (d).

All images were segmented into rock, water and oil phases using a seeded watershed algorithm (Andrew et al., 2014a, Jones et al., 2007), as shown in Figures 3.4 and 3.5. The segmented images were used to calculate oil and water saturation in the resolved macro-pore space. The seeded watershed segmentation method was used to analyse the images from the Estaillades experiments in chapters 4 and 5, e.g. the results highlighted in sections 4.1 and 5.1 were obtained using this method.

More details on pore space characterization and the differentiation between macro and micro-pores are in the next section.

3.2.4 Contrast Study

The distinction between the different phases in the scanned sample is critical to conduct image analysis. During contrast scanning, small glass tubes containing crushed rock, low salinity brine, high salinity brine and crude oil were scanned. During low salinity experiments, high and low salinity brine, as well as crude oil, will be injected into the rock sample, so it is critical to find whether a good image contrast will be generated when brine and oil coexist in the system. Figure 3.6 shows an image of a contrast scan where the solid grains, grains with micro-pores, brine and crude oil are clearly distinguished.

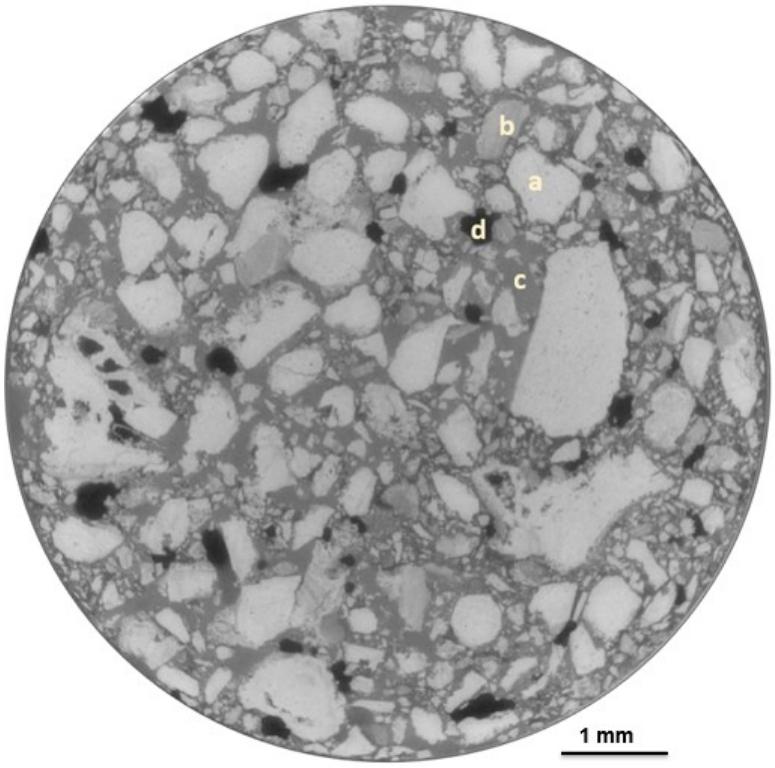

Figure 3.6: A contrast scan image showing (a) grains of crushed rock in white, (b) grains with micro-pores in light grey, (c) formation brine in dark grey, and (d) crude oil in black.

3.2.5 Porosity characterization

We assessed the rock dual-porosity (that is macro pores that can be explicitly resolved in the image and micro-porosity below the image resolution) using the differential imaging technique (Lin et al., 2016). A brine solution made from de-ionized water doped with 20 weight% Potassium Iodide (KI), as a high contrast agent, was used in the characterization of sub-micron porosity. This dense brine can be

distinguished from rock phases for effective image segmentation and characterization of the rock bimodal porosity. As mentioned previously in the experimental procedure steps, X-ray micro-CT was used to acquire a dry (air) image of the rock and an image after KI-brine injection. The KI brine will help distinguish the grains with micropores from that are composed of different mineralogy yet have the same grey-scale values. Initially a 10 wt.% KI brine was used but the contrast was not sufficient, so a 20 wt.% KI brine was injected which offered a good phase contrast. The sample was scanned with 100 keV at 2.5 µm voxel size. Figure 3.7 shows the difference in contrast quality of the scans using the two brines.

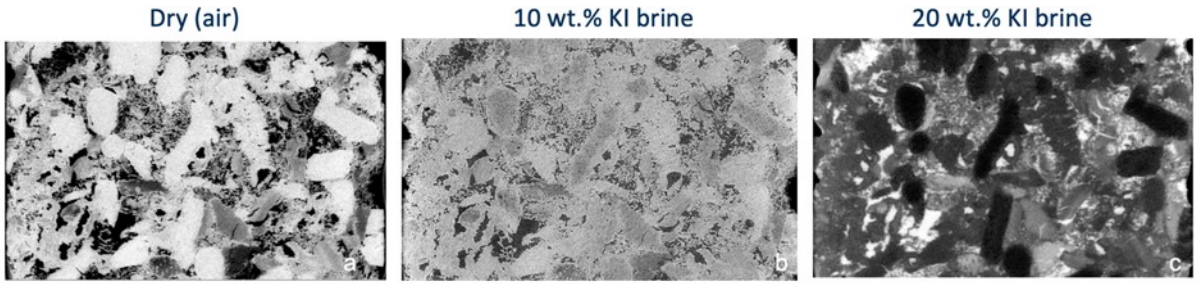

Figure 3.7: Estaillades limestone micro-CT image showing the contrast results with different KI concentrations. (a) Dry (air) scan. (b) 10 wt.% KI brine saturated sample scan. (c) 20 wt.% KI brine saturated sample scan.

To maximize the phase contrast between the grain and pore phases, a differential image between the KI-saturated and dry images was obtained. This image was then segmented using the seeded watershed method into solid grains, sub-resolution pores and macro pores. This differential imaging workflow is shown in Figure 3.8. The segmented label images combined with the KI-saturated image were used to obtain histograms of the grey-scale voxels for each phase (Figure 3.9). The peak values (CT) of the histograms were used to calculate the micro-porosity fraction (ϕ_{micro}),

$$\phi_{micro} = \frac{CT_{\text{micro}} - CT_{\text{grain}}}{CT_{\text{macro}} - CT_{\text{grain}}} \tag{3.2}$$

The total pore space comprises the macro- and macro-pores,

$$\phi_{total} = \phi_{micro} \times V_{micro} + 1 \times V_{macro} \tag{3.3}$$

where V_{micro} and V_{macro} are the total volume fractions for each phase obtained from the segmented image.

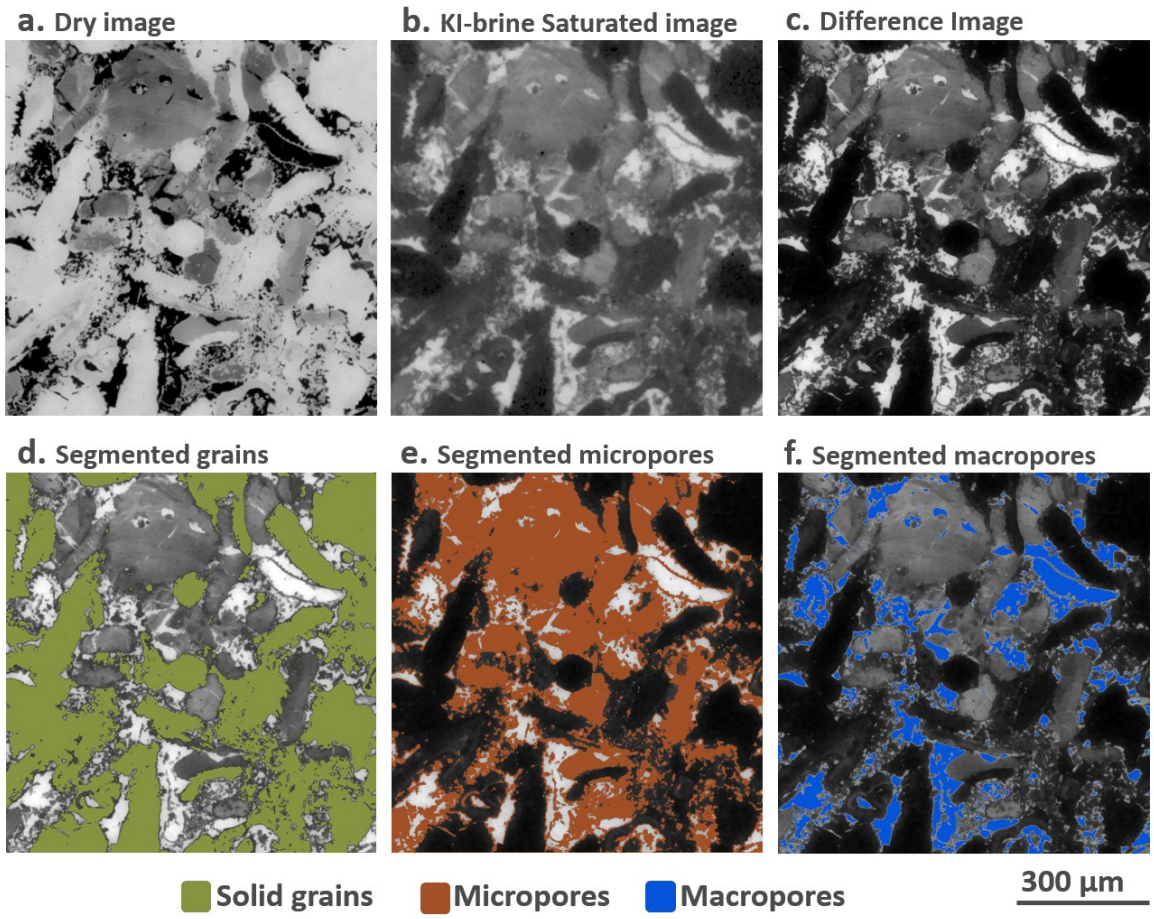

Figure 3.8: Two-dimensional cross-sections of three-dimensional micro-CT images at the same location in the Estaillades sample. (a) The dry scan. Air in the pore space does not adsorb X-rays and is black in the image. (b) The brine-saturated image. Brine has a higher X-ray attenuation than solid and appears bright (white) in the image. (c) The difference image between (b) and (a). The black in (c) represents the impermeable solid grains, white is macro pore space, while intermediate grey values indicate micro-porosity where the pore structure cannot be explicitly resolved in the image. Segmentation classification shown as two-dimensional cross-sections of the three-dimensional images of the same slice: (d) Solid grains (green). (e) Micro-pore phase (orange). (f) Macro-pore space (blue).

Our analysis showed that the rock sample has 0.128 and 0.171 macro- and micro-porosity, respectively: a total of 0.299 ± 0.007. which agrees, within experimental uncertainty, with the total helium-measured porosity of 0.293 ± 0.003 (measurement conducted at Imperial College London). Based on observations from the X-ray images acquired, we assumed that the micro-porosity remained water saturated. The greyscale value of the microporous grains did not change when doped oil was introduced nor during waterflooding indicating that these sub-resolution pores were brine-saturated throughout the experiment. Since micro-pores are below the resolution of the micro-CT scanner (3 µm/voxel), further

analysis will focus on macro-pores where fluid saturation, as well as contact angles and curvatures between the different phases, can be measured. The majority of resolved pore elements in studied rocks have radii in the range of 15 to 60 µm for pores and 5 to 30 µm for throats. This porosity characterization method was performed predominantly on Estaillades limestones.

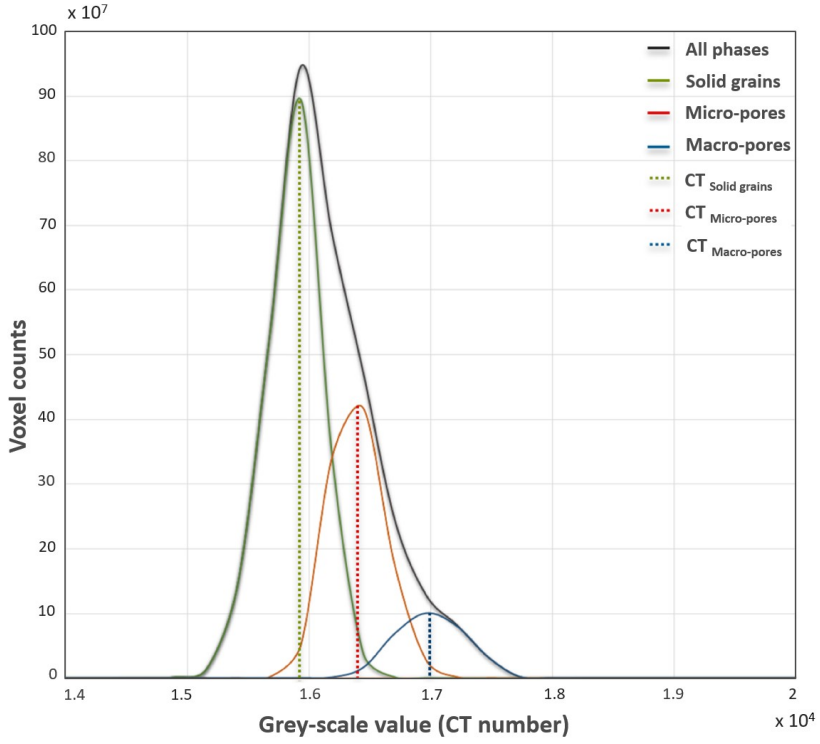

Figure 3.9: Histograms of the grey-scale values of the phases in the KI saturated image (Figure 3.8b) used to calculate the fraction of unresolved pores in the micro-porous rock grains.

3.2.6 Characterization of wettability and fluid distribution

Contact angles were measured by fitting smoothed surfaces to the oil/brine interfaces, obtained from segmented 3D images, and recording their intersection with the rock surface using defined perpendicular vectors. An automated algorithm was used allowing for hundreds of thousands of contact angle measurements (AlRatrout et al., 2017). The measurements were performed on a subvolume of the tomogram (Figure 9.2 in Appendix 1). An example of the number of contact points and values of contact

angles measured before and during waterflooding in secondary LSW experiment (chapter 5) is shown in Table. 3.5.

Table 3.5: Contact angles statistics and results. The measurements were conducted on a sub-volume with a total volume of 1.5 mm^3 (132.8 million voxels).

Injection rate (µL/min)	Counts (thousands)	Mean contact angle (°)	Standard deviation (± °)
Before waterflooding (after ageing)	54.13	124.0	22.9
1	201.64	114.3	24.1
2	190.17	114.1	22.3
4	154.08	113.5	24.7
11	142.07	113.6	20.3
42	106.34	107.7	22.8

Curvature measurements were obtained by extracting and smoothing the oil/brine interfaces and determining the principal curvature values and directions using commercial image analysis software, Avizo 9.5 (Armstrong et al., 2012, Andrew et al., 2014b, Sun et al., 2020). The curvatures were analyzed from the fluid interfaces extracted from the same sub-volume on which contact angles measurements were performed. The voxelized interfaces were smoothed using a volume preserving Gaussian smoothing (Taubin, 1995), Figure 3.10. The mean of the two principal curvatures (κ_1 and κ_2) was calculated as $\kappa = (\kappa_1 + \kappa_2)/2$. This method for determination of curvatures was used in chapters 4 and 5, specifically in sections 4.3 and 5.3.

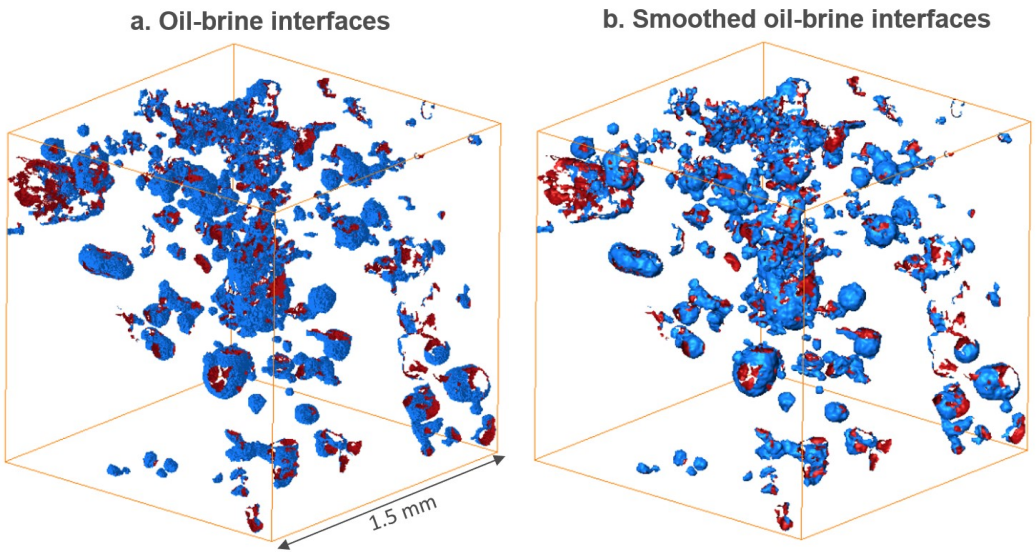

Figure 3.10: Oil-brine interfaces were smoothed using volume preserving Gaussian smoothing (kernel size 5) to remove voxelization artefacts. Curvatures were measured on the smoothed interfaces. The interfaces were extracted from the images, acquired on Estaillades rock, using commercial image analysis software, Avizo 9.5.

3.2.7 Pore occupancy analysis

Pore occupancy was determined by applying a generalized pore network extraction algorithm (Dong and Blunt, 2009, Raeini et al., 2017) to the segmented 3D images with oil and brine labels. This method was used in previous experimental studies (Gao et al., 2019, Gao et al., 2020, Selem et al., 2021b, Scanziani et al., 2018). The occupancy of both pores – wide regions of the void space – and throats – the narrow connections between pores – was quantified. Volume fractions of oil and brine have also been calculated directly from the segmented images to determine the remaining oil saturation after the floods and quantify oil recovery.

The distribution of the fluid occupancy of pores and throats, their sizes and location were investigated using a generalized pore network extraction algorithm (Raeini et al., 2017). The algorithm divided the pore space into pores (wider regions) connected with throats (narrower regions) with voxels assigned to unique pores and throats (Figure 3.11a). The volume-weighted fractions of pore elements whose centres were occupied mainly by either brine or oil were calculated to assess the fluid occupancy at different stages before and during low salinity waterflooding (Figure 3.11b-d). The volume-weighted

probability of a range elements with a radius in the range of $r - dr/2$ and $r + dr/2$ is determined from the following expression:

$$PDF_V(r) = \frac{\sum_{r-dr/2}^{r+dr/2} V_r}{\sum_0^\infty V_r} \tag{3.4}$$

where V_r is volume of elements in the range of radius considered (Raeini et al., 2017).

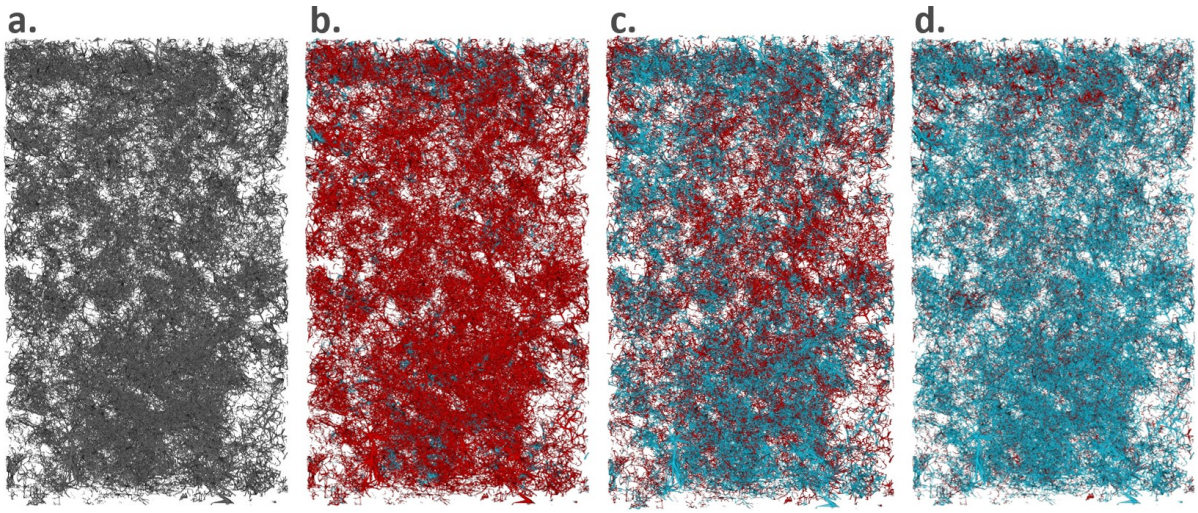

Figure 3.11: Pore network extraction and fluid occupancy mapping from the 3D segmented images. (a) A pore network extracted from the segmented dry image of the whole sample with 5.9 mm diameter and 10 mm length. (b-d) Occupancy maps of oil (red) and brine (blue) before, during and at the end of low salinity water injection, respectively. The code used for this extraction can be found on github.com/ImperialCollegeLondon/porescale

Pore occupancy analysis was performed on the images from all experiments and highlighted in the results in sections 4.2, 5.2, and 6.5 in the upcoming chapters 4, 5 and 6 respectively.

The experimental preparation steps, waterflooding sequences, image acquisition and data analysis are quite sensitive, time consuming and interdependent hence the challenge of repeatability of those experiments.

Chapter 4

Pore-scale processes in tertiary low salinity waterflooding in Estaillades limestone: micro-dispersions, water film growth, and wettability change

In this chapter, we present the experimental observations of the low salinity effect (LSE) at the pore-scale, characterise the wettability changes associated with this LSE, and assess its impact on pore occupancy and oil recovery. X-ray images were acquired during a tertiary LSW, high salinity followed by low salinity brine injection, experiment on Estaillades limestone at reservoir conditions. We captured the development of water micro-droplets and the expansion of thin water films after LSW. A suite of methods were applied to measure contact angle, curvature and capillary pressure at different stages throughout the flooding experiment. The experimental and analysis protocols are as described in chapter 3.

We compare the results obtained before waterflooding, and after different high salinity and low salinity waterfloods. In section 4.1, we investigate and visualize displacement processes and mechanisms, such as the formation of water micro-dispersions and the growth of water films, at the pore level because of LSW. In section 4.2, segmented images are used to map fluid occupancy in the pore space. In section 4.3, in situ wettability is characterized using interfacial areas, contact angle and curvature measurements as well as calculated capillary pressure. Then, the fluid connectivity using Gaussian curvatures and 3D visualization is demonstrated in section 4.4 followed by a discussion of the interrelationship between this set of results, and the oil saturation and recovery profiles in section 4.5.

4.1 Pore-scale displacement processes

We used the raw images to highlight any variations between the initial case before any waterflooding and the results after both high and low salinity waterflooding. Figure 4.1 shows two-dimensional cross-sections of the sample at different stages in the experiment. Initially, oil filled the pore space and brine blobs resided mainly in the centre of the pores (Figure 4.1a). This, in itself, is an interesting observation and implies that during ageing there is likely to be some rearrangement of the fluid phases, with water, initially the wetting phase in small pores and micro-porosity, moving into larger pores once the wettability changes. With HSW (Figure 4.1b-c), the volume of brine increased but oil remained in dead-end pores (orange circles), in pore-corners (red arrows) and layers along the pore walls (yellow arrows). When low salinity brine was injected, significant fluid/fluid and fluid/solid interactions were observed (Figure 4.1d-f). The oil layers started to collapse, and oil was displaced from pore corners and dead-end pores. Water domains, highlighted by blue arrows, formed between the oil and the rock surface and, with the continued injection of low salinity brine, they grew displacing most of the oil in the pore, highlighted with orange circles.

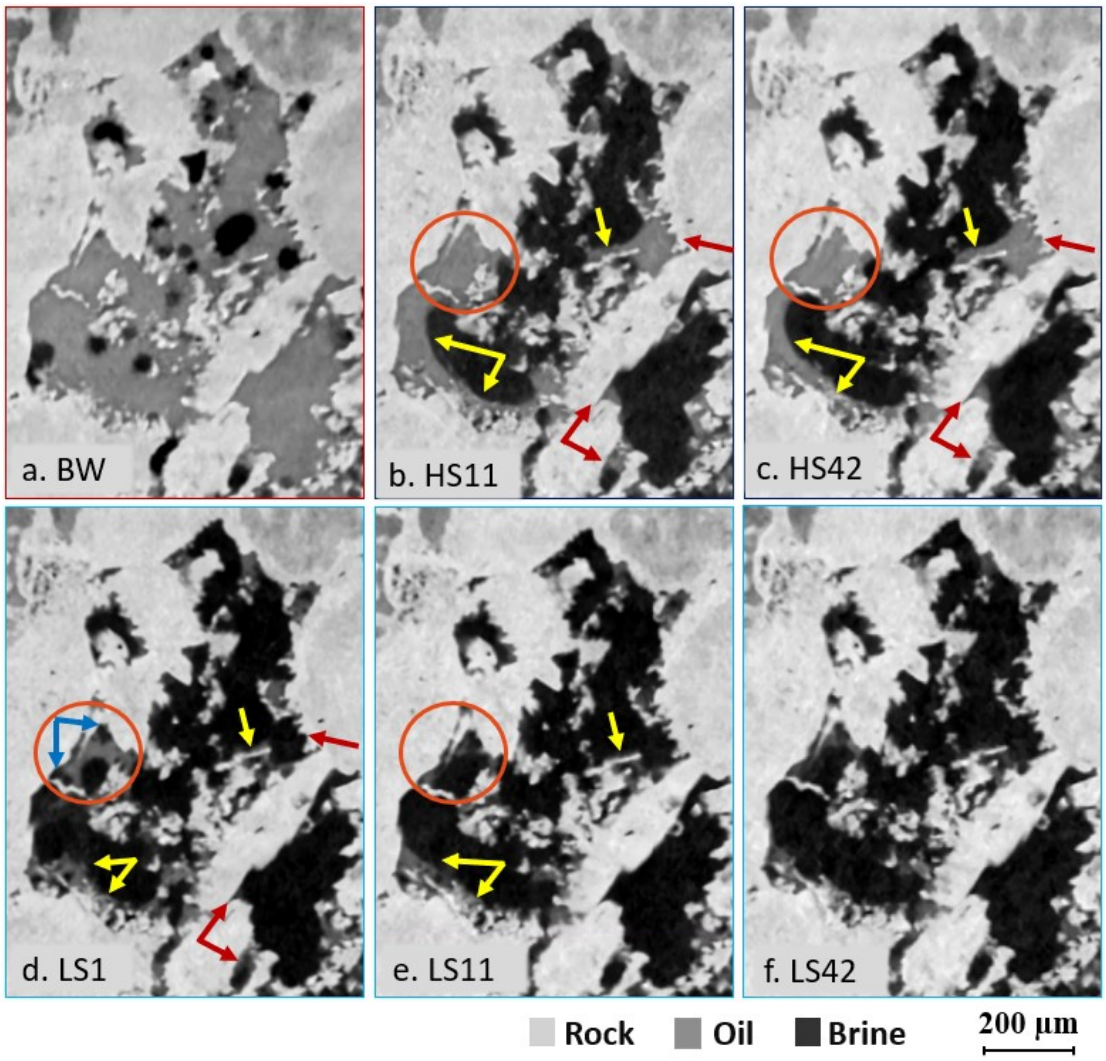

Figure 4.1: Two-dimensional cross-sections from the images illustrating the oil and brine distribution in the pores before waterflooding (a), after 11 and 42 µL/min high salinity (HS) floods (b-c), and after the 1, 11 and 42 µL/min LS floods (d-f). The orange circles show immobile oil in a dead-end pore during HSW which was detached from the rock surface by the growth of water droplets (blue arrows) during LSW. The yellow and red arrows highlight the oil constrained to layers and pore corners, respectively, after HSW and the breakup of these layers and displacement of oil from pore corners after LSW.

To further understand the processes, we examined another region. Figure 4.2 shows cross-sections of the same region of the sample at different time intervals throughout the experiment. Before waterflooding, oil occupied most of the pore space and water was mainly in the centre of large pores. After the various high salinity floods, the remaining oil was found in small-sized pores, in pore corners and along the pore walls. The oil films and layers, shown in red rectangles, spreading across the surface during HS floods showed minimal changes despite the injection of more brine at higher flow rates.

As the low salinity floods started, some remarkable changes were observed. The oil films started to collapse, brine invaded pore corners and smaller pores (green arrows in Figure 4.2), and water droplets formed at the oil/rock surface (blue arrows).

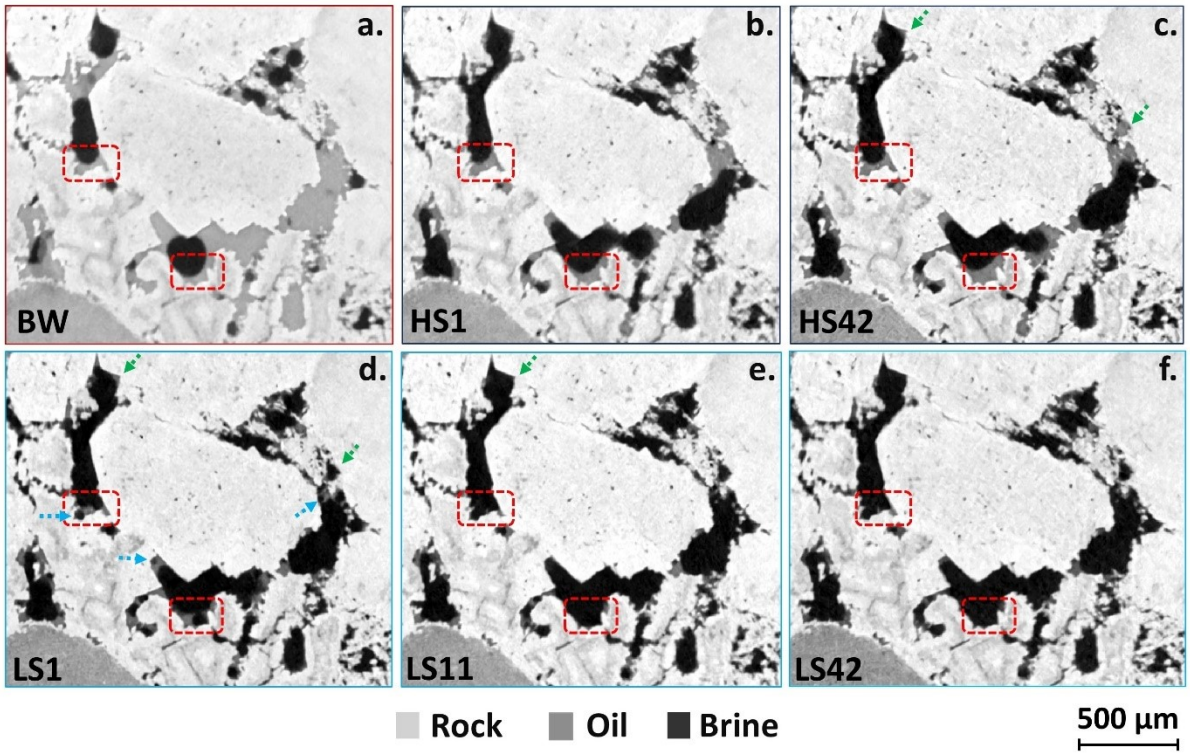

Figure 4.2: Raw images illustrating fluid configurations in the pores before waterflooding (a), after 1 and 42 µL/min high salinity (HS) floods (b-c) and 1, 11 and 42 µL/min LS floods (d-f). The red rectangles show stability of oil films during HS floods and their disintegration after LS injection. The blue and green arrows show the formation of water micro-droplets and the brine invasion of smaller pores, respectively.

In addition to the displacement processes, the images revealed the mechanisms by which oil was displaced during LSW. To investigate these underlying mechanisms further, we had a closer look at individual pores. Figure 4.3 shows different pores within which oil was displaced by two main mechanisms during LSW. From an initially oil filled pore, high salinity brine only displaced oil from the pore centres and, despite injecting 60 pore volumes at increasing flow rates, oil remained attached to pore walls and corners (Figure 4.3a-b). However, when LSW started (Figure 4.3c), brine appeared between the oil and rock surface (blue circles) and the oil in the top pore was mobilised (blue arrows) to the bottom pore, and after 2 days with LSB injection at higher flow rates a thin water film (blue arch) started to grow and detach the oil from the rock surface (Figure 4.3d-e). Oil was also displaced by

another mechanism; the development of water micro-droplets (micro-dispersions). These are small water droplets developing within the oil phase and growing to coalesce and displace the oil. After flooding the sample with high salinity brine for 6 days, no significant change was observed from the initial case (Figure 4.3f-g). During LSW, water micro-droplets started to form both within the oil phase and at the oil/solid interfaces (Figure 4.3h). After two days and more pore volumes of brine injected these droplets grew and coalesced displacing more oil (Figure 4.3i). After a few more days, there was a slight increase in the water volume and a change in the contact angle between the oil/brine interfaces and the rock (Figure 4.3j) suggesting a change in the wetting conditions. Wettability characterization will be discussed further in section 4.3.

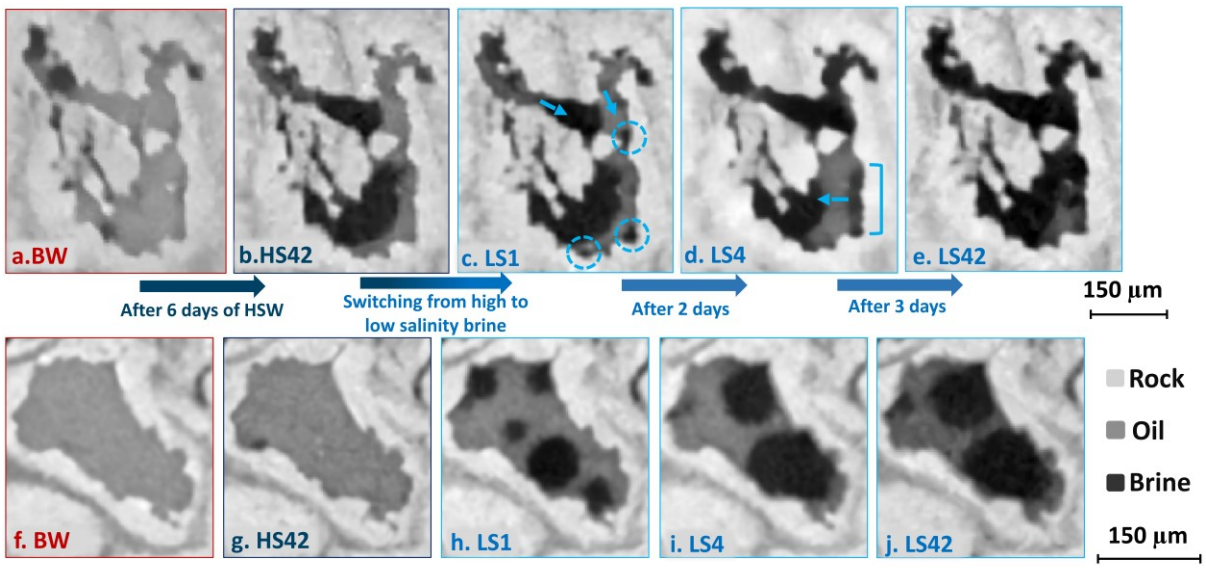

Figure 4.3: Two-dimensional cross-sections from the X-ray images highlighting the mechanisms by which oil is displaced during low salinity waterflooding. (a-e) Oil was displaced from the centre of the pore with HSW. Water appeared at the oil/rock interface after LS1, blue circles, and connected to form a layer detaching the oil after LS4, blue arch. (f-j) Water micro-droplets only started to appear and grow after LSW.

To have a deeper understanding of the role of micro-dispersions in the displacement process, a 3D visualization, extracted from the segmented images, highlights the appearance of these droplets during HSW and their growth as the brine salinity and composition was changed during LSW. The pores were fully occupied by oil before waterflooding (Figure 4.4a). Water micro-droplets did not initially form during HSW (Figure 4.4b) but after the injection of 30 PVs of HSB, some droplets started to appear

(Figure 4.4c). Brine invaded the centre of the two pores at the top while some residual oil was observed in the pore corners. At the end of HSW (Figure 4.4d), and the injection of 60 PVs, a few more droplets formed within the oil phase, while oil remained trapped in pore corners (red arrows). The water droplets grew after the first LS flood (Figure 4.4e) and coalesced resulting in volume displacement of oil at the end of LSW (Figure 4.4f). Moreover, the trapped oil was mobilized.

There could be a connection between the pore-scale displacement processes and mechanisms observed during waterflooding and the properties of the crude oil-brine-rock (COBR) system used in this study. The acidity and the asphaltene content of the crude, the salinity gradient between FB and HSB, as well as the reduced salinity and increased sulphate concentration of the LSB, compared to HSB, are elements that induced the formation and growth of water micro-dispersions within the oil and at the oil-brine interfaces (Emadi and Sohrabi, 2013, Chakravarty et al., 2015, Mahzari et al., 2019). In a secondary LSW experiment, where LSB was injected at initial water saturation into a similar COBR system, the aforementioned mechanisms were rarely observed (Selem et al., 2021b). This can be explained by the large osmotic gradient between the initial (formation) water and low salinity water which likely increases the rate at which micro-droplets develop and coalesce making the process too fast to be captured by X-ray imaging.

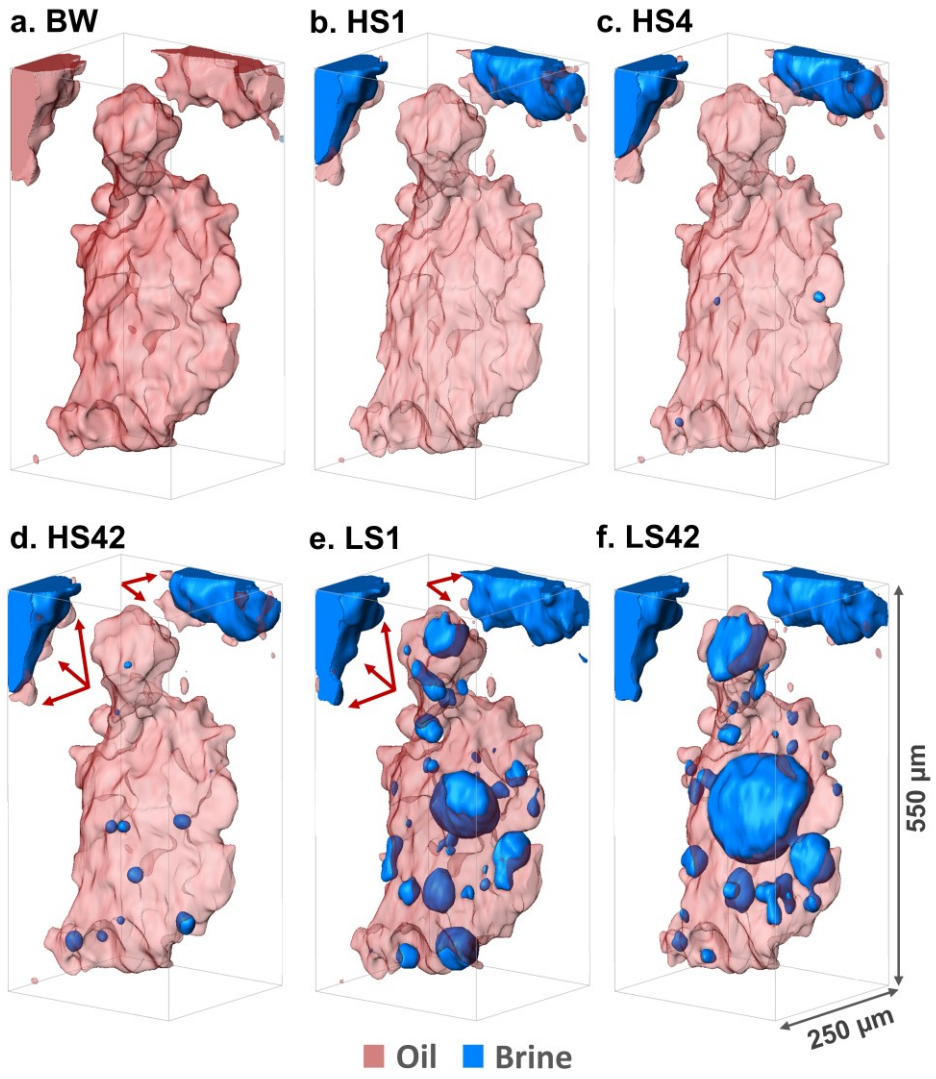

Figure 4.4: A three-dimensional visualization of oil-filled pores before waterflooding (a), and the development of water micro-droplets during HSW (b-d) and their growth during LSW (e-f). The red arrows highlight the displacement of oil trapped in pore corners by the low salinity brine injection. The brine, oil and rock are shown as blue, semi-transparent red and transparent, respectively.

4.2 Pore occupancy

To further understand the configuration of oil and brine across the sample with high and low salinity waterflooding, 3D quantification of pore occupancy was performed. The pore radii are mainly between 10-60 µm (Figure 4.5a), and between 5-35 µm for throats (Figure 4.5b). Initially, oil occupied most of the pore space with brine residing mainly in larger pores (Figure 4.5c) and throats (Figure 4.5i). This fluid distribution signifies oil-wet conditions (Salathiel, 1973, Lin et al., 2021, Selem et al., 2021b).

After HSW, brine displaced oil from relatively larger pores (pore radius > 10 μm), but oil still occupied most of the smaller pores and throats. Additional oil was only displaced when the flow rate was increased, indicating that large regions of the pore space remained oil wet during HSW. This is shown in Figure 4.5d-e for pores and Figure 4.5j-k for throats. During LSW, more oil was displaced from smaller pores (Figure 4.5f-h), which is in line with observations made in section 3.1. The fraction of throats occupied by oil decreased slightly after LSW (Figure 4.5l-n). The brine filling of smaller pores after switching to LSW, even when injected at a low flow rate, can be explained by the mechanisms discussed in the previous section and is characteristic of the low salinity effect and wettability changes. In the secondary LSW study, similar initially oil-wet conditions were detected; however, through LSW, a redistribution of oil from smaller to larger pores was observed which facilitated the recovery of oil as more brine was injected (Selem et al., 2021b). This rearrangement was not observed in the tertiary mode and could be the underlying reason for the difference in recovery factors between the two modes as will be discussed later.

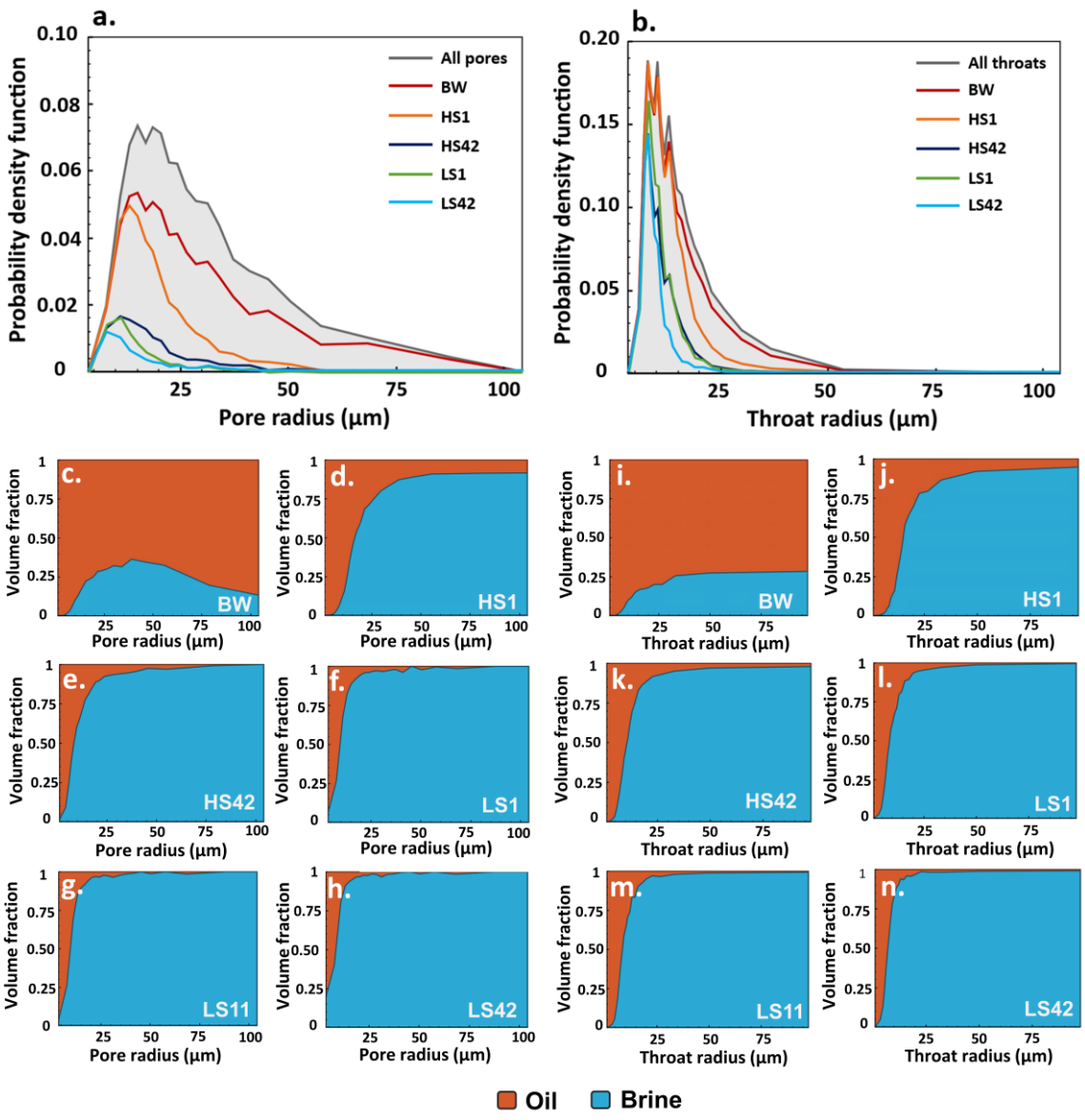

Figure 4.5: Histogram plots of oil-filled pores (a) and throats (b) showing the size distribution of resolved pores and throats and the volume-weighted fraction computed using the generalized pore network extraction tool at different stages of waterflooding. (c-n) Fluid occupancy maps for pores and throats of different radii before waterflooding and for HS and LS waterflooding.

The pore-scale displacement processes and mechanisms observed after LSW, namely the collapse of oil layers, formation of water micro-dispersions and the displacement of oil from pore corners and small pores, could be related to the change in the wettability of the rock from oil-wet conditions before and during HSW towards mixed-wet conditions after LSW.

In the next section, we assess the magnitude of wettability alteration after HSW and LSW by the analysis of interfacial areas, contact angles and curvatures. We will also examine whether there is a relationship between the wettability and the mechanisms discussed hitherto.

4.3 Wettability characterization

The fluid occupancy maps give an indication of the fluid distribution in the pore space, but they only show which fluid occupies the largest fraction of the pore and do not capture the fluids residing in the pore corners or as layers along the pore walls. Therefore, to complement the pore occupancy analysis, we calculated the interfacial area per unit volume between oil-water, water-solid and oil-solid interfaces. The measurements of interfacial area per unit volume in resolved pores are shown in Figure 4.6a. To remove the voxelization artefacts associated with the segmented images, the interfaces were smoothed using Gaussian smoothing (Taubin, 1995). The oil-solid interfacial area decreased to a value equal to that of the water-solid interfacial area towards the end of HSW, while the oil-water interfacial area increased to a maximum value. This can be explained, as discussed in section 4.1, by oil layers covering the oil-wet rock surfaces (Alhammadi et al., 2020). After LSW, a drop in both the oil-solid and oil-water interfacial areas is observed. This is due to the breakdown of the oil layers, formation of water micro-droplets, and the displacement of oil from pore corners and dead-end pores allowing the brine to directly contact the rock surface resulting in a change in wettability and further mobilization of oil.

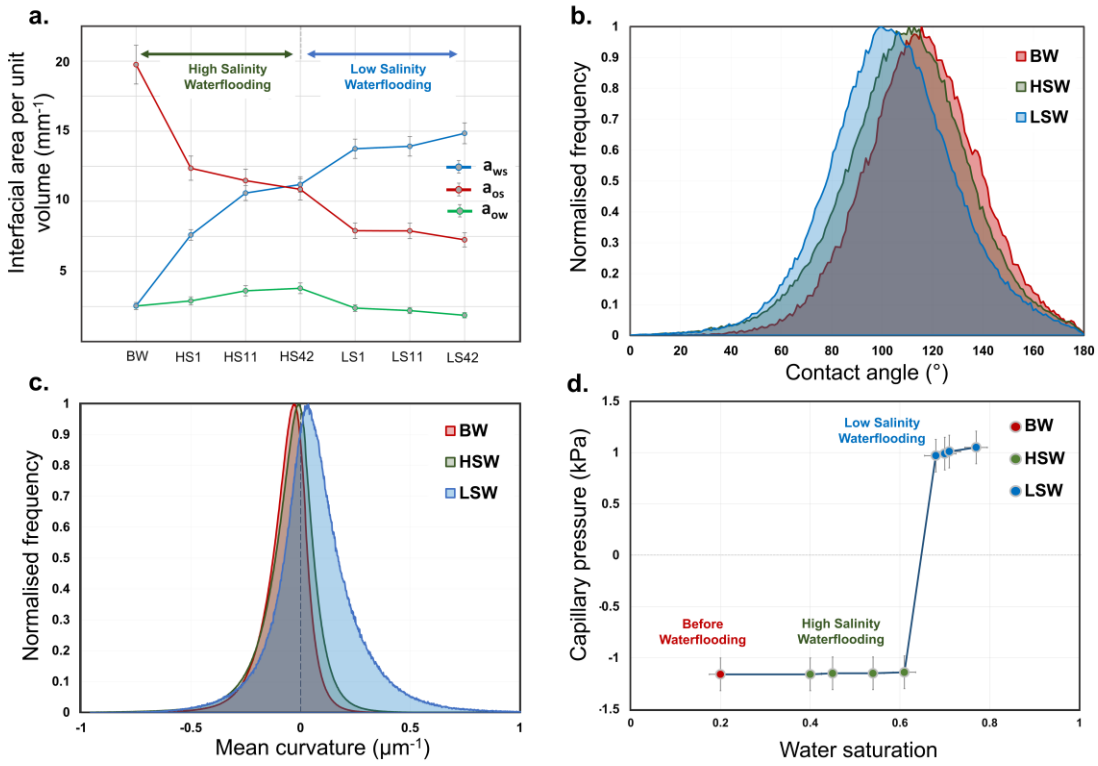

Figure 4.6: (a) Oil-water, water-solid and oil-solid interfacial areas per unit volume: a_{ow}, a_{ws} and a_{os} respectively. Histograms of contact angle distributions (b) and mean curvatures (c) measured from the segmented 3D images. (d) Capillary pressure values calculated from the mean oil/brine interfacial curvatures before waterflooding (BW) and after different steps of high and low salinity waterflooding. The error bars indicate the uncertainty in the segmentation and the measurements of curvature and saturation.

To further evaluate the effect of high and low salinity water injection on wettability with the change in flow rate, contact angles and curvatures were measured using oil-brine interfaces. The spatial distribution of contact angles on the contact line between oil, water and rock was used to assess the wettability (Andrew et al., 2014a, Alhammadi et al., 2017). *In situ* contact angle and curvature measurements histograms showed a shift after HSW and LSW. Initially, the mean contact angle was 115° ± 18° which changed only slightly to 112° ± 20° at the end of HSW showing the oil-wet nature of the sample. After the LSW, a substantial shift occurred with a mean contact angle of 102° ± 15° (Figure 4.6b).

In addition to calculating interfacial areas, the oil-water interfaces were used to estimate curvatures which can reveal details about rock wettability, local capillary pressures, and fluid connectivity. The

smoothed oil-water interfaces were used to extract the two principal curvatures (κ_1 and κ_2), from which the mean curvature κ is calculated as an average. Before waterflooding, and during HSW the mean curvature values are negative (Figure 4.6c). The negative curvature values can also be explained by the morphology of the fluid interfaces in Figure 3a-c where brine bulged into oil indicating an oil-wet system. With LSW, the fraction of the positive curvatures increases explaining the shift in the mean curvatures values.

The changes in the contact angles and mean curvature values after switching from high to low salinity brine suggest that the rock surfaces display a shift from the initial oil-wet conditions towards more mixed-wet conditions.

The local capillary pressure was calculated using the Young-Laplace law:

$$P_c = 2\sigma\kappa \tag{4.1}$$

where σ is the oil-water interfacial tension and κ is the average curvature of the interface between oil and water. The mean curvature values, were used to calculate the capillary pressure of the system (Armstrong et al., 2012, Lin et al., 2019, Alhammadi et al., 2020) before waterflooding and after various injection steps (Figure 4.6d). Negative capillary pressure values before waterflooding and through HSW, are reflective of oil-wet conditions. However, after LSW, the values showed a change towards increased water-wetness. With an increase in capillary pressure, brine can invade and displace oil from smaller pores. The wettability change is more significant than the normal trend of capillary pressure, namely a decrease with increasing water saturation, seen when the wettability remains constant throughout the displacement.

4.4 Fluid connectivity

Curvature measurements were also used to evaluate fluid connectivity from the product of the two principal curvatures (κ_1 and κ_2), defined as the Gaussian curvature (Gauss and Pesic, 2005, Berger and Gostiaux, 2012). It has a negative value for well-connected phases and the opposite if the phases are poorly connected. To better understand the phase connectivity in the system, principal curvatures were

categorized into three groupings: both positive ($\kappa_1 > 0$, $\kappa_2 > 0$), both negative ($\kappa_1 < 0$, $\kappa_2 < 0$), and of opposite signs ($\kappa_1\ \kappa_2 \leq 0$). Initially, the curvature distributions show predominantly negative principal curvatures, i.e., positive Gaussian curvature, indicating a lack of connection of the water phase within the pore space (Figure 4.7a). A similar distribution is shown after HSW (Figure 4.7b) where, despite the increase in water saturation, the oil phase remains better connected through oil layers, as discussed in sections 3.1 and 3.2, indicative of the oil-wet state of the system (Lin et al., 2019). After LSW, most of the curvatures have one positive and one negative value, i.e., a negative Gaussian curvature, Figure 4.7c-d. The increase in interfaces with two positive principal curvatures (the blue histogram) corresponds, unlike in HSW, to poorly connected oil in water-wet regions. This indicates a mixed-wet, or weakly water-wet, system with reasonable connectivity of both phases in the pore space (Lin et al., 2019, Alhammadi et al., 2020, Gao et al., 2020).

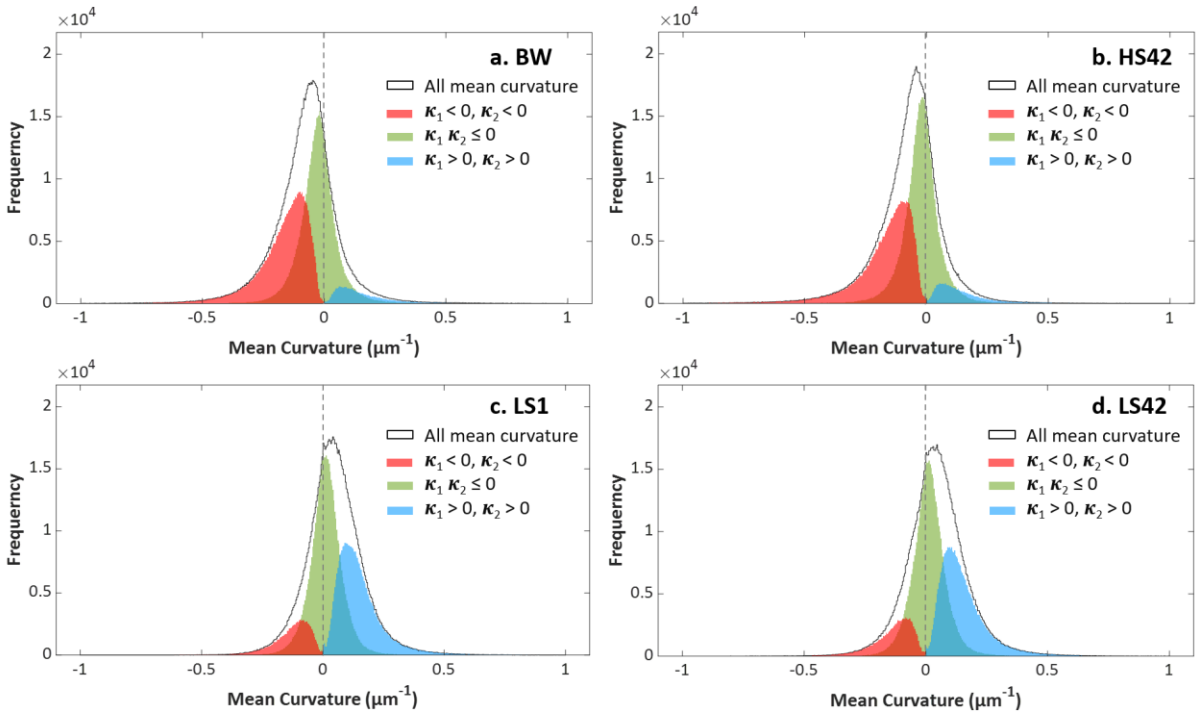

Figure 4.7: Measured oil-brine curvature distribution (a) before waterflooding (BW), (b) after the last high salinity flood (HS42), (c) after the first low salinity flood (LS1), and (d) after the last low salinity flood (LS42) using the principal curvatures (κ_1 and κ_2) extracted from smoothed oil-water interfaces. The

black curve shows the mean curvature distribution. The red, green, and blue histograms show the distributions of κ_1 and κ_2 values that are both negative, of opposite signs, and both positive respectively.

To further understand the fluid connectivity, Figure 4.8 shows how different brine ganglia in one part of the rock sample became connected during waterflooding. Initially, water clusters were dispersed and occupied the centre of the pores (Figure 4.8a). During HSW, water micro-droplets started to develop, albeit slowly (Figure 4.8b-d). As LSW started, water micro-droplets grew and connected forming continuous water layers (Figure 4.8e-f). The development of the blue brine blob, in the top right corner, highlights this process. The pore encircled in red was fully oil-saturated before waterflooding and after the first HS flood (Figure 4.8a-b). Water micro-dispersions started to form only after 3 days, and 30 pore volumes, of HSB injection (Figure 4.8c). Injecting more HSB did not result in a significant difference (Figure 4.8d). However, switching to LSB triggered the growth of water micro-dispersions and a substantial increase in their size was observed (Figure 4.8e-f). For example, the volume of the main brine ganglion in Figure 4.8, shown in blue, has increased by four times after 60 PVs of HSB injection. After the first LS flood, 10 PVs of LSB injection at 1 μL/min, the ganglion size further increased by more than seven times, and the injection of more LSB resulted in a small volume increase. The ganglion volume increased due to the growth of the ganglion itself and by the coalescence with nearby droplets resulting in the displacement of oil as discussed in section 4.1.

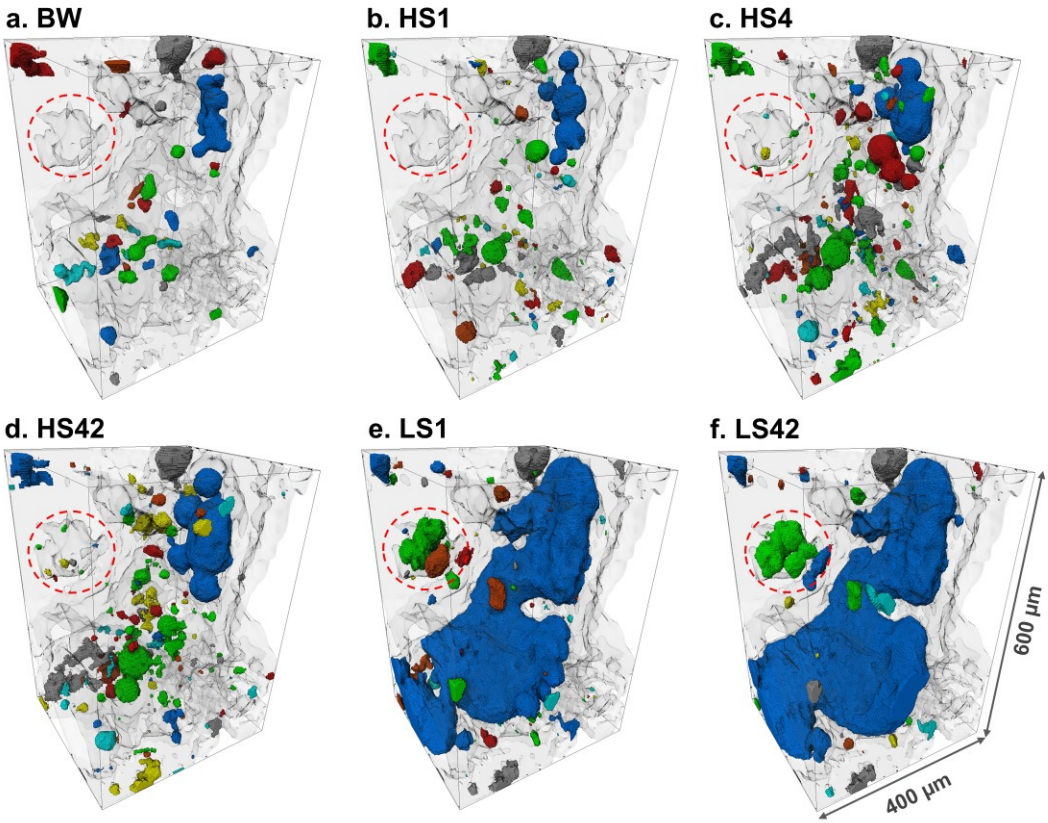

Figure 4.8: Three-dimensional visualizations of the development and connection of water domains before waterflooding (a) after HS floods (b-d) and LS floods (e-f). Different colours represent different connected brine blobs. Oil is transparent and rock is semi-transparent. The volume, in units of 10^6 µm^3, of the largest brine ganglion, highlighted in blue, at the different stages is 0.34, 0.48, 0.86, 1.37, 10.7 and 11.32, respectively. The red circles show the slow formation of water micro-droplets during HSW and the fast rate at which they developed and coalesced during LSW.

4.5 Oil saturation and recovery profiles

The initial water saturation, before waterflooding, was calculated from the segmented 3D image as 11%. The saturation profiles of oil across the sample at different stages are shown in Figure 4.9a, a more detailed figure is shown in the appendix (Figure 9.11). The oil saturation decreased with time during the HSW, especially after the highest flow rate injection (HS42), indicating an oil-wet sample (Piñerez Torrijos et al., 2016). Oil was displaced by the invasion of HSB to the centre of pore space, as discussed in sections 4.1 and 4.2. By the end of HSW, 57% of the original oil in place (OOIP) in resolved pores was recovered, as shown in Figure 4.9b. With LSW, more oil was recovered. After 10 pore volumes (PVs) of LSB were injected at 0.001 mL/min, an additional 3% of oil was recovered. By the

end of LSW, the ultimate recovery reached 66%, i.e., LSW resulted in an incremental oil recovery of 9%.

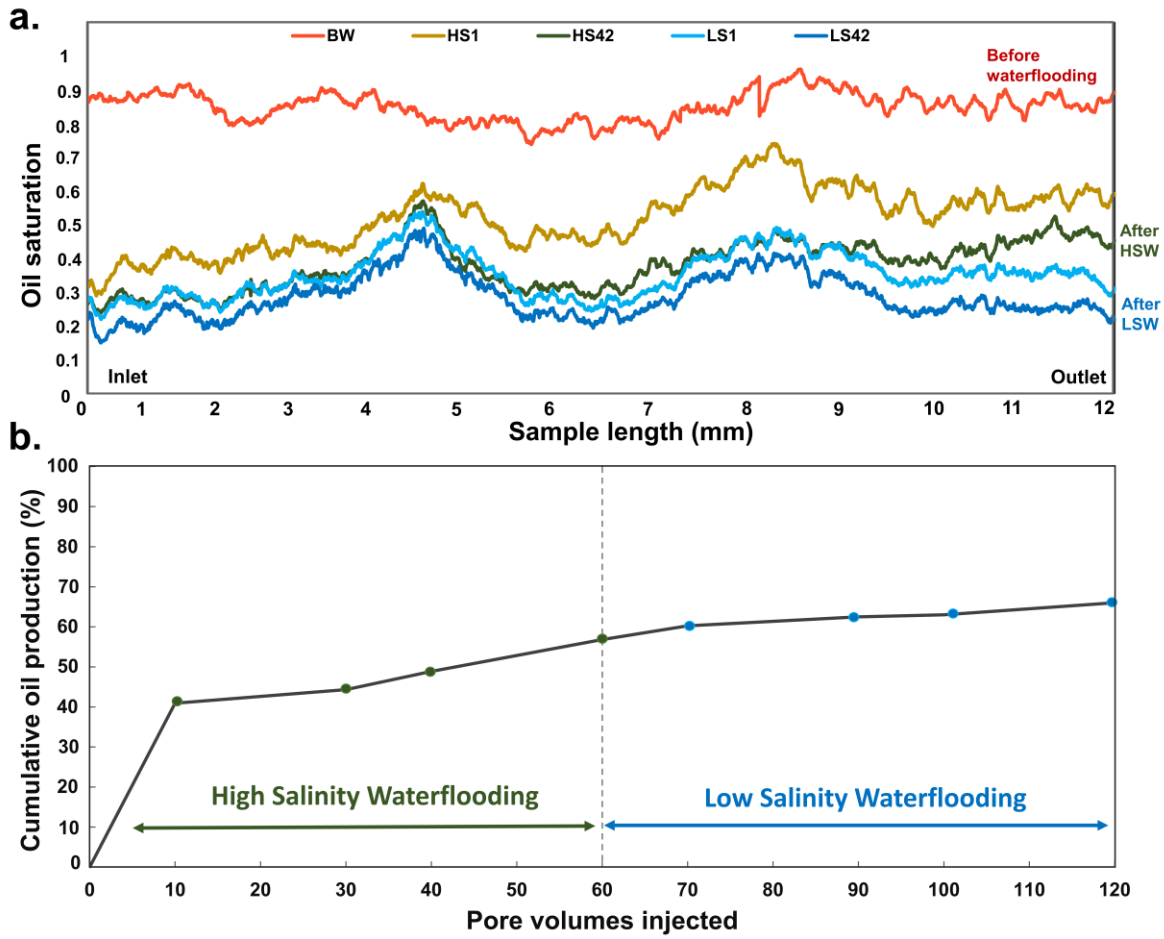

Figure 4.9: (a) Oil saturation profiles across the sample before waterflooding (BW) and at different stages of HSW and LSW. (b) The cumulative oil recovery at different points of waterflooding.

The low salinity effect was not instant; there was first a rearrangement of detached oil in the pore space before it was displaced towards the outlet. Two phenomena were observed that led to oil detachment and mobilization: the formation of water micro-droplets within the oil phase and at the oil/solid interfaces, and then the merging of water domains forming thin water films. Figure 4.3a indicates that the expansion of the water film detaching the oil followed by the reconnection of the oil ganglia occurred after 2-3 days of LSB injection.

4.6 Summary

This study employed X-ray imaging to monitor the *in situ* evolution of low salinity effects in a natural system and analyzed the accompanying changes in rock wettability and their impact on oil recovery.

The analysis of contact angles, curvatures, capillary pressures, and pore occupancy showed a transition in rock wettability from oil-wet to mixed-wet due to LSW, resulting in improved microscopic sweep efficiency through increased capillary forces. The distribution of the oil phase, before and during the HS floods, in dead-end regions of the pore space and expanding along the pore walls is indicative of the relatively strong propensity of the rock surface to oil, hence high contact angle and negative capillary pressure values. After LS floods, the development of water micro-droplets in oil and at the oil/rock interface as well as the expansion of the thin water films between the oil and rock surface were observed. Figure 4.3 indicates that the expansion of the water film detaching the oil followed by the reconnection of oil ganglia occurred after the third LS flood, i.e. the injection of 30 pore volumes of LSB and an increase in the flow rate.

The asphaltene content and the acidity of the crude oil as well as the relatively higher sulphate content of the low salinity brine are elements that are consistent with our indication of the formation of water micro-dispersions and the expansion of electric-double-layers. Double layer expansion and water micro-dispersion are considered the underlying mechanisms for the wettability alteration and ultimately the low salinity effect resulting in a 9% increase in oil recovery. Analyses of contact angles, curvatures, capillary pressures, and pore occupancy indicated a shift in the rock wettability to more water-wet conditions because of LSW.

This extensive LSW investigation sheds light on previously observed pore-scale displacement mechanisms, especially the development of micro-dispersions, in micro-model tests. These findings can facilitate interpretation of results from Darcy and molecular scale experiments, closing the gap between the vastly different length scales given a similar crude oil, brine and rock system is tested. Finally, the quantitative experimental measurements presented can be used for pore-scale modelling validation and upscaling in EOR projects.

In the next chapter we will investigate the differences in mechanisms, displacement efficiency and variations in recovery factors when low salinity brine is injected in secondary mode, i.e., when the there is no sea water/high salinity brine injection. We will compare the wettability characterization results and investigate the efficiency improvement, if any, associated with the direct injection of low salinity brine into the oil-wet/wettability altered rock.

Chapter 5

Imaging and analysis of secondary low salinity waterflooding in Estaillades limestone at reservoir conditions

In this chapter we provide experimental observations of secondary low salinity waterflooding in the same quarry rock used in the previous chapter. The experimental protocol is described in chapter 3. The segmented three-dimensional pore-scale images were used to quantify fluid saturation and oil recovery and to perform pore-by-pore occupancy analysis after low salinity waterflooding. To assess the impact of the low salinity effect on rock wettability with increasing brine injection rate, we measured contact angles and curvatures on oil-brine interfaces extracted from the micro-CT images and calculated capillary pressure. We end by placing the analyses from this study and the previous in a practical context by discussing implications for enhanced oil recovery with LSW.

5.1 Fluid distribution and oil recovery

At the end of ageing, the value of irreducible water saturation in macro-pores measured from the segmented image was 12% as oil occupied most of the pore space (Figure 5.1a), similar to the initial water saturation of 11% in the previous chapter. Again, as in chapter 4.1, we see the interesting phenomenon that water has moved from what we hypothesize are narrower regions of the pore space to occupy some of the larger oil-wet pores. As mentioned previously, low salinity brine was then injected at six different flow rates (10 pore volumes at each rate) under capillary-force dominated conditions.

At the early stages of waterflooding, brine preferentially invaded larger pores whereas smaller pores remained uninvaded (Figure 5.1b-c): this is expected for an oil-wet rock, where water displaces oil in the larger oil-wet pores through forced injection (Blunt, 2017). After the third injected flow rate (4 μL/min), a different behaviour was observed, where brine started to invade smaller pores and oil re-emerged in larger pores. Remember that we only consider the macro pores resolvable in the image in this analysis. This is consistent with a change in wettability to be more water-wet: brine now preferentially invades the smaller water-wet portions of the pore space, whereas the displaced oil occupies the larger pores. This can be seen when comparing the highlighted areas in Figure 5.1c-d. This pattern continued into the next injection step (11 μL/min), with oil and brine occupying both smaller and larger pores (Figure 5.1e); however, as the waterflood rate further increased brine displaced most of the oil (Figure 5.1f).

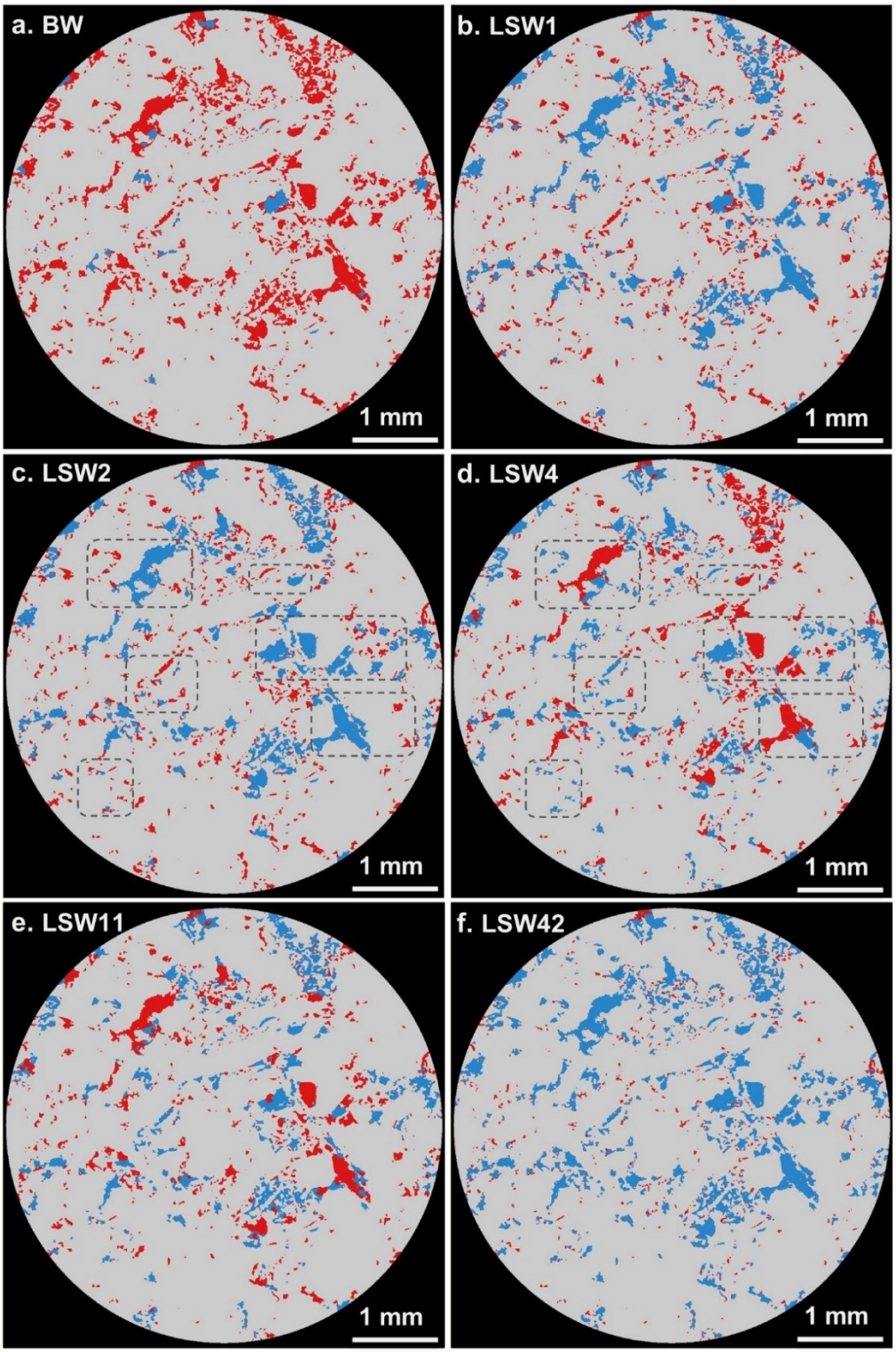

Figure 5.1: Two dimensional cross-sectional views of the segmented three-dimensional images of oil (red), brine (blue) and rock phase (grey). (a) Before waterflooding (BW) oil occupied most of the pore space with a saturation of 88%. (b-c) After the first two floods, at 1 and 2 µL/min, brine mainly invaded larger pores. (d-e) After the intermediate floods, 4 and 11 µL/min, fluids redistribution was observed. The highlighted areas show displacement of oil from small pores, with larger pores reoccupied by oil as more

pore volumes of low salinity brine are injected at higher flow rates. (f) After the last flood, 42 μL/min, brine displaced most of the remaining oil.

To further examine the effect of LSW across the whole sample and quantify oil recovery, saturation values were determined from the segmented images. After the first two injection rates, more than half of the volume of oil has been displaced across the sample except from the part near the outlet where there was a higher oil saturation, Figure 5.2a. LSB may not have fully displaced formation brine to come in contact with oil and alter wettability in this region of the sample, explaining the high remaining oil saturation. As more low salinity brine was injected at higher rates, 4 and 11 μL/min, a significant amount of oil was displaced from this region near the outlet; however, an increase in oil saturation was observed in the middle part of the sample. This is due to the displacement of oil from smaller into larger pore elements controlled by local wettability and capillary pressure, as shown previously in the segmented 3D images in Figure 5.1. This will be discussed further in the pore occupancy analysis in the next section. Two bump rates, 22 and 42 μL/min were then applied to remove any capillary end effects and appropriately assess the remaining oil saturation at the end of the waterflood. At the end of waterflooding, a more uniform saturation profile was achieved with an ultimate recovery value of 85% of the oil initially in place in macro-pores, see Figure 5.2b.

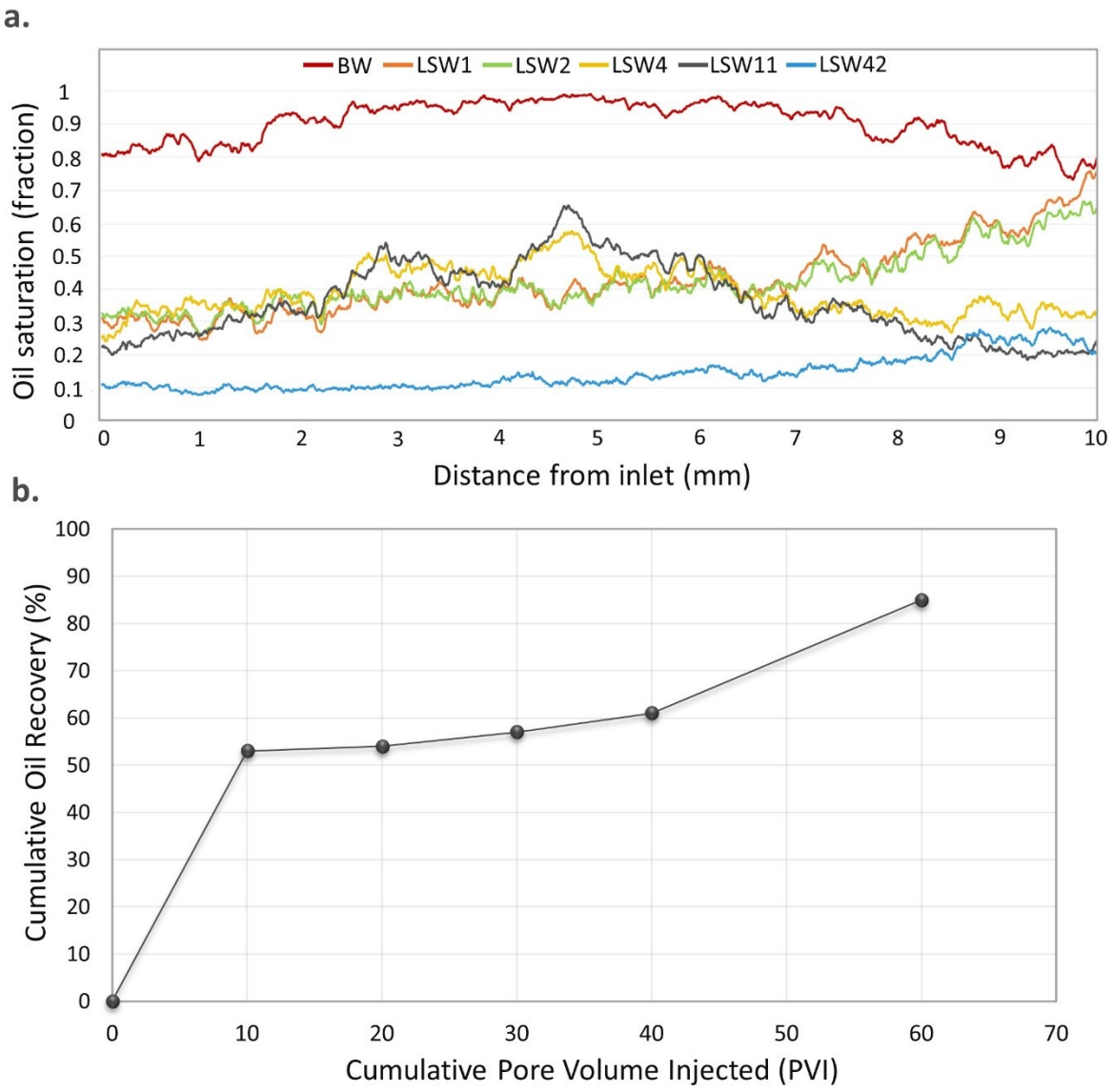

Figure 5.2: (a) Oil saturation profiles across the sample (flow direction from left to right) before waterflooding (BW) and at different stages of LSW, namely 1, 2, 4, 11 and 42 µL/min. (b) Oil recovery as a percentage of the oil initially in place in macro-pores. A total of 60 pore volumes (10 at each flow rate) of low salinity brine were injected.

5.2 Fluid occupancy

Mapping of pore-scale fluid occupancy is essential to build a better understanding of the fluid configuration in the pore space and to test whether there were substantial changes in both pore and throat occupancy due to low salinity injection, as outlined in chapter 4. The size distribution of resolved pores and throats and the volume-weighted fraction of oil-filled pore elements computed using the generalized pore network extraction tool are shown in Figure 5.3. The pore radii are mainly between

15-60 μm (Figure 5.3a), and between 5-30 μm for throats (Figure 5.3b). Before waterflooding, oil occupied almost all the pore elements with brine residing mainly in larger pores (Figure 5.3a and c) and throats (Figure 5.3b and i). This fluid distribution is characteristic of oil-wet conditions (Salathiel, 1973, Lin et al., 2021). After the first two waterfloods, brine displaced oil from large and medium-sized pores (pore radius > 20 μm) whereas most of the small pores remained filled with oil, Figure 3d and e.

As more brine was injected at higher rates (4 and 11 μL/min; LSW4 and LSW11), there was no significant increase in recovery, Figure 5.2b (between 30 and 40 pore volumes injected), but brine invaded some smaller pores and oil occupied larger pores, Figure 3f and g. This redistribution has not been captured in previous studies (Bartels et al., 2017b), as well as in the tertiary LSW, chapter 4, and is consistent with a shift towards more water-wet conditions. This fluid configuration where both oil and brine fill large and small pores is consistent with a mixed-wet state with both oil-wet and water-wet regions of the rock (Jadhunandan and Morrow, 1995a, Blunt, 1997, Gao et al., 2020, Scanziani et al., 2020): brine preferentially displaces oil from the smaller water-wet elements, while oil filled larger pore elements. In regions of the pore space that remained oil-wet, oil was not displaced until the flow rate increased. After the bump rates, brine had invaded the majority of the pore elements, with some oil remaining in small and large pores, Figure 5.3h. A similar tendency of brine filling and oil redistribution was observed in throats, see Figure 5.3i-n. The brine filling sequence and oil rearrangement observed during waterflooding are indicative of alteration of the rock wettability by low salinity brine from oil-wetting to a mixed-wetting state.

In the next section, we further investigate this understanding through the analysis of contact angle and curvature measurements to assess the magnitude of wettability alteration during low salinity waterflooding.

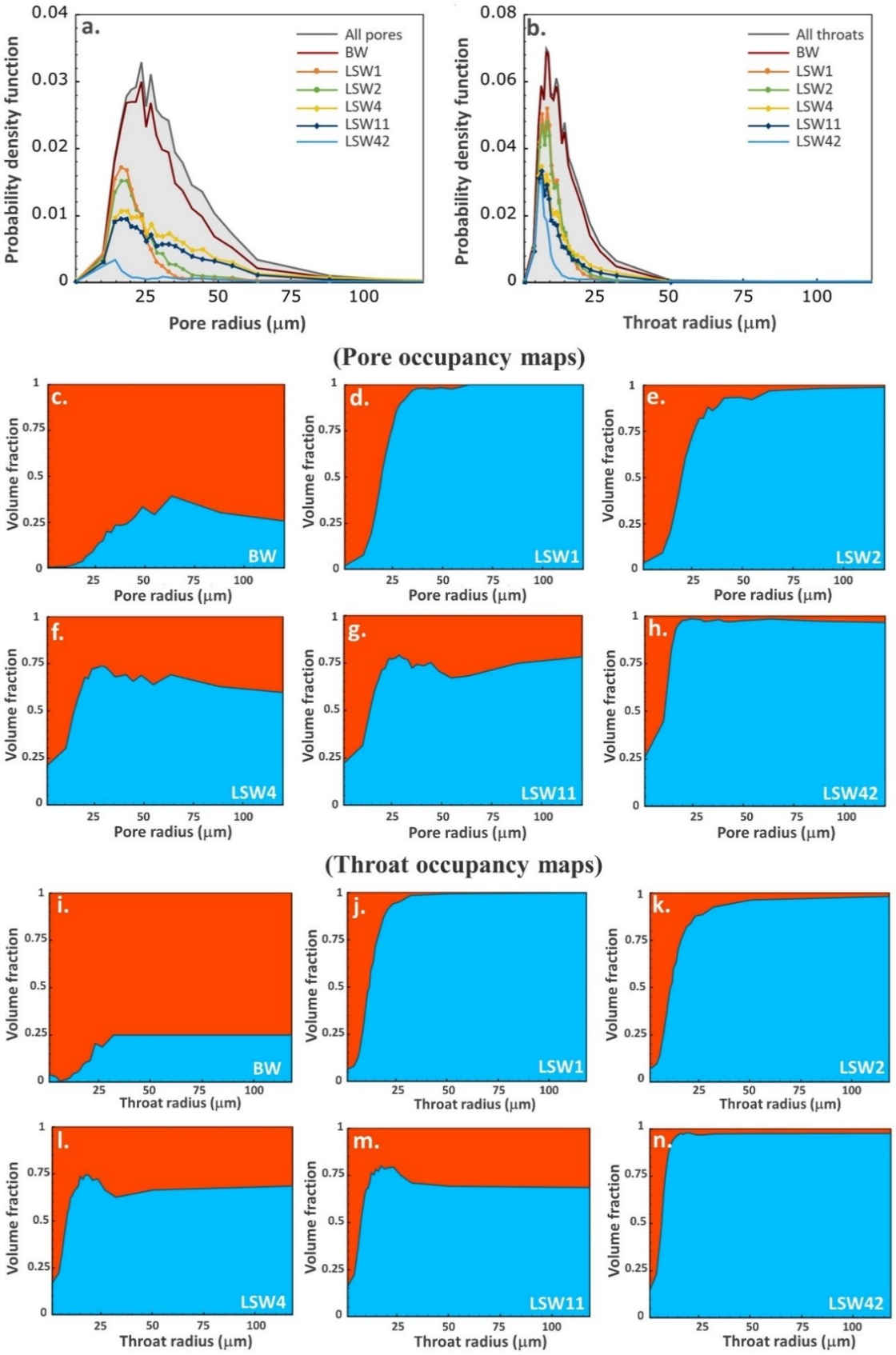
a.
All pores
BW
LSW1
LSW2
LSW4
LSW11
LSW42
Probability density function
Pore radius (μm)
b.
All throats
Throat radius (μm)
(Pore occupancy maps)
c.
d.
e.
f.
g.
h.
Volume fraction
(Throat occupancy maps)
i.
j.
k.
l.
m.
n.

Figure 5.3: (a-b) Histogram plots of oil-filled pore elements showing the probability density function (PDF) distribution at different stages of waterflooding. (c-n) Pore and throat occupancy maps showing the volume fraction of pores and throats of different radii occupied by oil (red) and brine (blue).

5.3 Contact angles, curvatures, and capillary pressure

Contact angle and curvature measurements were performed to quantify wettability changes in large 3D volumes of the complex pore space. Wettability can be inferred from the estimated spatial distribution of contact angles between the fluids within the pore space, also known as the geometric contact angle (Andrew et al., 2014a, Alhammadi et al., 2017). An illustration of the contacts between oil, brine and rock, shown in Figure 5.4a-d, shows that the low salinity brine was observed to be initially bulging into oil in an oil-wet pore. However, with the progress of the waterflood, the oil-brine interface gradually changed to eventually indicate a contact angle close to 90°, reflecting an alteration in the local wetting state. We hypothesize that this is the origin of the increase in recovery, since the flow rates remain in the capillary-dominated regime.

The distribution of *in situ* contact angles between oil and water was measured throughout the displacement using the automated method on a sub-volume of size 1.5×1.5×1.5 mm^3. This sub-volume is located in the top half of the sample, Figure A1.1 in appendix A1. The contact angle distributions are shown in Figure 5.4e. We observe that the mean contact angle before waterflooding, based on over 50,000 measurements, has a value of 124 ± 23°, indicating oil-wet conditions and confirming the success of the ageing process. The contact angle distributions after the brine injection steps show a shift towards water-wetness and a decrease in the mean contact angles. This agrees with the oil redistribution observed from the pore occupancy analysis, Figure 5.3. At the end of waterflooding, a further shift in the measured contact angles distribution was observed with a mean value of 108 ± 23°, based on over 100,000 measurements, see Table 3.5. This change in the contact angle distributions and mean values suggest that the rock, under the effect of low salinity, now displays a mix of water-wet and oil-wet surfaces (AlRatrout et al., 2018).

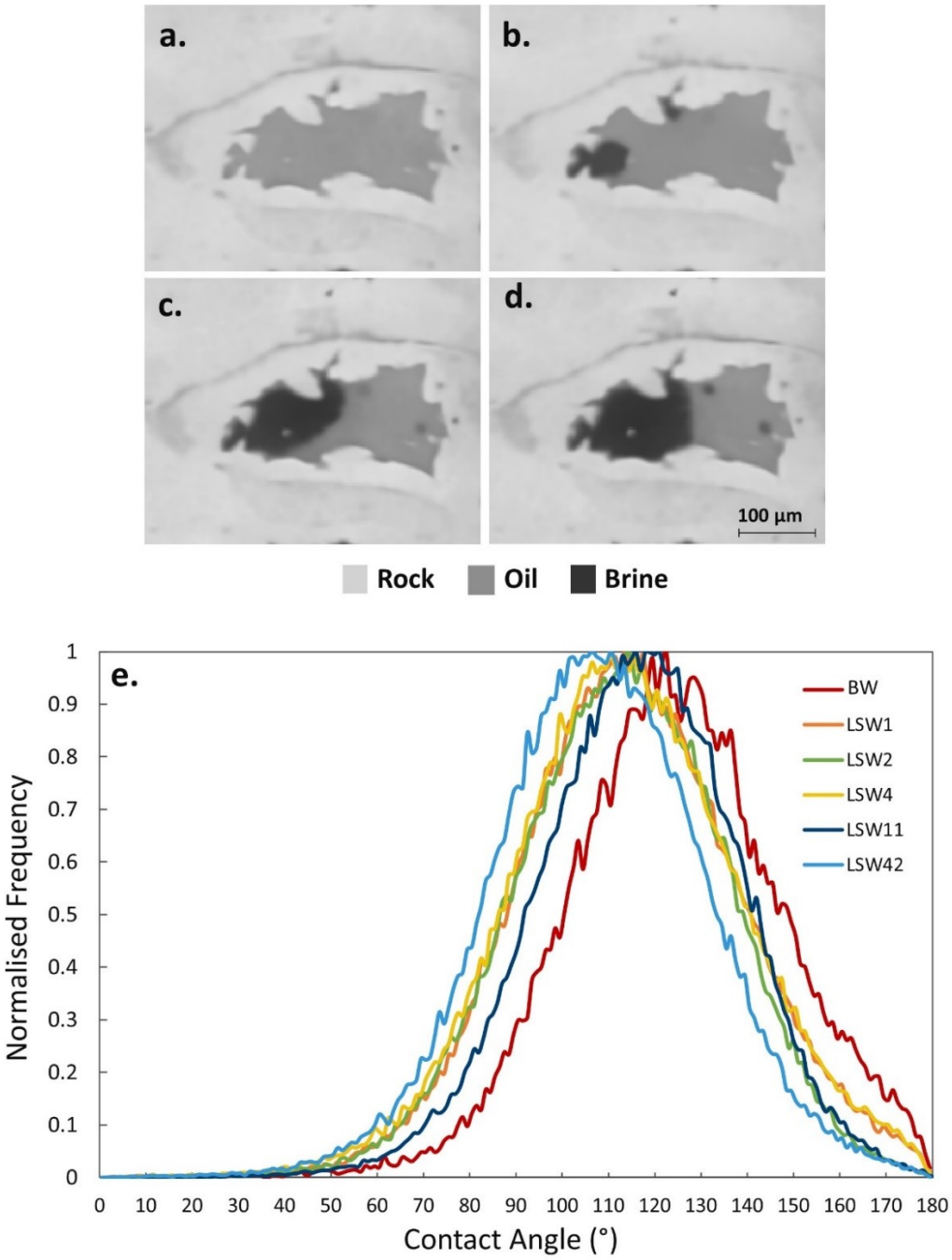

Figure 5.4: (a-d) Two-dimensional raw images illustrating the changes in contact between the fluids and rock in an oil-wet pore before waterflooding (a) and after an injection of 20, 30 and 40 pore volumes of low salinity water (b-d) respectively. (e) Histograms of the *in situ* contact angle distributions measured on a sub-volume extracted from the segmented 3D images. The 3D pore-scale images were acquired by X-ray micro-tomography with a voxel size of 2.9 µm.

Curvatures of the oil-brine interfaces were captured to reveal details about rock wettability and fluid connectivity as well as to calculate local capillary pressures. Oil-brine interfaces were extracted from

the segmented images and smoothed to measure mean curvature values. The mean curvature κ was calculated as the average of the two principal curvatures (κ_1 and κ_2) obtained from the smoothed interfaces, see Figure 5.5. Before waterflooding, the principal curvatures are mainly negative resulting in negative mean curvature values. This is consistent with the morphology of the fluid interfaces with water bulging into oil forming ball-shaped structures, see Figure 5.5a-b. At the end of waterflooding, there is a mixture of both positive and negative curvatures with roughly equal fractions, and hence a less negative mean curvature value, as shown in Figure 5.5c-d. The distributions, in Figure 5.5e, show a shift in the mean curvature value from a negative value before waterflooding into values close to zero after low salinity injection.

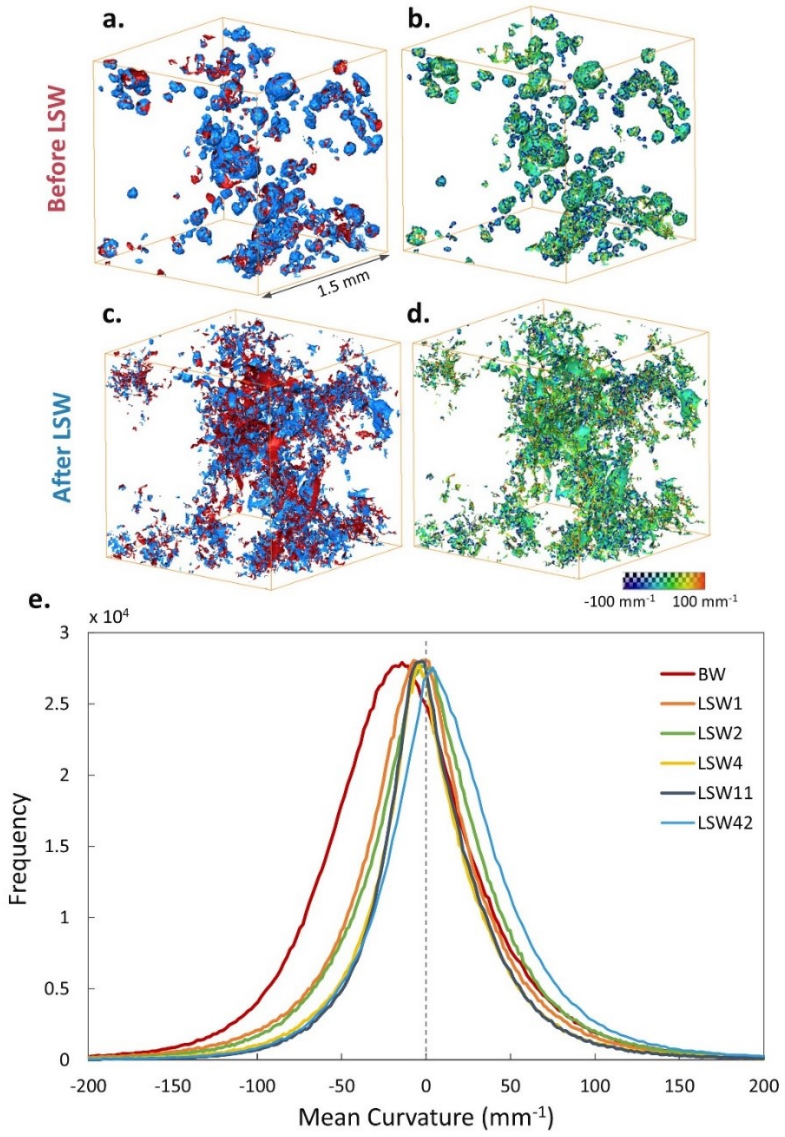

Figure 5.5: Three-dimensional view of smoothed oil-brine interfaces, from a 1.5 mm3 sub-volume, before and after waterflooding (a and c) and their measured mean curvatures (b and d). Histograms of the mean curvature values measured before and throughout waterflooding (e). The interfaces and mean curvatures were extracted from 3D X-ray images using commercial image analysis software, Avizo 9.5 (https://www.fei.com/software/amira-avizo/).

5.4 Capillary pressure and fluid connectivity

As in chapter 4, the capillary pressure was calculated from the curvature measurements using the Young-Laplace law:

$$P_c = 2\sigma\kappa \tag{5.1}$$

where σ is the oil-brine interfacial tension and κ is the mean curvature of the interface. The mean values of the distributions shown in Figure 5.5e were used to characterize the capillary pressure of the system (Armstrong et al., 2012, Lin et al., 2019, Alhammadi et al., 2020) before waterflooding and after each injection step, see Figure 5.6a. The negative capillary pressures are consistent with the measured mean curvature values. A strongly negative capillary pressure before waterflooding is a characteristic of predominantly oil-wet media. Figure 5.6b shows this oil-wet state where a brine ganglion is surrounded by oil in a large pore. Negative pressure values signify a forced displacement where brine must be, on average, at a higher pressure than oil to induce flow over oil-wet surfaces. At this stage, brine can only displace oil from large oil-wet pore elements, Figure 5.6c. However, as low salinity brine is injected capillary pressure values become less negative indicating a lower threshold entry pressure. Only then brine can invade smaller water-wet pores and throats, see Figure 5.6d-e. This change in capillary pressure suggests that the rock wettability has been modified after LSW.

Upon initial examination, Figure 5.6a appears to show a counter-intuitive, or indeed non-physical, trend of capillary pressure with saturation: normally capillary pressure decreases with increasing water saturation (Blunt, 2017). However, the reason for capillary pressure increasing with saturation is because the wettability changes during the displacement. That is, the normal decreasing trend with increasing saturation is outweighed by the impact of a change in wettability and average interfacial curvature, as shown in Figure 5.5e.

In addition to examining wettability and capillary pressure, curvatures can be used to evaluate fluid connectivity from the product of the interfacial curvatures in orthogonal directions: the Gaussian curvature (Gauss and Pesic, 2005, Berger and Gostiaux, 2012). In the case of well-connected phases, the Gaussian curvature will be negative, and vice versa. To assess connectivity, principal curvatures were sorted into three categories: $\kappa_1 < 0$, $\kappa_2 < 0$; $\kappa_1\, \kappa_2 \leq 0$ and $\kappa_1 > 0$, $\kappa_2 > 0$. Before waterflooding, there is a broader distribution with primarily negative principal curvatures, Figure 5.7a. When the interfaces have two negative principal curvatures, i.e. positive Gaussian curvature, this indicates an oil-wet system with the water phase poorly connected in the pore space (Lin et al., 2019); an opposite of what is observed in water-wet cases (Gao et al., 2020). After low salinity flooding, the majority of the

curvatures have one positive and one negative value, i.e. a negative Gaussian curvature, Figure 5.7b. This implies a mixed-wet system with good connectivity of the phases in the pore space (Lin et al., 2019, Alhammadi et al., 2020, Gao et al., 2020) which results in enhanced oil flow and better recovery.

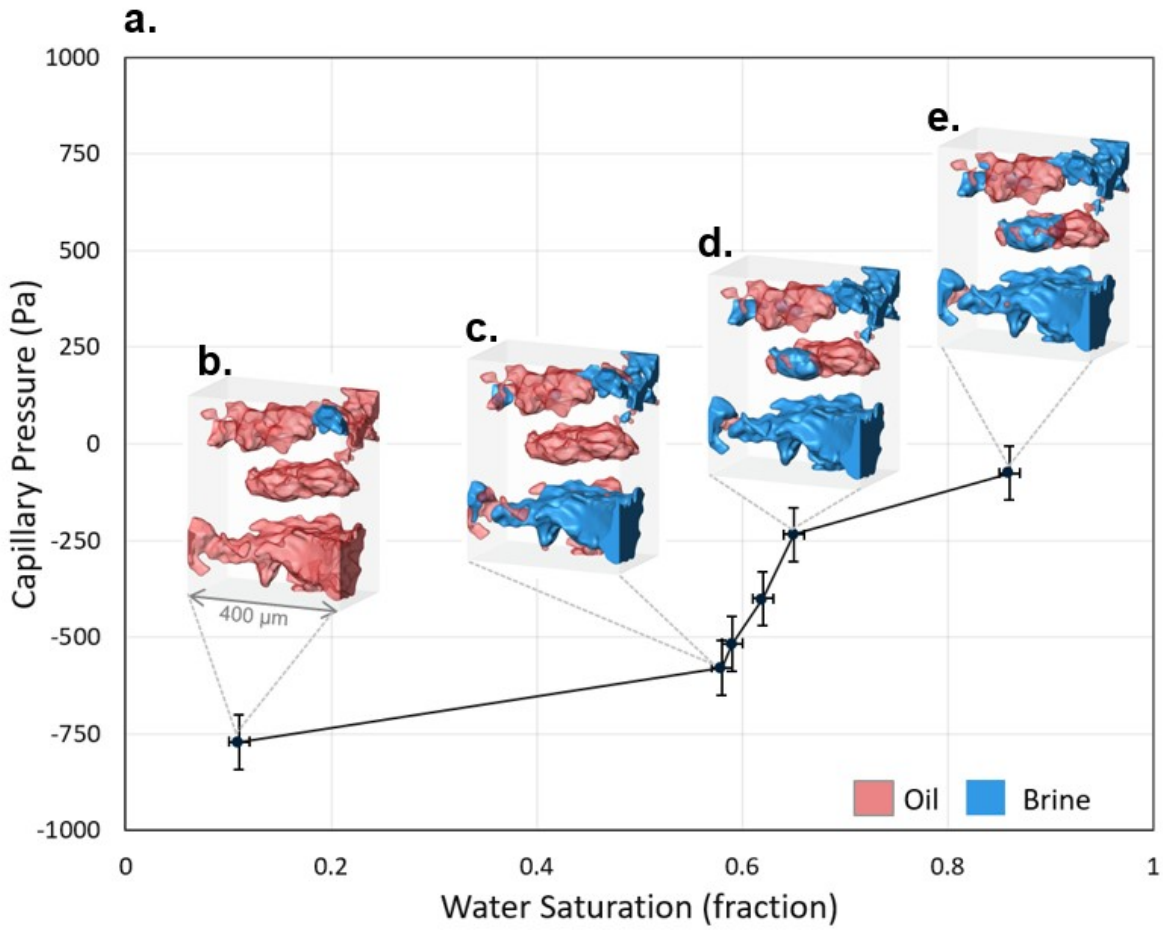

Figure 5.6: (a) The capillary pressure values estimated from the mean interfacial curvature, Figure 5.5e, as a function of water (brine) saturation. (b-e) A 3D representation of pore filling sequence during LSW where light grey, red and blue represent the rock, oil and brine phases, respectively. (b) Initially, pores were mainly filled with oil. (c) When waterflooding started, low salinity brine invaded large pores first with the lowest threshold capillary pressure. (d) and (e) Brine subsequently invaded smaller pores as more pore volumes were injected at higher flow rates.

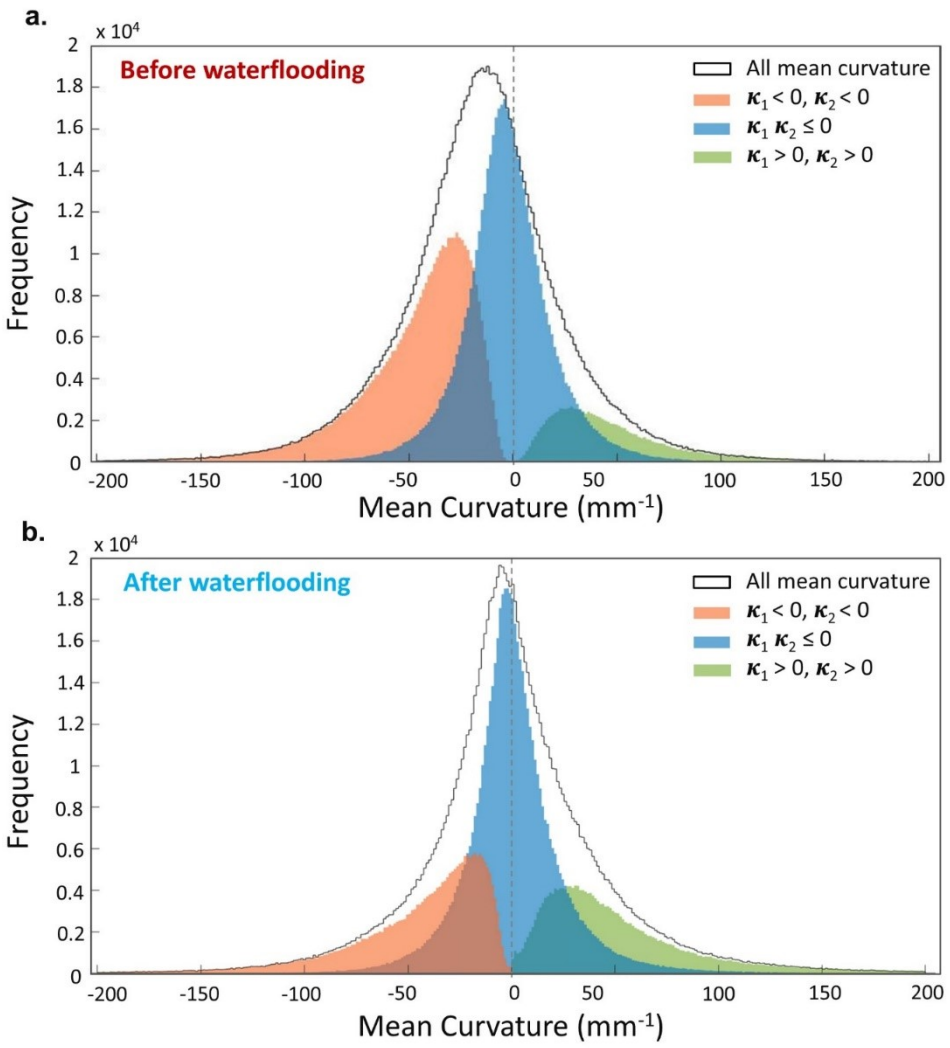

Figure 5.7: Measured oil-brine curvature distribution before and at the end of waterflooding using the principal curvatures (κ_1 and κ_2) obtained from all oil-brine interfaces. The black curve shows the mean curvatures. The distribution of values where principal curvatures are both negative, both positive and of the opposite signs are shown in orange, green and blue, respectively. After low salinity waterflooding most of the interfaces have a negative Gaussian curvature.

5.5 Summary

This experimental work offers new understanding of secondary LSW through quantifying the change in wettability caused by the low salinity effect using X-ray micro-CT imaging of an aged carbonate rock. *In situ* wettability was characterized through (i) mapping and determining the filling order of pore occupancy, (ii) measuring contact angles and curvatures, and (iii) calculating capillary pressures. The findings were also linked to fluid saturation and oil recovery.

The sample was confirmed as oil-wet after aging, shown by its high contact angle of 124° and negative mean curvature and capillary pressure values. Fluid occupancy spatial analysis revealed the impact of LSW on pore-filling events, with brine initially invading larger pores and later invading smaller pores while pushing oil into larger ones. This pattern of pore-filling and oil redistribution has not been seen before and suggests a gradual alteration in wettability by LSW. This was further supported by a shift in contact angle and mean curvature distribution towards a mean contact angle of 108° and near zero mean curvature. The capillary pressure values also indicated a shift from oil-wet to mixed-wet with a near-zero capillary pressure at final water saturation. In terms of wettability change and occupancy the behaviour is broadly similar to that observed for tertiary flooding, described in chapter 4.

Sandengen and Arntzen (2013) proposed the osmosis mechanism, a proposition endorsed by Sandengen et al. (2016), Fredriksen et al. (2016), Fredriksen et al. (2018). Contrarily, Bartels et al. demonstrated that while osmotic pressure could play a role in incremental oil recovery, it is not the primary mechanism of LSW. Derkani et al. (2018) suggested a general belief that multiple factors contribute to LSW in carbonate reservoirs. Al-Shalabi et al. (2015) noted that the enhanced oil recovery through LSW in carbonates is most effectively explained by wettability alteration induced by dissolution, alterations in pH, and expansion of the double layer.

These two experimental studies, discussed in this chapter and in chapter 4, on a quarry limestone showed that secondary LSW is more effective and yields a higher recovery factor compared to tertiary LSW. Injecting low salinity brine in secondary mode led to the recovery of 85% of the oil in the X-ray resolved pore space, while tertiary mode only recovered 66%. The reason for this difference in recovery is not due to a more limited change in wettability, as the shift in average contact angle, curvature and pore occupancy are similar in both flooding sequences. Instead, we suggest that the change in recovery is due to differences in the local sweep and flow field. In secondary mode, the low salinity water is forced to displace and contact the vast majority of the oil, leading to favourable recovery. In tertiary mode, the brine has already established flow paths through the rock, bypassing the significant amount of remaining oil after high salinity flooding. When low salinity brine is injected, it follows the same flow path, leading to limited contact with the remaining oil and substantially poorer overall recovery.

This work emphasizes the importance of beginning low salinity flooding early in the field life, rather than as a tertiary process late in the field life, at least in terms of local displacement efficiency.

The second phase in our research focused on investigating the impact of changing one or more elements of the COBR system on the low salinity effect/mechanisms. Hence, in the next chapter, a different system of crude oil, brine and reservoir rock was tested for both secondary and tertiary flooding. Here we will investigate the mechanisms of improved recovery on a more representative rock sample, as well as comparing the difference in behaviour in secondary and tertiary flooding.

Chapter 6

Pore-scale imaging of emulsification of oil during tertiary and secondary low salinity waterflooding in a reservoir carbonate

We investigated the impact of modifying the salinity and composition of injected brine on oil displacement using three-dimensional pore-scale images of the reservoir carbonate rock. High-resolution three-dimensional X-ray imaging combined with microfluidics were used to visualise the emulsification kinetics during secondary and tertiary low salinity waterflooding in a carbonate reservoir rock sample. The sample was imaged during waterflooding where the salinity of the injected brine was much lower than the formation water. The experimental protocol is described in chapter 3.

We compare the results obtained before waterflooding, and after different high salinity and low salinity waterfloods in both tertiary and secondary LSW. It is important to highlight that the HSB has a 30-

times higher salinity than LSB and a 5-times lower salinity than the formation brine. In section 6.1, we present the *in situ* emulsification of oil with the reduction of injected brine salinity in a tube. In section 6.2, we study the mechanism for oil displacement and map the emulsification process in the reservoir carbonate. In section 6.3 we study oil saturation changes, accompanied by grey level (X-ray adsorption) histograms for different waterfloods in section 6.4 showing the changes in water and oil saturations at different stages throughout the two experiments.

6.1 *In situ* emulsification of oil by diluted brine

At the start of low salinity waterflooding, an intermediate phase between the oil and brine was observed at the X-ray transparent inlet piece, shown in Figure 6.1a. We hypothesize that this phase with intermediate X-ray adsorption (greyscale) between oil and water is an emulsion. The image illustrated the development of an emulsion and water-in-oil microdroplets near the inlet (Figure 6.1b). Another image was acquired for the rock sample and again showed three phases within the pore space: oil, brine, and emulsion. Figure 6.1c shows oil in light grey in the centre of the pores whereas emulsion, in dark grey, occupying the pore corners is highlighted by the orange arrow. Water microdroplets, highlighted by the blue arrows, were also observed to grow within the oil phase.

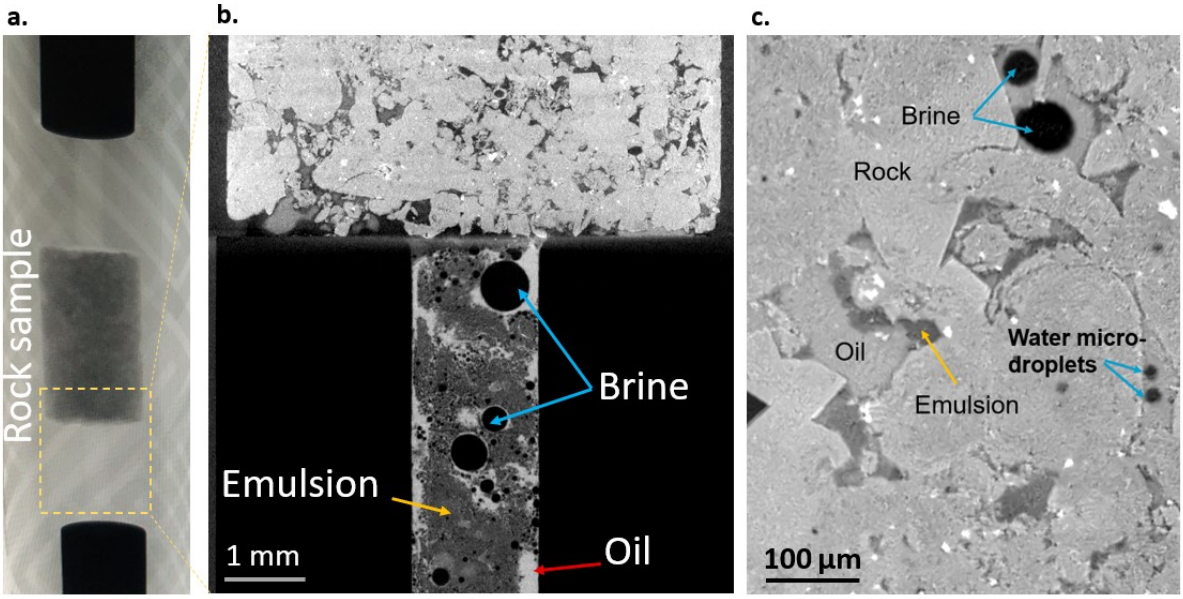

Figure 6.1: (a) the core assembly showing the rock sample in the middle and X-ray transparent end pieces at inlet and outlet. (b) Formation of emulsion during waterflooding was observed at the inlet showing water droplets of various sizes forming within the oil and the development of an intermediate greyscale emulsion phase. (c) An extracted section from the image showing the changes associated with reducing the injected brine salinity on the oil phase at the pore level.

6.2 Emulsion as a low salinity effect

The X-ray images acquired throughout the tertiary and secondary LSW experiments revealed the mechanisms by which oil was displaced during LSW adding to the analysis presented in chapters 4 and 5. To investigate these underlying mechanisms, we had a closer look at individual pores. We started with the tertiary experiments. Figure 6.2 shows the displacement processes in two pores during the injection of HSB followed by LSB in tertiary mode. From an initially oil filled pore, high salinity brine blobs started to appear at the oil rock interface after a few pore volumes were injected as shown by images acquired before and during waterflooding (Figure 6.2a-b). At the end of the first flood, after 5 pore volumes injected (PVI), the oil was still not displaced but was largely emulsified by the brine as indicated by the darkening of the oil phase (Figure 6.2c). With the injection of an additional 5 PVs of HSB and increase in flow rates from 1 to 10 µL/min, the oil phase was indistinguishable from brine suggesting the displacement of a large fraction of the oil volume initially in place (Figure 6.2d). A very small to no difference was observed when switching from HSB to LSB in this case as shown in

comparing Figure 6.2d and e. By zooming in to a smaller pore we can observe the interfaces between the different phases.

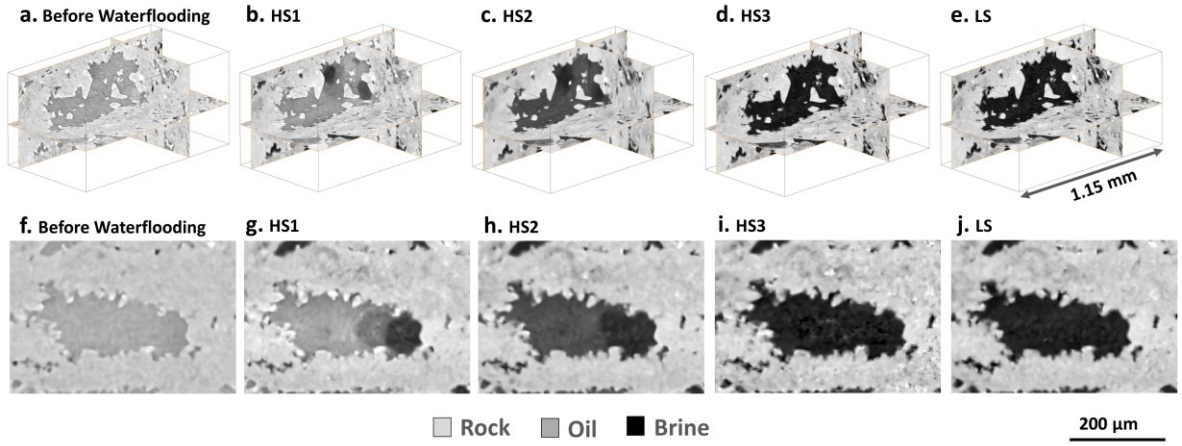

Figure 6.2: The growth of water domains at the oil/rock interface detaching the oil from the rock surface during HS waterflooding in the tertiary mode experiment as shown in (a) and (b). The oil was gradually emulsified and recovered by the continuous brine injection (c-d). By the end of HS most of the oil phase was recovered so no significant change was observed with LS injection (e). (f-j) show the same behaviour in a different pore.

Like the previous pore, Figure 6.2f shows an initially oil saturated pore. As the waterflooding begun, brine started to invade the pore developing an intermediate phase for which the greyscale values indicate to be an emulsion of oil and brine (Figure 6.2g). As more brine is injected, the volume of water in the mixture increases displacing more oil; hence the greyscale values of the emulsion phase decrease and the intermediate phase appears darker (Figure 6.2h). This trend continues with the increase in PVI of HSB and with switching to LSB, as shown in Figure 6.2i and j, respectively.

In the secondary LSW experiment, an emulsion was also observed and was seen mainly at the oil/water interface; however, the kinetics of emulsification was different compared to the tertiary mode. More displacement was observed during waterflooding in the secondary experiment compared to the tertiary experiment (compare Figure 6.2f-g and 6.3a-b), consistent with our previous results in Estaillades, chapters 4 and 5. Moreover, after the first injection rate, and 5 PVI, a substantial fraction of oil was displaced, and a smaller amount of emulsion is observed (Figure 6.3b-c). The intermediate grey-scale layer between brine (black) and oil (light grey) was observed in both experiments. The waterfront was observed to advance and connect with water microdroplets formed at or near the oil/rock interface,

highlighted by the red arrows in Figure 6.3b. After the second injection rate, and 5 additional PVI, most of the oil has been displaced (Figure 6.3d).

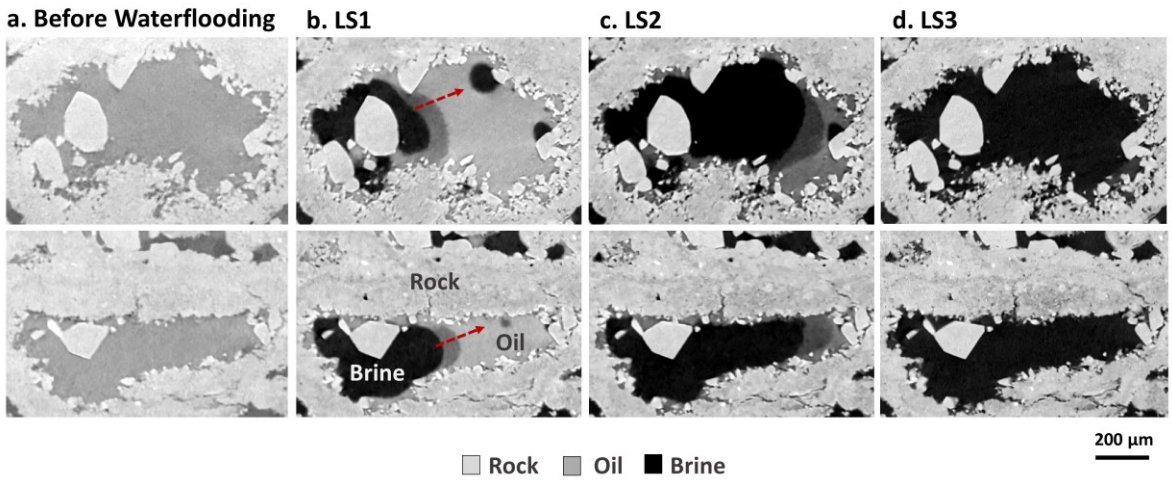

Figure 6.3: The growth of water domains at the oil/rock interface which detach the oil from the rock surface during LS waterflooding in the secondary mode experiment as shown in (a) and (b). The oil was gradually emulsified and recovered by continuous brine injection (c) and (d). The red arrows highlight the intermediate grey-level emulsion phase between oil and brine and shows how the interface connects to a micro-droplet forming near the rock surface.

There could be a link between the mechanisms of the pore-scale displacement processes and the properties of the crude oil-brine-rock (COBR) system. The asphaltene content of the crude, the salinity gradient between FB and HSB, and an even higher gradient between FB and LSB in the secondary experiment, are elements that induced the emulsification of oil and formation of water microdroplets within the oil and at the oil-brine interfaces (Emadi and Sohrabi, 2013, Chakravarty et al., 2015, Mahzari et al., 2019). In the tertiary experiment, where there was a gradual decrease in salinity from FB to HSB to LSB, the aforementioned mechanisms were observed albeit in a slower fashion (Selem et al., 2021b). Whereas in secondary mode, the mechanisms and processes were more conspicuous. This can be explained by the large osmotic gradient between the very saline water initially in place and the injected low salinity brine. Similar kinetics were also observed in our previous work, chapters 4 and 5 (Selem et al., 2021b, Selem et al., 2022). The unique observation in this chapter is however, the relatively fast emulsification of oil by reduced salinity brine resulting in the mobilization of oil by miscible displacement.

In the next section, we use the three-dimensional images to quantify the changes in oil saturation.

6.3 Changes in oil saturation

To further understand the spatial configuration of the different phases within the pore space, a three-dimensional subvolume was extracted from the full tomograms (Figure 6.4a) of the secondary LSW experiment. A pore network was extracted from the segmented image to identify individual pores (Figure 6.4b). Then average greyscale value in each pore was used to estimate the saturation. Figure 6.4c-f show the changes in oil saturation from a high oil saturation before low salinity waterflooding to a gradual decrease in oil saturation throughout the experiment, this is shown by the shift in colours from red (oil) to blue (brine). The high proportion of the intermediate green, indicating pores with a partial saturation, demonstrates emulsification prior to the eventual displacement of oil.

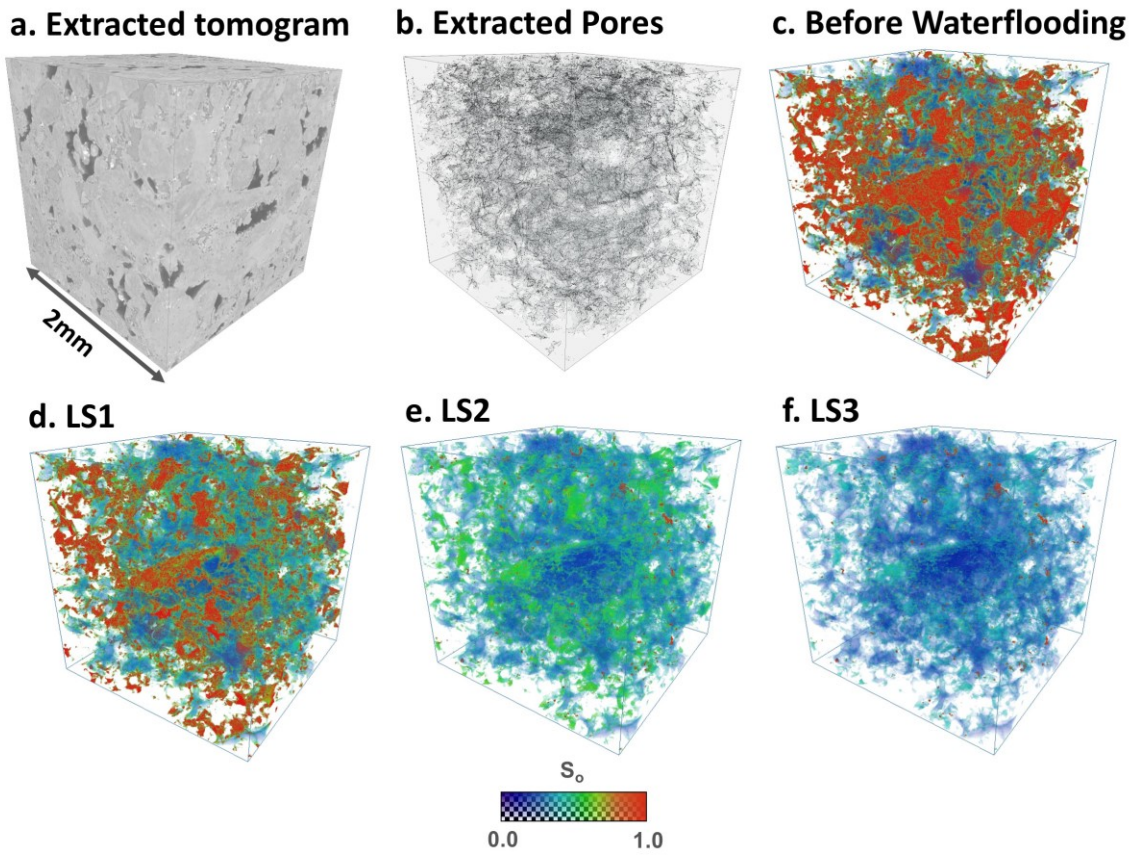

Figure 6.4: Three-dimensional visualizations showing the changes in oil saturation at different stages during secondary LSW in individual pores. The local oil saturation S_o (fraction of oil volume to the total pore volume) is determined from the greyscale averaged over every voxel within each pore which is given

colours based on the greyscale value. The shift from red to blue represents a decrease in oil saturation, and oil fraction within the emulsion phase. The difference between each LS image is nearly 1 day.

A subset of this 3D visualisation was examined to investigate the saturation changes at a pore level as shown in Figure 6.5. The intermediate emulsion phase is very clear between the oil and the brine as transition phase with a composition of roughly equal fractions of oil and water, shown by the yellow arrow in Figure 6.5a. The black arrows show oil trapped in small pores and the pore corner. After the first low salinity flood, some oil remained in the pore corners and smaller pores (Figure 6.5b). With further injection, the oil trapped in the corners and smaller pores was emulsified (Figure 6.5c) but not displaced (Figure 6.5d).

A visualization study using fast X-ray imaging for water and surfactant flooding showed similar processes and a faster displacement of oil in the latter case (Unsal et al., 2019). This was believed to be due to the higher rate of oil emulsification aided by the presence of the surfactant injected after a conventional waterflood.

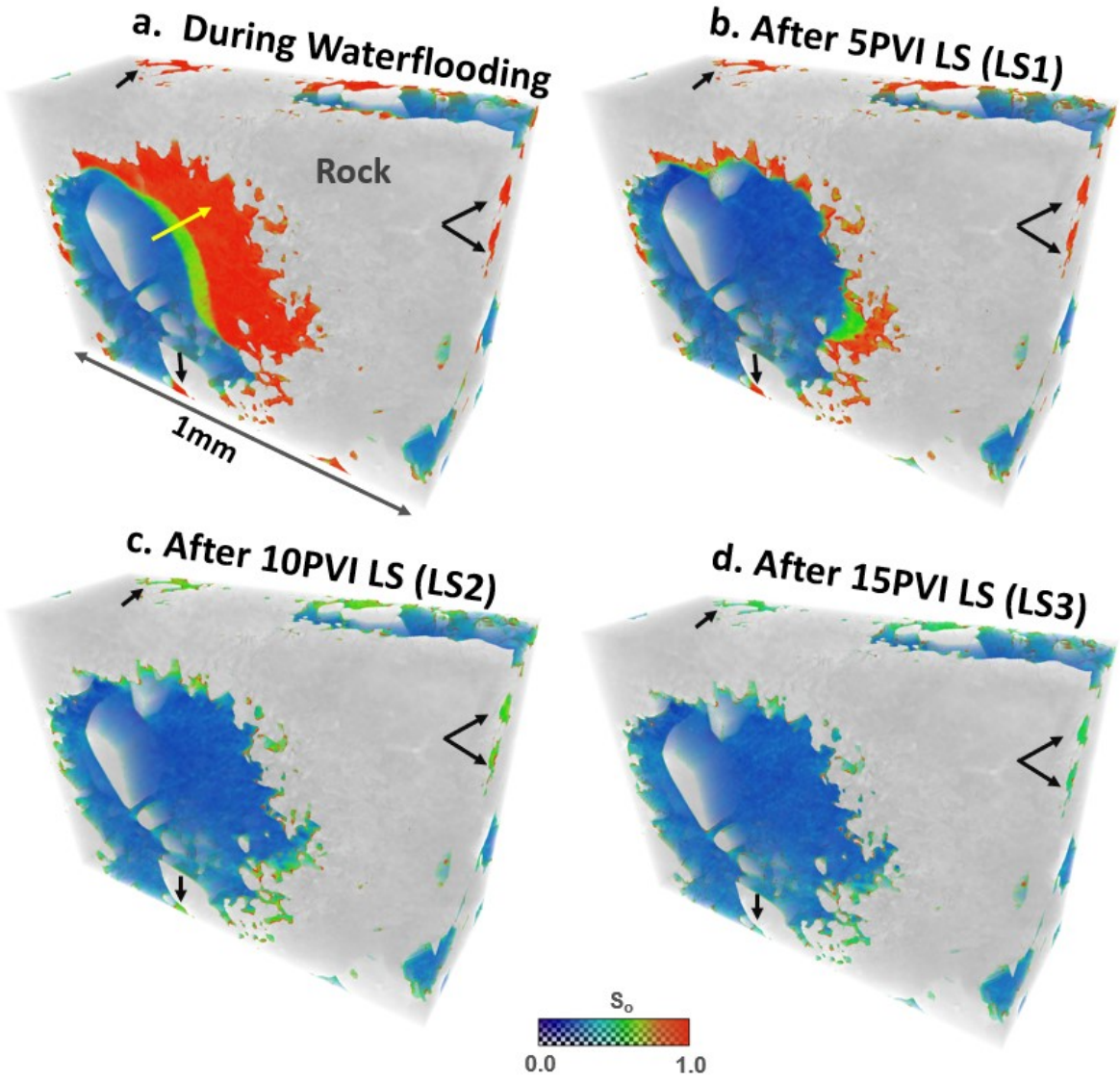

Figure 6.5: Three-dimensional visualizations of the displacement process and associated changes in oil saturation with LSW. The yellow arrow shows the waterfront with the emulsion phase between oil and water.

6.4 Grey-level histograms

The greyscale histograms for the different waterfloods during both tertiary and secondary LSW are shown in Figure 6.6. Initially the samples were predominantly saturated with oil hence the monomodal distribution: histogram shown by the red line is indicative of oil as it has a higher greyscale value than brine in both cases. The brine line histogram represents the brine predominantly saturating the rock at the end of waterflooding. In the tertiary experiment (Figure 6.6a), the histograms of the first two floods (black and green lines) show distributions with greyscale values between those of the oil (red) and brine

(blue). After the third flood, a monomodal distribution (yellow line) skewed to the left started to emerge indicating a significant decrease in oil saturation. With the switch to LSB this only signified the process (as shown by the blue line). A similar narrative applies to the secondary experiment (Figure 6.6b) apart from the fact that the histograms show a much-pronounced shift to the lower greyscale value and much bigger brine peak in the histograms (compare the black and green lines in both diagrams). With the subsequent LS floods the shift continues to the left emphasising the fast decrease in oil saturation. The intermediate grey-level histograms (black, green and yellow) indicate the slow development of emulsion for the tertiary case and a relatively fast oil emulsification, and mobilisation, of oil for the secondary waterflood.

Another study on surfactant flooding also showed a shift in greyscale histograms from bimodal, indicating separate oil and brine phases, to monomodal, indicating a single emulsion phase, with surfactant flooding (Unsal et al., 2019). However, the rate of the shift was faster than that in the case of LSW studied here.

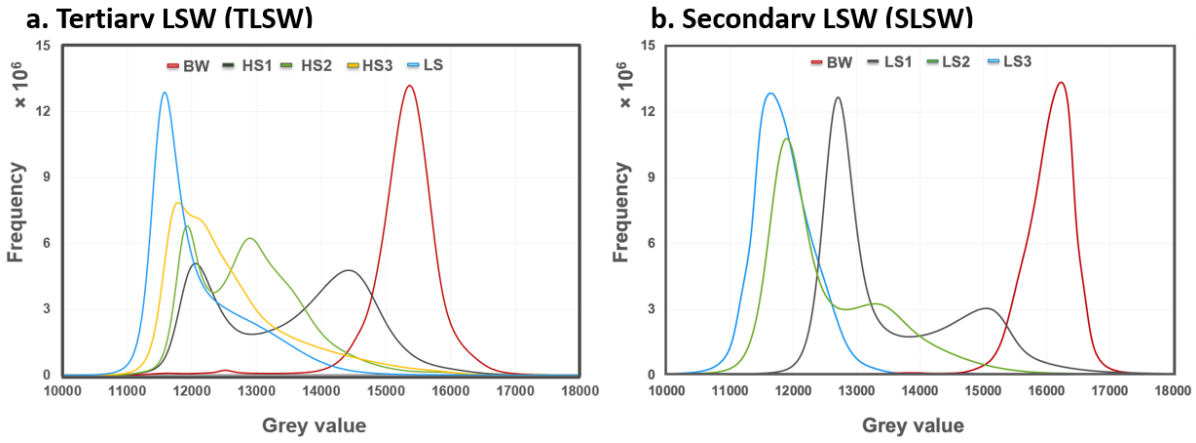

Figure 6.6: The grey level histograms of the tertiary (a) and secondary (b) low salinity waterflooding experiments at various stages. The red lines show predominantly the oil phase, with high grey-scale values, before waterflooding while blue represents the brine, after waterflooding. The transitional stages show shifting histograms from right to lift with intermediate grey-scale values between those of the oil and brine peaks. After the last flood in each experiment most of the oil was displaced as indicated by the blue lines representing the water phase with the peak at a low grey-scale value. The floods in each case indicate the three injection steps with 5 PVI at each step.

6.5 Pore occupancy

Pore occupancy analysis provides deeper insights into the sequence of displacement based on the pore size. The pore radii are mainly between 10-60 μm for both samples used in the two experiments. This is comparable to the carbonate quarry rock used in our previous work, chapter 5 (Selem et al., 2022).

The oil in the tertiary experiment is believed to be predominantly emulsified prior to displacement. After the first injection flow rate, HS1, the oil was displaced mainly from larger pores from which displacement can occur at a lower capillary pressure. However, the oil in smaller pores was emulsified, the orange lines in Figure 6.7a-c. After the second injection flow rate, the green line labelled HS2, a small fraction of oil in smaller pores was displaced by brine; the remaining oil, however, was entirely emulsified. At the end of high salinity flooding, light blue line labelled HS3, most of the emulsified oil was produced. The low salinity flood resulted in an incremental recovery: compare the light and dark blue lines in Figure 6.7b-c.

In the secondary mode, brine invaded the larger pores in the first low salinity flood, orange line labelled LS1, leaving emulsion and oil in the medium and small pores, respectively (Figure 6.7d-f). The reservoir carbonate sample is initially oil-wet and so brine, the non-wetting phase, preferentially displaces oil in the larger pores. Low salinity brine progressively invaded smaller pores in the subsequent floods, green and blue lines, with a small amount of emulsion trapped in small pores. Two main differences between the two modes are observed; (1) secondary mode results in an overall faster recovery compared to tertiary mode, and (2) the low salinity brine is more efficient than the high salinity brine, comparing the light blue lines in Figure 6.7b and e, and Figure 6.7c and f. The same number of pore volumes injected results in a better displacement with LS compared to HS. This could also be explained by the reduced mobility of the emulsified oil compared to the non-emulsified oil due to differences in viscosity (Alzahid et al., 2019, Unsal et al., 2019).

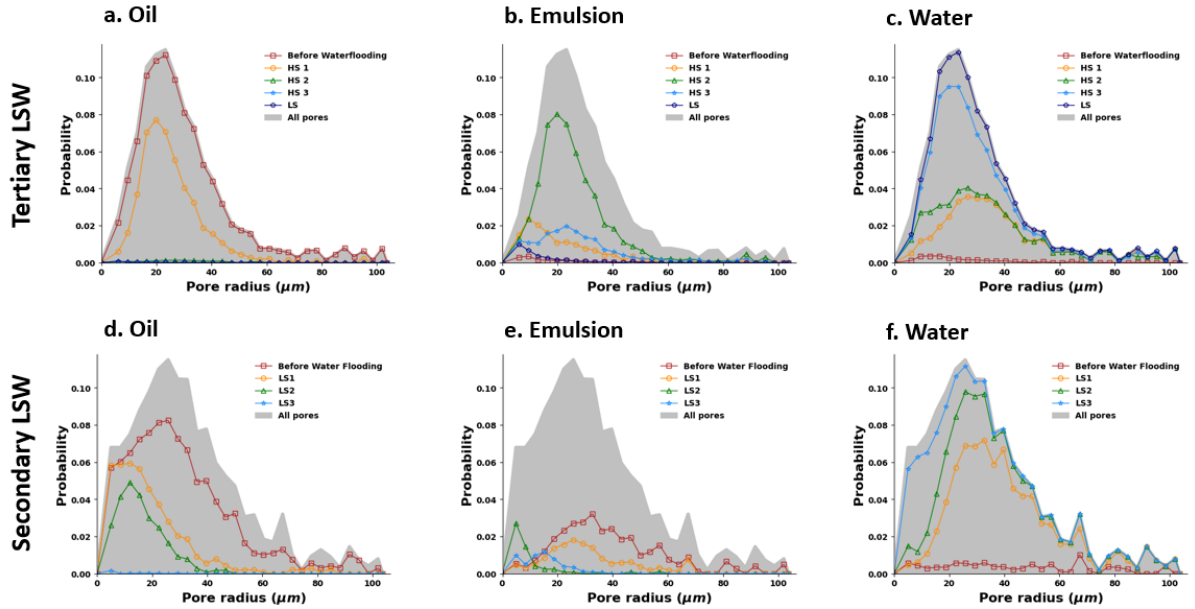

Figure 6.7: Histograms plots highlighting the distribution of pore sizes filled by oil, emulsion, and water in tertiary (a-c) and secondary (d-f) low salinity waterflooding experiment computed using generalized pore network extraction tool at different stages of waterflooding.

6.6 Summary

This work used X-ray imaging to visualise the *in situ* development of emulsion during LSW and characterized the associated changes in phase distribution as well as the impact on oil saturation. We studied secondary and tertiary LSW in a carbonate reservoir rock sample. We presented novel observations of the formation of emulsion and the displacement of oil on a natural system under reservoir conditions. This study extends previous low salinity waterflooding experiments that have focused on sandstone rocks where it was not clear if the observed recovery mechanisms applied in carbonates (Lager et al., 2008, Austad et al., 2010, Tang and Morrow, 1999).

The X-ray images showed the displacement process by which oil was mobilized. The rate of emulsion formation and hence oil displacement was higher in secondary mode compared to tertiary LSW. The results suggest that the larger the salinity gradient between the injected brine and the brine in the system, the greater the emulsification rate. The main mechanism suggested in the literature is the osmotic pressure imbalance between the water and oil phases resulting in emulsion and water-in-oil

microdroplets formation (Duboué et al., 2019, Aldousary and Kovscek, 2019). With the rock is believed to be playing a role when the mechanisms are observed at the fluid/solid interfaces.

The pore occupancy analysis revealed distinctions in the displacement method between the two modes. During tertiary flooding, a significant portion of oil was emulsified, causing a slower displacement process due to the high viscosity of emulsified oil compared to non-emulsified oil. In contrast, the displacement process in secondary mode was more effective and oil was recovered faster.

The pore occupancy analysis highlighted the differences between the displacement mechanism in the two modes; for tertiary flooding most of oil was emulsified prior to displacement which slowed down the displacement process due to the likely high viscosity of emulsified oil compared to non-emulsified oil. In secondary mode, the displacement process was more efficient and oil recovery was quicker. This agrees with the results from previous experimental work in chapters 4 and 5 on both secondary and tertiary modes, respectively, where the displacement processes and recovery were more prominent in the secondary mode. Overall, the work demonstrates the importance of emulsification as a mechanism for improved recovery in LSW.

Den Ouden et al. (2015), Austad et al. (2012), and Al-Khafaji et al. (2017) have noted that the anticipated higher incremental oil recovery in carbonate reservoirs through the application of LSW is associated with the presence of more acidic oil, characterized by a higher concentration of carboxylates. The increased presence of carboxylates allows for greater adsorption on the carbonate rock surface, rendering the rock more oil wet. A reduction in salinity alters the polarity of the zeta potential at the fluid-rock interface, leading to a shift in wettability. Sari et al. (2017) demonstrated that the incremental oil recovery in the tertiary stage of LSW may be attributed to the transformation of the rock's wettability from strongly water-wet to intermediate.

Chapter 7

Conclusions and future work

In this chapter we will summarize the novel findings and insights of our work as well as suggest areas for future studies to further improve our understanding of controlled salinity waterflooding in carbonates.

7.1 Conclusions

This thesis presents a reliable, efficient methodology for observing and assessing low salinity waterflooding mechanisms and effects in carbonate rocks at the millimetre scale. This approach combines experimental, imaging, and analytical techniques to provide a comprehensive way of observing how the change in injected brine salinity could affect the wettability of the rock and result in improved recovery. This work has created a foundation for examining controlled salinity waterflooding at the pore level. Finally, the quantitative analysis, e.g., contact angle and pore occupancy can be utilized for validation or incorporated into simulation studies to explain and forecast the observed displacement behaviour.

The four experimental studies performed are:

1. Tertiary LSW on a quarry limestone rock.
2. Secondary LSW on a quarry limestone rock.
3. Tertiary LSW on a reservoir limestone rock using a different crude oil.
4. Secondary LSW on a reservoir limestone rock using a different crude oil.

7.1.1 Mechanisms of oil recovery by low salinity waterflooding in carbonates

The mechanisms governing recovery by low salinity waterflooding can vary significantly based on the crude oil-brine-rock (COBR) system. Therefore, there is a necessity for more precise characterization of low salinity waterflooding in reservoir rocks, spanning various crude oils and brines. This can offer insights into novel recovery mechanisms. In this project, two sets of COBR systems have been studied. Two heterogeneous carbonate rocks, two different low salinity brine recipes, and two crude oils with different properties were assessed. Our extension of this research from the first phase of experiments on quarry rocks to the second phase of experiments on reservoir rocks involved two key aspects: firstly, the examination of different recovery mechanisms; and secondly, a detailed exploration of the mechanisms observed in the first phase, along with their potential role in the recovery process.

Numerous observations and measurements pointed to alterations in wettability, shifting towards a more water-wet state following the injection of low-salinity brine. Additionally, the visualization of micro-dispersions in the pore space was evident, playing a crucial role in facilitating displacement. The findings from the experiments indicate that a higher salinity gradient between the injected brine and the existing system brine corresponds to an increased emulsification/micro-dispersion development rate. Figure 7.1 shows an example of the development and growth of water-in-oil microdroplets during tertiary LSW where the salinity gradient between the injected brine (HSB and LSB) and formation brine has a large impact on the size of the microdroplets. When the highest gradient is introduced with the injection of LSB, water droplets expand and coalesce resulting in increased oil recovery. The primary mechanism proposed in the literature involves an osmotic pressure imbalance between the water and oil phases, leading to emulsion formation and the creation of water-in-oil microdroplets. The two sets of experiments tested in this project showed variations in the nature of the displacement mechanisms from water-in-oil micro-dispersions to the complete emulsification of oil by the injections of brine with reduced salinity.

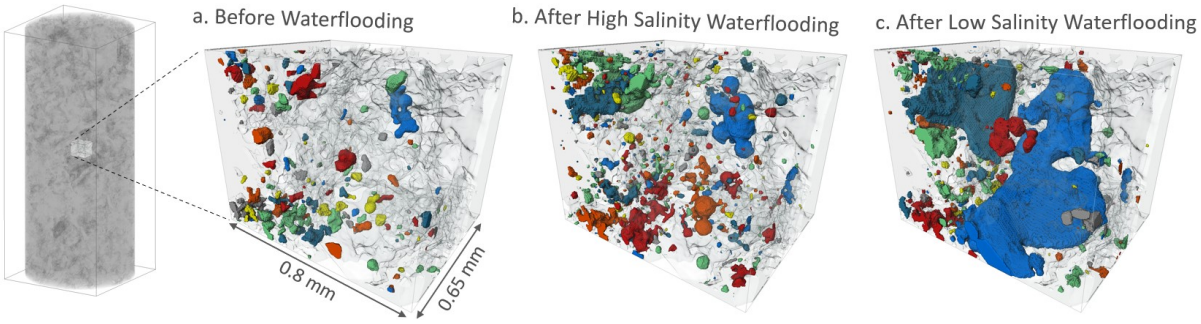

Figure 7.1: Formation of water micro-dispersion because of the low salinity effect during the tertiary LSW experiment on Estaillades carbonate. Different colours represent different connected brine blobs. Oil is transparent and rock is semi-transparent.

The next two sections highlight those variations and also shed light on the difference between secondary and tertiary flooding modes.

7.1.2 Tertiary and secondary LSW on a quarry carbonate

Firstly, in the tertiary LSW on Estaillades study presented in Chapter 4, we used X-ray imaging to observe the *in situ* development of low salinity mechanisms on a natural system and characterized the associated changes in rock wettability as well as the impact on oil recovery.

For our combination of crude oil, brine and rock, a response to LSW was demonstrated. The distribution of the oil phase, before and during the HS floods, in dead-end regions of the pore space and expanding along the pore walls is indicative of the relatively strong propensity of the rock surface to oil, consistent with the measured high contact angle and negative capillary pressure values. After LSW, the development of water micro-droplets at the oil/brine and oil/rock interfaces and in the oil phase, as well as the expansion of thin water films between the oil and rock surface were observed. Water film swelling and micro-dispersions are considered the underlying mechanisms for the wettability alteration and ultimately the low salinity effect observed in this study. This is in line with observations from previous studies on the relationship between water-in-oil micro-dispersions and crude oil properties (Emadi and Sohrabi, 2013, Mahzari and Sohrabi, 2014, Mahzari et al., 2018). The formation of micro-dispersions, driven by diffusion and osmosis, resulted in oil displacement and mobilization (Sandengen et al., 2016, Fredriksen et al., 2018).

Unlike in previous work (Emadi and Sohrabi, 2013), our results show a gradual formation of water micro-dispersions during HSW, which is due to the salinity difference between FB, or irreducible water, and HSB until osmotic equilibrium is reached. It was also observed that, after switching to LSW, oil in the pores in which micro-droplets had formed during HSW, was recovered faster than in the pores that remained intact after HSW. The fast coalescence of water micro-droplets during LSW is driven by the significant differences in salinity, and ionic strength, between the LSB and the brine in the system. This explains the inability to capture the development of water micro-droplets during secondary LSW (Selem et al., 2021b).

Analyses of contact angles, curvatures, capillary pressures, and pore occupancy indicated a shift in the rock wettability from oil-wet towards mixed-wet conditions due to LSW. The change in wettability induced by LSW improved the microscopic sweep efficiency as the result of increased capillary forces (Selem et al., 2021b). The underlying mechanisms and subsequent change in wettability resulted in a 9% increase in oil recovery. A similar increase in recovery was obtained in a previous tertiary LSW coreflooding experiment (Piñerez Torrijos et al., 2016).

The ultimate oil recovery using HSB was 57% of OOIP. After the first flood of LSB, 10 PVs injected at 0.001 mL/min, the recovery increased to 60% of OOIP, and by the end of LSW, the recovery reached 66% of OOIP. The LSE has resulted in a 9% incremental oil recovery. The gradual increase in oil recovery during LSW is due to the rearrangement of oil in the pore space before it was eventually displaced, i.e. the low salinity effect was not instant. Prior to the eventual displacement of the oil layers, two phenomena were observed: the formation of water micro-droplets within the oil phase and at the oil/solid interface, and then the expansion of the thin water films.

We suggest that the observed mechanisms resulted in the release of oil which was then reconnected with oil from other surrounding pores. Moreover, the possible formation of water micro-dispersions in oil caused oil-swelling. The swelling and reconnection of oil ganglion enhanced the oil mobility and efficiently reduced the remaining oil saturation.

This comprehensive LSW study provides insights into the pore-scale displacement mechanisms previously observed only on micro-models (Emadi and Sohrabi, 2013, Sohrabi et al., 2017, Fredriksen et al., 2018). These results can help interpret the outcome from Darcy and molecular scale experiments, hence bridging the gap between these very different length scales. Moreover, this study can deliver valuable input for the brine selection criteria to design LSW-EOR. Finally, the quantitative experimental measurements presented can be used for pore-scale modelling validation and upscaling in enhanced oil recovery projects.

The second experimental study, secondary LSW on Estaillades, presented in chapter 5 provides novel insights into secondary LSW through quantitative characterization of wettability alteration associated with the low salinity effect using X-ray micro-CT images of coreflooding of an aged carbonate rock at subsurface conditions. While the experiment was conducted on only a single sample, we suggest that the findings are applicable to LSW in most carbonate rocks, this is also proved by the results from the previous experiment. *In situ* wettability was characterized by contact angle and curvature measurements, capillary pressure calculations, and pore occupancy mapping and filling order.

The findings were evidenced by considering contact lines, fluid saturation and oil recovery measurements. The oil-wet nature of the sample, after ageing, was confirmed by the high contact angle, as well as the negative mean curvature and capillary pressure values. Spatial analysis of fluid occupancy showed the effects of LSW on pore-filling events.

After the injection of 60 pore volumes at different flow rates, a prolonged response to low salinity injection is observed in this study. The changes in the wettability configuration in the system and the good connectivity of the oil phase were the main factors responsible for a remarkable recovery performance and a low residual oil saturation, 15%, in the resolved porosity.

The results from these two experimental studies showed consistency with regards to a response to diluting the injected brine salinity. However, when compared to tertiary LSW, secondary LSW is more efficient and achieved a higher recovery factor. When injecting LSB in secondary mode 85% of the oil,

in the pore space resolved by X-ray imaging, was recovered compared to 66% in tertiary mode (Figure 7.1).

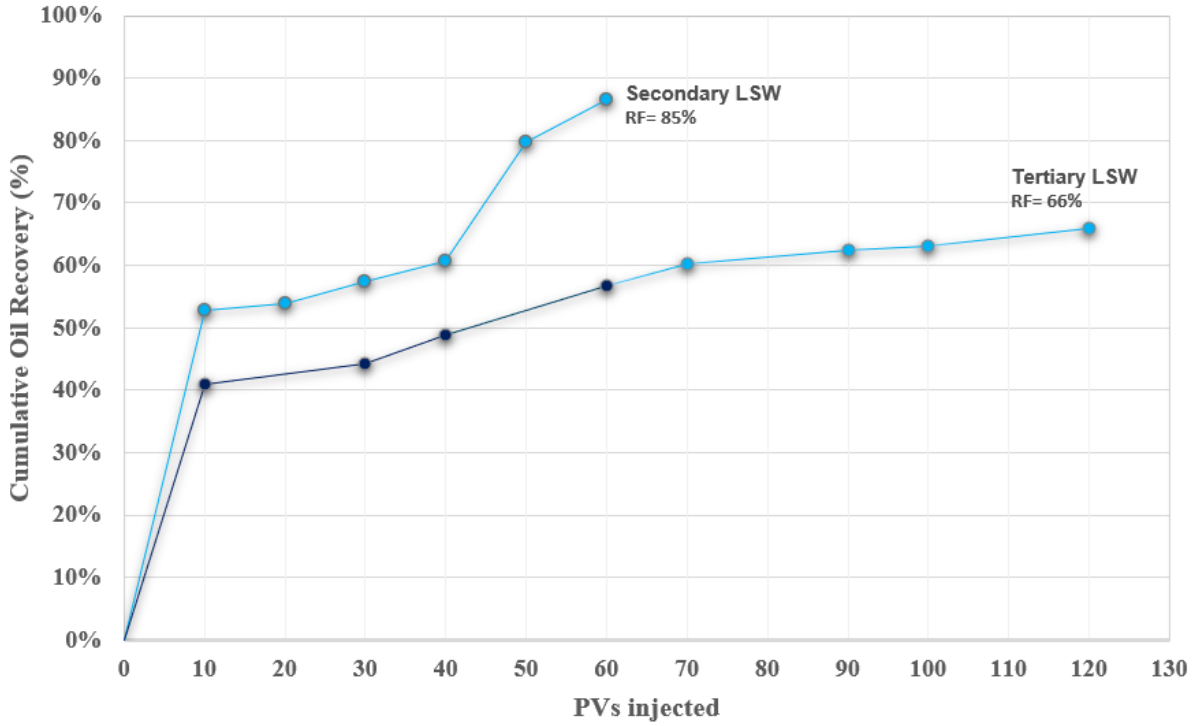

Figure 7.2: LSW contributed to better oil recovery in secondary mode compared to that in tertiary mode.

In tertiary mode, the local displacement efficiency is lower, as the brine continues to follow principally the flow pathways established during the initial, inefficient, high salinity flood. Moreover, the rate of micro-dispersions formation during secondary LSW was faster, compared to tertiary LSW, which enhanced oil mobilization and displacement (Figures 7.2 and 7.3).

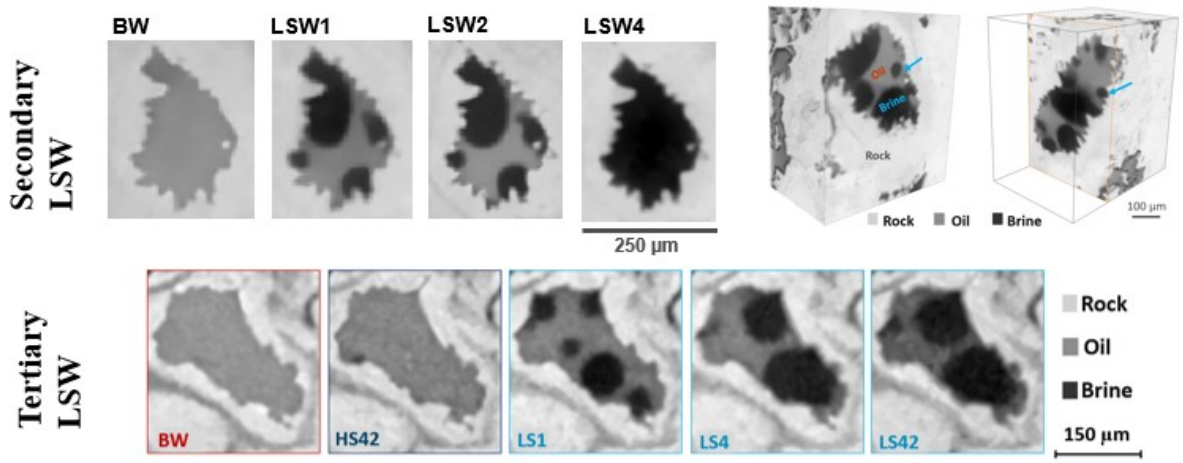

Figure 7.3: Similar oil displacement processes by LS brine were observed in both secondary and tertiary floods. Oil displacement was faster in the secondary mode compared to tertiary.

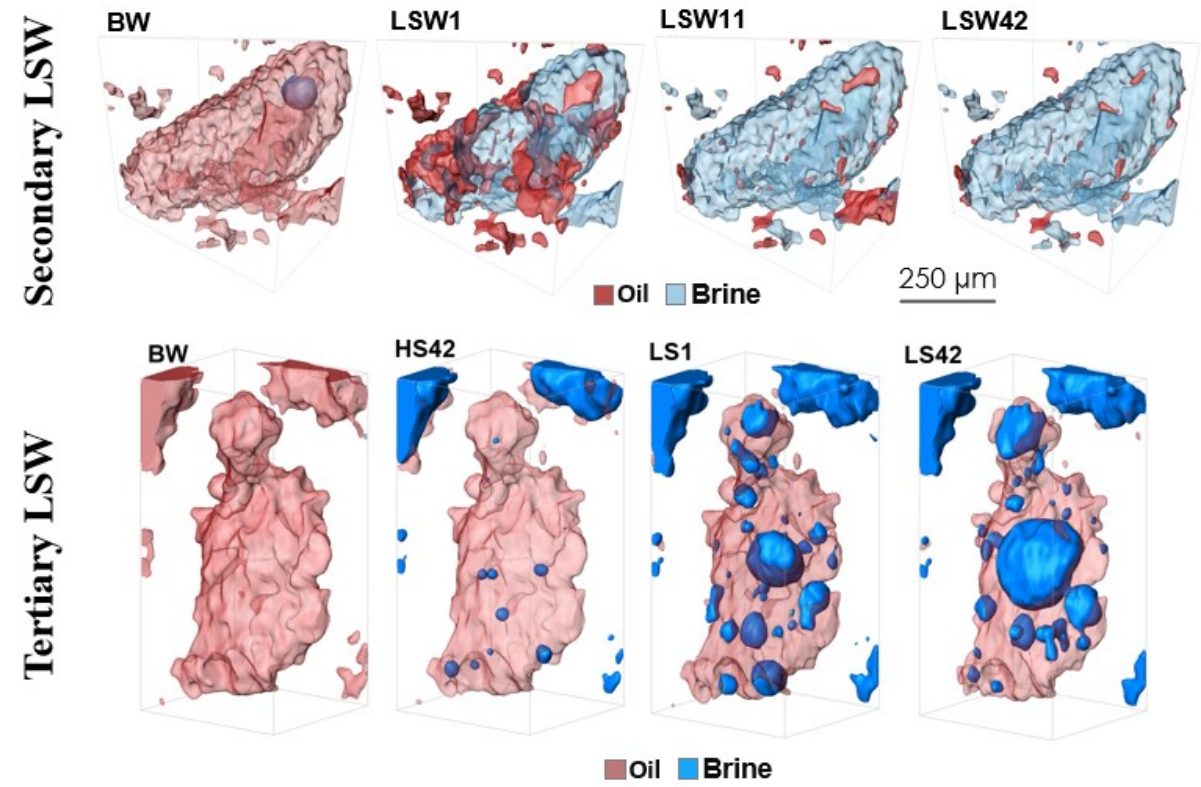

Figure 7.4: The faster and more efficient of recovery of oil in secondary mode (top) compared to the slow development and displacement of oil in tertiary mode (bottom).

This work provides hitherto unreported insights into pore-scale displacements under LSW and can help interpret results obtained from core-scale experiments. The results offer a valuable benchmark for pore-scale modelling and upscaling to help design LSW EOR projects at the field scale. Further work could

compare the pore-scale displacement observed here with the results from a tertiary LSW. Moreover, the same methodology for wettability characterisation on a pore-by-pore basis can be applied to study displacement in oil- and mixed-wet porous media in other applications, such as carbon storage, flow in batteries and packed bed chemical reactors.

7.1.3 Tertiary and secondary LSW on a reservoir carbonate

In the final set of experiments, we presented novel observations of the formation of emulsion and the displacement of oil on a natural system under reservoir conditions. The X-ray images showed the displacement process by which oil was mobilized. The rate of emulsion formation and hence oil displacement was higher in secondary mode compared to tertiary LSW. The results suggest that the larger the salinity gradient between the injected brine and the brine in the system, the greater the emulsification rate. The main mechanism suggested in the literature is the osmotic pressure imbalance between the water and oil phases resulting in the formation of an emulsion and water-in-oil microdroplets (Duboué et al., 2019, Aldousary and Kovscek, 2019).

In the Estaillades experiments, the intermediate phase of emulsion was also observed. Figure 7.4 shows an example of the changes in a pore during secondary LSW experiment on Estaillades. The emulsion phase was observed near the interface between oil and rock (Figure 7.4b).

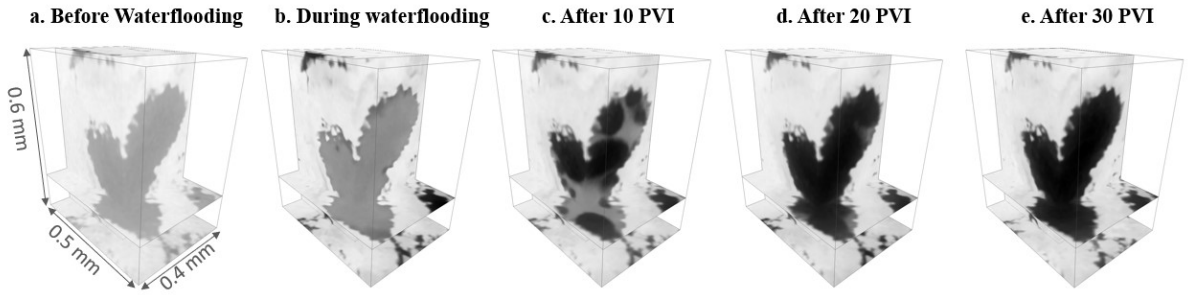

Figure 7.5: A visualization of the changes during secondary LSW in the Estaillades experiment.

The pore occupancy analysis highlighted the differences between the displacement mechanism in the two modes; for tertiary flooding most of oil was emulsified prior to displacement which slowed down the displacement process due to the likely high viscosity of emulsified oil compared to non-emulsified oil. In secondary mode, the displacement process was more efficient and oil recovery was quicker. This is consistent with all the work in this thesis on both secondary and tertiary modes where the displacement processes and recovery were more prominent in the secondary mode. Overall, the work demonstrates the importance of emulsification as a mechanism for improved recovery in LSW (AlHammadi et al., 2018b, Fattahi Mehraban et al., 2020, Fattahi Mehraban et al., 2021).

7.2 Future Work

This thesis covers a broad scope of LSW mechanisms and processes, two COBR systems were assessed and similar mechanisms of oil displacement were highlighted. This increases the predictability of which crude oil and rock systems will respond to low salinity waterflooding, but further research is necessary to improve the systems predictability. Micro-scale X-ray imaging is a promising approach to gain comprehensive understanding of this and other EOR techniques, as demonstrated in this work. The suggestions for future work are as follows:

1. Future work could expand on our findings in chapter 4 with regards to the water film expansion. More measurements are needed to better understand the different metrics, e.g., brine salinity, composition, temperature, and oil properties, affecting the double layer expansion mechanism

of LSW. Measurement of the film thickness could also be valuable as no such measurement was done on carbonates.

2. Future work could also focus on understanding the dynamics of LSW mechanisms such as the timescale of water micro-dispersions growth and thin water films development. This could dramatically help further understand the time response of LSW.
3. Another recommendation is to perform steady state LSW experiments and measure relative permeability to further understand the relationship between the observed mechanisms and displacement processes.
4. Studying LSW can be combined with CO_2 injection to combine EOR with CCS.
5. This thesis did not consider the impact of micro- or sub-resolution porosity on fluid flow, as three-phase flow segmentation would have been more challenging. However, micro-porosity is crucial in facilitating the flow of water, especially at lower saturation levels. To fully account for its contribution in the future, a more advanced segmentation method is needed.
6. Additionally, the *in situ* measured geometric contact angle was calculated as the average of a wide, varied distribution in individual pores due to rough surfaces and intricate pore shapes. This method can provide a general idea of surface wettability, but it is not accurate for displacement angles, which are essential for pore-scale modelling. The thermodynamic contact angle, which is obtained from an energy balance, provides more reliable estimates of displacement angles as it relies on less sensitive parameters, such as local volume change, interfacial curvature, and area, rather than a fixed three-phase contact line (Blunt et al., 2019).
7. Furthermore, with pore-scale imaging, the movement and impact of surfactants and foams can be studied.

These experiments, combined with the findings from this thesis and previous research, could serve as the basis for pore-scale modelling and simulation of LSW EOR in the field. While the experimental methodologies and image analysis techniques developed were strictly applied to investigate LSW in permeable rocks, it can in fact be used as a standard procedure to study multiphase flow in a broad range of porous media. More specifically, the techniques could be adapted for various applications, other than

enhanced oil recovery, including the design of microfluidic devices, batteries, fuel cells as well as contaminant transport in soils.

References

ABDALLAH, W., BUCKLEY, J. S., CARNEGIE, A., EDWARDS, J., HEROLD, B., FORDHAM, E., GRAUE, A., HABASHY, T., SELEZNEV, N. & SIGNER, C. 1986. Fundamentals of wettability. *Technology,* 38**,** 268.

ABDOLMOHSEN, S.-A., ABDALLA, A. M., MOHD, S. I. & JOSE, V. P. P. 2015. Experimental investigation into effects of crude oil acid and base number on wettability alteration by using different low salinity water in sandstone rock. *Journal of the Japan Petroleum Institute,* 58**,** 228-236.

ABRAMS, D. S. & PRAUSNITZ, J. M. 1975. Statistical thermodynamics of liquid mixtures: a new expression for the excess Gibbs energy of partly or completely miscible systems. *AIChE journal,* 21**,** 116-128.

AKBAR, M., VISSAPRAGADA, B., ALGHAMDI, A. H., ALLEN, D., HERRON, M., CARNEGIE, A., DUTTA, D., OLESEN, J.-R., CHOURASIYA, R. & LOGAN, D. 2000. A snapshot of carbonate reservoir evaluation. *Oilfield Review,* 12**,** 20-21.

AL-ATTAR, H. H., MAHMOUD, M. Y., ZEKRI, A. Y., ALMEHAIDEB, R. & GHANNAM, M. 2013. Low-salinity flooding in a selected carbonate reservoir: experimental approach. *Journal of Petroleum Exploration and Production Technology,* 3**,** 139-149.

AL-KHAFAJI, A., NEVILLE, A., WILSON, M. & WEN, D. 2017. Effect of low salinity on the oil desorption efficiency from calcite and silica surfaces. *Energy & Fuels,* 31**,** 11892-11901.

AL-SHALABI, E. W., SEPEHRNOORI, K. & POPE, G. 2015. Geochemical interpretation of low-salinity-water injection in carbonate oil reservoirs. *Spe Journal,* 20**,** 1212-1226.

ALDOUSARY, S. & KOVSCEK, A. R. 2019. The diffusion of water through oil contributes to spontaneous emulsification during low salinity waterflooding. *Journal of Petroleum Science and Engineering,* 179**,** 606-614.

ALHAMMADI, A. M., ALRATROUT, A., BIJELJIC, B. & BLUNT, M. J. 2018a. Pore-scale imaging and characterization of hydrocarbon reservoir rock wettability at subsurface conditions using X-ray microtomography. *Journal of visualized experiments: JoVE*.

ALHAMMADI, A. M., ALRATROUT, A., SINGH, K., BIJELJIC, B. & BLUNT, M. J. 2017. In situ characterization of mixed-wettability in a reservoir rock at subsurface conditions. *Scientific Reports,* 7**,** 10753.

ALHAMMADI, A. M., GAO, Y., AKAI, T., BLUNT, M. J. & BIJELJIC, B. 2020. Pore-scale X-ray imaging with measurement of relative permeability, capillary pressure and oil recovery in a mixed-wet micro-porous carbonate reservoir rock. *Fuel,* 268**,** 117018.

ALHAMMADI, M., MAHZARI, P. & SOHRABI, M. 2018b. Fundamental investigation of underlying mechanisms behind improved oil recovery by low salinity water injection in carbonate rocks. *Fuel,* 220**,** 345-357.

ALHOSANI, A., SCANZIANI, A., LIN, Q., RAEINI, A. Q., BIJELJIC, B. & BLUNT, M. J. 2020a. Pore-scale mechanisms of CO2 storage in oilfields. *Scientific Reports,* 10**,** 8534.

ALHOSANI, A., SCANZIANI, A., LIN, Q., SELEM, A., PAN, Z., BLUNT, M. J. & BIJELJIC, B. 2020b. Three-phase flow displacement dynamics and Haines jumps in a hydrophobic porous medium. *Proceedings of the Royal Society A: Mathematical, Physical and Engineering Sciences,* 476**,** 20200671.

ALQURAISHI, A. A., AMAO, A. M., AL-ZAHRANI, N. I., ALQARNI, M. T. & ALSHAMRANI, S. A. 2019. Low salinity water and CO2 miscible flooding in Berea and Bentheimer sandstones. *Journal of King Saud University - Engineering Sciences,* 31**,** 286-295.

ALRATROUT, A., BLUNT, M. J. & BIJELJIC, B. 2018. Wettability in complex porous materials, the mixed-wet state, and its relationship to surface roughness. *Proceedings of the National Academy of Sciences,* 115**,** 8901-8906.

ALRATROUT, A., RAEINI, A. Q., BIJELJIC, B. & BLUNT, M. J. 2017. Automatic measurement of contact angle in pore-space images. *Advances in Water Resources,* 109**,** 158-169.

ALVARADO, V., BIDHENDI, M. M., GARCIA-OLVERA, G., MORIN, B. & OAKEY, J. S. Interfacial Visco-Elasticity of Crude Oil - Brine: An Alternative EOR Mechanism in Smart Waterflooding. SPE Improved Oil Recovery Symposium, 2014. SPE-169127-MS.

ALYAFEI, N. & BLUNT, M. J. 2016. The effect of wettability on capillary trapping in carbonates. *Advances in Water Resources,* 90**,** 36-50.

ALZAHID, Y. A., MOSTAGHIMI, P., ALQAHTANI, N. J., SUN, C., LU, X. & ARMSTRONG, R. T. 2019. Oil mobilization and solubilization in porous media by in situ emulsification. *Journal of Colloid and Interface Science,* 554**,** 554-564.

ANDERSON, W. 1986. Wettability Literature Survey- Part 2: Wettability Measurement. *Journal of Petroleum Technology,* 38**,** 1246-1262.

ANDREW, M., BIJELJIC, B. & BLUNT, M. J. 2013. Pore-scale imaging of geological carbon dioxide storage under in situ conditions. *Geophysical Research Letters,* 40**,** 3915-3918.

ANDREW, M., BIJELJIC, B. & BLUNT, M. J. 2014a. Pore-scale contact angle measurements at reservoir conditions using X-ray microtomography. *Advances in Water Resources,* 68**,** 24-31.

ANDREW, M., BIJELJIC, B. & BLUNT, M. J. 2014b. Pore-scale imaging of trapped supercritical carbon dioxide in sandstones and carbonates. *International Journal of Greenhouse Gas Control,* 22**,** 1-14.

ANDREW, M., MENKE, H., BLUNT, M. J. & BIJELJIC, B. 2015. The Imaging of Dynamic Multiphase Fluid Flow Using Synchrotron-Based X-ray Microtomography at Reservoir Conditions. 110**,** 1-24.

ANDREWS, E., MUGGERIDGE, A., GARFI, G., JONES, A. & KREVOR, S. 2021. Pore-Scale X-ray Imaging of Wetting Alteration and Oil Redistribution during Low-Salinity Flooding of Berea Sandstone. *Energy & Fuels,* 35**,** 1197-1207.

ANDREWS, E., MUGGERIDGE, A., JONES, A. & KREVOR, S. 2023. Pore structure and wetting alteration combine to produce the low salinity effect on oil production. *Fuel,* 332**,** 126155.

ARMSTRONG, R. T., PORTER, M. L. & WILDENSCHILD, D. 2012. Linking pore-scale interfacial curvature to column-scale capillary pressure. *Advances in Water Resources,* 46**,** 55-62.

ARNS, C. H., BAUGET, F., LIMAYE, A., SAKELLARIOU, A., SENDEN, T., SHEPPARD, A., SOK, R. M., PINCZEWSKI, V., BAKKE, S., BERGE, L. I., OREN, P. E. & KNACKSTEDT, M. A. 2005. Pore Scale Characterization of Carbonates Using X-Ray Microtomography. *SPE Journal,* 10**,** 475-484.

AUSTAD, T., REZAEIDOUST, A. & PUNTERVOLD, T. Chemical Mechanism of Low Salinity Water Flooding in Sandstone Reservoirs. SPE Improved Oil Recovery Symposium, 2010. SPE-129767-MS.

AUSTAD, T., SHARIATPANAHI, S. F., STRAND, S., AKSULU, H. & PUNTERVOLD, T. 2015. Low Salinity EOR Effects in Limestone Reservoir Cores Containing Anhydrite: A Discussion of the Chemical Mechanism. *Energy & Fuels,* 29**,** 6903-6911.

AUSTAD, T., SHARIATPANAHI, S. F., STRAND, S., BLACK, C. J. J. & WEBB, K. J. 2012. Conditions for a Low-Salinity Enhanced Oil Recovery (EOR) Effect in Carbonate Oil Reservoirs. *Energy & Fuels,* 26**,** 569-575.

BARTELS, W.-B.-B., MAHANI, H., BERG, S., MENEZES, R., VAN DER HOEVEN, J. A. & FADILI, A. 2017a. Oil Configuration Under High-Salinity and Low-Salinity Conditions at Pore Scale: A Parametric Investigation by Use of a Single-Channel Micromodel. *SPE Journal,* 22**,** 1362-1373.

BARTELS, W.-B., RÜCKER, M., BERG, S., MAHANI, H., GEORGIADIS, A., FADILI, A., BRUSSEE, N., COORN, A., VAN DER LINDE, H., HINZ, C., JACOB, A., WAGNER, C., HENKEL, S., ENZMANN, F., BONNIN, A., STAMPANONI, M., OTT, H., BLUNT, M. & HASSANIZADEH, S. M. 2017b. Fast X-Ray Micro-CT Study of the Impact of Brine Salinity on the Pore-Scale Fluid Distribution During Waterflooding. *Petrophysics - The SPWLA Journal of Formation Evaluation and Reservoir Description,* 58**,** 36-47.

BARTELS, W., RÜCKER, M., BERG, S., MAHANI, H., GEORGIADIS, A., BRUSSEE, N., COORN, A., VAN DER LINDE, H., FADILI, A. & HINZ, C. 2016. Micro-ct study of the impact of low salinity waterflooding on the pore-scale fluid distribution during flow. *International symposium of the society of core analysts, Snowmass, CO,* 22**,** 1362-1373.

BARTELS, W. B., MAHANI, H., BERG, S. & HASSANIZADEH, S. M. 2019. Literature review of low salinity waterflooding from a length and time scale perspective. *Fuel,* 236**,** 338-353.
BERGER, M. & GOSTIAUX, B. 2012. *Differential Geometry: Manifolds, Curves, and Surfaces: Manifolds, Curves, and Surfaces*, Springer Science & Business Media.
BIJELJIC, B., MOSTAGHIMI, P. & BLUNT, M. J. 2013. Insights into non-Fickian solute transport in carbonates. *Water Resources Research,* 49**,** 2714-2728.
BIN SELAMAT, S., TELETZKE, G., DINESH PATEL, P., B. DARMAN, N. & AZURA SHUHAIMI, M. 2008. EOR : The New Frontier in the Malay Basin Development. *International Petroleum Technology Conference, IPTC 2008,* 4.
BLUNT, M. J. 1997. Pore level modeling of the effects of wettability. *Spe Journal,* 2**,** 494-510.
BLUNT, M. J. 2017. *Multiphase flow in permeable media: A pore-scale perspective*, Cambridge University Press.
BLUNT, M. J., BIJELJIC, B., DONG, H., GHARBI, O., IGLAUER, S., MOSTAGHIMI, P., PALUSZNY, A. & PENTLAND, C. 2013. Pore-scale imaging and modelling. *Advances in Water Resources,* 51**,** 197-216.
BLUNT, M. J., LIN, Q., AKAI, T. & BIJELJIC, B. 2019. A thermodynamically consistent characterization of wettability in porous media using high-resolution imaging. *Journal of Colloid and Interface Science,* 552**,** 59-65.
BUADES, A., COLL, B. & MOREL, J. 2005. A non-local algorithm for image denoising. *2005 IEEE Computer Society Conference on Computer Vision and Pattern Recognition (CVPR'05),* 2**,** 60-65 vol. 2.
BUCKLEY, J. S., LIU, Y. & MONSTERLEET, S. 1998. Mechanisms of Wetting Alteration by Crude Oils. *SPE Journal,* 3**,** 54-61.
BUI, M., ADJIMAN, C. S., BARDOW, A., ANTHONY, E. J., BOSTON, A., BROWN, S., FENNELL, P. S., FUSS, S., GALINDO, A., HACKETT, L. A., HALLETT, J. P., HERZOG, H. J., JACKSON, G., KEMPER, J., KREVOR, S., MAITLAND, G. C., MATUSZEWSKI, M., METCALFE, I. S., PETIT, C., PUXTY, G., REIMER, J., REINER, D. M., RUBIN, E. S., SCOTT, S. A., SHAH, N., SMIT, B., TRUSLER, J. P. M., WEBLEY, P., WILCOX, J. & MAC DOWELL, N. 2018. Carbon capture and storage (CCS): the way forward. *Energy & Environmental Science,* 11**,** 1062-1176.
BURCHETTE, T. P. 2012. Carbonate rocks and petroleum reservoirs: a geological perspective from the industry. *Geological Society, London, Special Publications,* 370**,** 17-37.
CHAKRAVARTY, K. H., FOSBØL, P. L. & THOMSEN, K. Brine Crude Oil Interactions at the Oil-Water Interface. SPE Asia Pacific Enhanced Oil Recovery Conference, 2015. D031S015R004.
CHANDRASEKHAR, S. & MOHANTY, K. K. 2018. Effect of brine composition on oil-rock interaction by atomic force microscopy. *Journal of Petroleum Science and Engineering,* 164**,** 289-301.
CHRISTENSEN, M. & TANINO, Y. 2017. Waterflood Oil Recovery from Mixed-Wet Limestone: Dependence upon the Contact Angle. *Energy & Fuels,* 31**,** 1529-1535.
CHRISTENSEN, M. & TANINO, Y. Residual oil saturation under mixed-wet conditions: optimal wettability revisited. Proc International symposium of the society of core analysts, SCA2018–011, Trondheim, Norway, 2018.
CNUDDE, V. & BOONE, M. N. 2013. High-resolution X-ray computed tomography in geosciences: A review of the current technology and applications. *Earth-Science Reviews,* 123**,** 1-17.
CRAIG, F. F. 1971. *The reservoir engineering aspects of water flooding,* New York, Henry L. Doherty Memorial Fund of AIME.
DANG, C., NGHIEM, L., NGUYEN, N., CHEN, Z. & NGUYEN, Q. 2016. Evaluation of CO 2 Low Salinity Water-Alternating-Gas for enhanced oil recovery. *Journal of Natural Gas Science and Engineering,* 35**,** 237-258.
DANG, C. T., NGHIEM, L. X., CHEN, Z., NGUYEN, Q. P. & NGUYEN, N. T. State-of-the Art Low Salinity Waterflooding for Enhanced Oil Recovery. SPE Asia Pacific Oil and Gas Conference and Exhibition, 2013. SPE-165903-MS.
DANG, C. T. Q., NGHIEM, L. X., CHEN, Z., NGUYEN, N. T. B. & NGUYEN, Q. P. 2014. CO2 Low Salinity Water Alternating Gas: A New Promising Approach for Enhanced Oil Recovery. *SPE Improved Oil Recovery Symposium.* Tulsa, Oklahoma, USA: Society of Petroleum Engineers.

DEN OUDEN, L., NASRALLA, R., GUO, H., BRUINING, H. & VAN KRUIJSDIJK, C. Calcite dissolution behaviour during low salinity water flooding in carbonate rock. IOR 2015-18th European Symposium on Improved Oil Recovery, 2015. European Association of Geoscientists & Engineers, cp-445-00013.
DERKANI, M., FLETCHER, A., ABDALLAH, W., SAUERER, B., ANDERSON, J. & ZHANG, Z. 2018. *Low Salinity Waterflooding in Carbonate Reservoirs: Review of Interfacial Mechanisms*.
DONG, H. & BLUNT, M. J. 2009. Pore-network extraction from micro-computerized-tomography images. *Physical review E,* 80**,** 036307.
DUBOUÉ, J., BOURREL, M., CARRERAS, E. S., KLIMENKO, A., AGENET, N., PASSADE-BOUPAT, N. & LEQUEUX, F. 2019. Auto-Emulsification of Water at the Crude Oil/Water Interface: A Mechanism Driven by Osmotic Gradient. *Energy & Fuels,* 33**,** 7020-7027.
EL-HOSHOUDY, A. N. & DESOUKY, S. 2018. CO2 Miscible Flooding for Enhanced Oil Recovery. *Carbon Capture, Utilization and Sequestration***,** 79.
EMADI, A. & SOHRABI, M. 2013. Visual Investigation of Oil Recovery by Low Salinity Water Injection: Formation of Water Micro-Dispersions and Wettability Alteration. *SPE Annual Technical Conference and Exhibition*.
FARAJZADEH, R., KAHROBAEI, S., EFTEKHARI, A. A., MJENI, R. A., BOERSMA, D. & BRUINING, J. 2021. Chemical enhanced oil recovery and the dilemma of more and cleaner energy. *Scientific Reports,* 11**,** 829.
FATHI, S. J., AUSTAD, T. & STRAND, S. 2010. "Smart Water" as a Wettability Modifier in Chalk: The Effect of Salinity and Ionic Composition. *Energy & Fuels,* 24**,** 2514-2519.
FATTAHI MEHRABAN, M., FARZANEH, S. A. & SOHRABI, M. 2021. Functional compounds of crude oil during low salinity water injection. *Fuel,* 285**,** 119144.
FATTAHI MEHRABAN, M., FARZANEH, S. A., SOHRABI, M. & SISSON, A. 2020. Novel Insights into the Pore-Scale Mechanism of Low Salinity Water Injection and the Improvements on Oil Recovery. *Energy & Fuels,* 34**,** 12050-12064.
FLANNERY, B. P., DECKMAN, H. W., ROBERGE, W. G. & D'AMICO, K. L. 1987. Three-Dimensional X-Ray Microtomography. *Science,* 237**,** 1439-1444.
FREDRIKSEN, S. B., ROGNMO, A. U. & FERNØ, M. A. Pore-scale mechanisms during low salinity waterflooding: water diffusion and osmosis for oil mobilization. SPE bergen one day seminar, 2016. OnePetro.
FREDRIKSEN, S. B., ROGNMO, A. U. & FERNØ, M. A. 2018. Pore-scale mechanisms during low salinity waterflooding: Oil mobilization by diffusion and osmosis. *Journal of Petroleum Science and Engineering,* 163**,** 650-660.
GAO, Y., RAEINI, A. Q., BLUNT, M. J. & BIJELJIC, B. 2019. Pore occupancy, relative permeability and flow intermittency measurements using X-ray micro-tomography in a complex carbonate. *Advances in Water Resources,* 129**,** 56-69.
GAO, Y., RAEINI, A. Q., SELEM, A. M., BONDINO, I., BLUNT, M. J. & BIJELJIC, B. 2020. Pore-scale imaging with measurement of relative permeability and capillary pressure on the same reservoir sandstone sample under water-wet and mixed-wet conditions. *Advances in Water Resources,* 146**,** 103786.
GAUSS, K. F. & PESIC, P. 2005. *General investigations of curved surfaces*, Courier Corporation.
GOMARI, K. R., DENOYEL, R. & HAMOUDA, A. 2006. Wettability of calcite and mica modified by different long-chain fatty acids (C18 acids). *Journal of colloid and interface science,* 297**,** 470-479.
GRAUE, A., VIKSUND, B. G., EILERTSEN, T. & MOE, R. 1999. Systematic wettability alteration by aging sandstone and carbonate rock in crude oil. *Journal of Petroleum Science and Engineering,* 24**,** 85-97.
HAMOUDA, A. A. & GOMARI, K. R. Influence of temperature on wettability alteration of carbonate reservoirs. SPE/DOE Symposium on Improved Oil Recovery, 2006. OnePetro.
IBEKWE, A., POKRAJAC, D. & TANINO, Y. 2020. Automated extraction of in situ contact angles from micro-computed tomography images of porous media. *Computers & Geosciences,* 137**,** 104425.
IEA 2022. World Energy Outlook 2022. IEA (2022), , IEA, Paris.

IGLAUER, S., FAVRETTO, S., SPINELLI, G., SCHENA, G. & BLUNT, M. J. 2010. X-ray tomography measurements of power-law cluster size distributions for the nonwetting phase in sandstones. *Physical Review E,* 82**,** 056315.

JACKSON, M. D., AL-MAHROUQI, D. & VINOGRADOV, J. 2016a. Zeta potential in oil-water-carbonate systems and its impact on oil recovery during controlled salinity water-flooding. *Scientific Reports,* 6**,** 37363.

JACKSON, M. D., VINOGRADOV, J., HAMON, G. & CHAMEROIS, M. 2016b. Evidence, mechanisms and improved understanding of controlled salinity waterflooding part 1: Sandstones. *Fuel,* 185**,** 772-793.

JADHUNANDAN, P. & MORROW, N. R. 1995a. Effect of wettability on waterflood recovery for crude-oil/brine/rock systems. *SPE reservoir engineering,* 10**,** 40-46.

JADHUNANDAN, P. P. & MORROW, N. R. 1995b. Effect of Wettability on Waterflood Recovery for Crude-Oil/Brine/Rock Systems. *SPE Reservoir Engineering,* 10**,** 40-46.

JONES, A. C., ARNS, C. H., SHEPPARD, A. P., HUTMACHER, D. W., MILTHORPE, B. K. & KNACKSTEDT, M. A. 2007. Assessment of bone ingrowth into porous biomaterials using MICRO-CT. *Biomaterials,* 28**,** 2491-2504.

KAR, T., CHO, H. & FIROOZABADI, A. 2022. Assessment of low salinity waterflooding in carbonate cores: Interfacial viscoelasticity and tuning process efficiency by use of non-ionic surfactant. *Journal of Colloid and Interface Science,* 607**,** 125-133.

KETCHAM, R. A. & CARLSON, W. D. 2001. Acquisition, optimization and interpretation of X-ray computed tomographic imagery: applications to the geosciences. *Computers & Geosciences,* 27**,** 381-400.

KHISHVAND, M., ALIZADEH, A., KOHSHOUR, I. O., PIRI, M. & PRASAD, R. 2017a. In situ characterization of wettability alteration and displacement mechanisms governing recovery enhancement due to low-salinity waterflooding. *Water Resources Research,* 53**,** 4427-4443.

KHISHVAND, M., ALIZADEH, A. H., ORAKI KOHSHOUR, I., PIRI, M. & PRASAD, R. S. 2017b. In situ characterization of wettability alteration and displacement mechanisms governing recovery enhancement due to low-salinity waterflooding. *Water Resources Research,* 53**,** 4427-4443.

KHISHVAND, M., ALIZADEH, A. H. & PIRI, M. 2016. In-situ characterization of wettability and pore-scale displacements during two- and three-phase flow in natural porous media. *Advances in Water Resources,* 97**,** 279-298.

KHISHVAND, M., ORAKI KOHSHOUR, I., ALIZADEH, A. H., PIRI, M. & PRASAD, S. 2019. A multi-scale experimental study of crude oil-brine-rock interactions and wettability alteration during low-salinity waterflooding. *Fuel,* 250**,** 117-131.

KLISE, K. A., MORIARTY, D., YOON, H. & KARPYN, Z. 2016. Automated contact angle estimation for three-dimensional X-ray microtomography data. *Advances in water resources,* 95**,** 152-160.

KNEBEL, G. M. & RODRIGUEZ-ERASO, G. 1956. Habitat of Some Oil1. *AAPG Bulletin,* 40**,** 547-561.

KUMAR, M., FOGDEN, A., MORROW, N. R. & BUCKLEY, J. S. 2011. Mechanisms of Improved Oil Recovery From Sandstone by Low Salinity Flooding. *Petrophysics - The SPWLA Journal of Formation Evaluation and Reservoir Description,* 52**,** 428-436.

KUMAR, S., RAO, A., ALOTAIBI, M. B., AYIRALA, S. C., YOUSEF, A. A., SIRETANU, I. & MUGELE, F. 2021. Response of crude oil deposited organic layers to brines of different salinity: An atomic force microscopy study on carbonate surfaces. *Fuel,* 302**,** 121129.

LAGER, A., WEBB, K. J., BLACK, C. J. J., SINGLETON, M. & SORBIE, K. S. 2008. Low Salinity Oil Recovery - An Experimental Investigation1. *Petrophysics,* 49**,** 8.

LEBEDEVA, E. V. & FOGDEN, A. 2011. Micro-CT and Wettability Analysis of Oil Recovery from Sand Packs and the Effect of Waterflood Salinity and Kaolinite. *Energy & Fuels,* 25**,** 5683-5694.

LI, S., JACKSON, M. D. & AGENET, N. 2020. Role of the calcite-water interface in wettability alteration during low salinity waterflooding. *Fuel,* 276**,** 118097.

LIN, Q., AKAI, T., BLUNT, M. J., BIJELJIC, B., IWAMA, H., TAKABAYASHI, K., ONAKA, Y. & YONEBAYASHI, H. 2021. Pore-scale imaging of asphaltene-induced pore clogging in carbonate rocks. *Fuel,* 283**,** 118871.

LIN, Q., AL-KHULAIFI, Y., BLUNT, M. J. & BIJELJIC, B. 2016. Quantification of sub-resolution porosity in carbonate rocks by applying high-salinity contrast brine using X-ray microtomography differential imaging. *Advances in Water Resources,* 96**,** 306-322.

LIN, Q., BIJELJIC, B., BERG, S., PINI, R., BLUNT, M. J. & KREVOR, S. 2019. Minimal surfaces in porous media: Pore-scale imaging of multiphase flow in an altered-wettability Bentheimer sandstone. *Physical Review E,* 99**,** 063105.

LIU, Z., HERRING, A., ARNS, C., BERG, S. & ARMSTRONG, R. T. 2017. Pore-Scale Characterization of Two-Phase Flow Using Integral Geometry. *Transport in Porous Media,* 118**,** 99-117.

MAHANI, H., BERG, S., ILIC, D., BARTELS, W.-B.-B. & JOEKAR-NIASAR, V. 2014. Kinetics of Low-Salinity-Flooding Effect. *SPE Journal,* 20**,** 8-20.

MAHANI, H., KEYA, A. L., BERG, S., BARTELS, W.-B., NASRALLA, R. & ROSSEN, W. R. 2015. Insights into the Mechanism of Wettability Alteration by Low-Salinity Flooding (LSF) in Carbonates. *Energy & Fuels,* 29**,** 1352-1367.

MAHANI, H., MENEZES, R., BERG, S., FADILI, A., NASRALLA, R., VOSKOV, D. & JOEKAR-NIASAR, V. 2017. Insights into the Impact of Temperature on the Wettability Alteration by Low Salinity in Carbonate Rocks. *Energy & Fuels,* 31**,** 7839-7853.

MAHANI, H., SOROP, T., LIGTHELM, D. J., BROOKS, D., VLEDDER, P., MOZAHEM, F. & ALI, Y. 2011. Analysis of field responses to low-salinity waterflooding in secondary and tertiary mode in Syria. *SPE Europec/EAGE Annual Conference and Exhibition*.

MAHZARI, P. & SOHRABI, M. Crude Oil/Brine Interactions and Spontaneous Formation of Micro-Dispersions in Low Salinity Water Injection. SPE Improved Oil Recovery Symposium, 2014. SPE-169081-MS.

MAHZARI, P., SOHRABI, M., COOKE, A. J. & CARNEGIE, A. 2018. Direct pore-scale visualization of interactions between different crude oils and low salinity brine. *Journal of Petroleum Science and Engineering,* 166**,** 73-84.

MAHZARI, P., SOHRABI, M. & FAÇANHA, J. M. 2019. The Decisive Role of Microdispersion Formation in Improved Oil Recovery by Low-Salinity-Water Injection in Sandstone Formations. *SPE Journal,* 24**,** 2859-2873.

MCGUIRE, P. L., CHATHAM, J. R., PASKVAN, F. K., SOMMER, D. M. & CARINI, F. H. 2005. Low Salinity Oil Recovery: An Exciting New EOR Opportunity for Alaska's North Slope. *SPE Western Regional Meeting*.

MENKE, H. P., BIJELJIC, B., ANDREW, M. G. & BLUNT, M. J. 2015. Dynamic Three-Dimensional Pore-Scale Imaging of Reaction in a Carbonate at Reservoir Conditions. *Environmental Science & Technology,* 49**,** 4407-4414.

MIRCHI, V. Pore-Scale Investigation of the Effect of Surfactant on Fluid Occupancies during Low-Salinity Waterflooding in Oil-Wet Carbonates. SPE Annual Technical Conference and Exhibition, 2018. D023S099R020.

MOHAMMADI, M. & MAHANI, H. 2020. Direct insights into the pore-scale mechanism of low-salinity waterflooding in carbonates using a novel calcite microfluidic chip. *Fuel,* 260**,** 116374.

MORROW, N. & BUCKLEY, J. 2011. Improved Oil Recovery by Low-Salinity Waterflooding. *Journal of Petroleum Technology,* 63**,** 106-112.

MORROW, N. R. 1970. Physics and thermodynamics of capillary action in porous media. *Industrial & Engineering Chemistry,* 62**,** 32-56.

MORROW, N. R., CRAM, P. J. & MCCAFFERY, F. 1973. Displacement studies in dolomite with wettability control by octanoic acid. *Society of Petroleum Engineers Journal,* 13**,** 221-232.

MORROW, N. R., TANG, G.-Q., VALAT, M. & XIE, X. 1998. Prospects of improved oil recovery related to wettability and brine composition. *Journal of Petroleum Science and Engineering,* 20**,** 267-276.

MUGGERIDGE, A., COCKIN, A., WEBB, K., FRAMPTON, H., COLLINS, I., MOULDS, T. & SALINO, P. 2014. Recovery rates, enhanced oil recovery and technological limits. *Philosophical Transactions of the Royal Society A: Mathematical, Physical and Engineering Sciences,* 372**,** 20120320.

MUNGAN, N. 1981. Carbon Dioxide Flooding-fundamentals. *Journal of Canadian Petroleum Technology,* 20**,** 7.

NASRALLA, R. A., SERGIENKO, E., MASALMEH, S. K., VAN DER LINDE, H. A., BRUSSEE, N. J., MAHANI, H., SUIJKERBUIJK, B. M. & AL-QARSHUBI, I. S. 2016. Potential of Low-Salinity Waterflood To Improve Oil Recovery in Carbonates: Demonstrating the Effect by Qualitative Coreflood. *SPE Journal,* 21**,** 1643-1654.

NASRALLA, R. A., SERGIENKO, E., VAN DER LINDE, H. A., BRUSSEE, N. J., MAHANI, H., SUIJKERBUIJK, B. M., AL-QARSHUBI, I. S. & MASALMEH, S. K. Demonstrating the Potential of Low-Salinity Waterflood to Improve Oil Recovery in Carbonate Reservoirs by Qualitative Coreflood. Abu Dhabi International Petroleum Exhibition and Conference, 2014. D041S074R001.

NIU, B., AL-MENHALI, A. & KREVOR, S. C. 2015. The impact of reservoir conditions on the residual trapping of carbon dioxide in B erea sandstone. *Water Resources Research,* 51**,** 2009-2029.

PIÑEREZ TORRIJOS, I. D., PUNTERVOLD, T., STRAND, S., AUSTAD, T., ABDULLAH, H. I. & OLSEN, K. 2016. Experimental Study of the Response Time of the Low-Salinity Enhanced Oil Recovery Effect during Secondary and Tertiary Low-Salinity Waterflooding. *Energy & Fuels,* 30**,** 4733-4739.

QIN, Z., ARSHADI, M. & PIRI, M. 2019. Micro-scale experimental investigations of multiphase flow in oil-wet carbonates. I. In situ wettability and low-salinity waterflooding. *Fuel,* 257**,** 116014.

RAEINI, A. Q., BIJELJIC, B. & BLUNT, M. J. 2017. Generalized network modeling: Network extraction as a coarse-scale discretization of the void space of porous media. *Physical Review E,* 96**,** 013312.

REZAEIDOUST, A., PUNTERVOLD, T., STRAND, S. & AUSTAD, T. 2009. Smart Water as Wettability Modifier in Carbonate and Sandstone: A Discussion of Similarities/Differences in the Chemical Mechanisms. *Energy & Fuels,* 23**,** 4479-4485.

SALATHIEL, R. 1973. Oil recovery by surface film drainage in mixed-wettability rocks. *Journal of Petroleum Technology,* 25**,** 1,216-1,224.

SANDENGEN, K. & ARNTZEN, O. Osmosis during low salinity water flooding. IOR 2013-17th European Symposium on Improved Oil Recovery, 2013. European Association of Geoscientists & Engineers, cp-342-00015.

SANDENGEN, K., KRISTOFFERSEN, A., MELHUUS, K. & JØSANG, L. O. 2016. Osmosis as Mechanism for Low-Salinity Enhanced Oil Recovery. *SPE Journal,* 21**,** 1227-1235.

SANDREA, I. & SANDREA, R. 2007. Recovery factors leave vast target for EOR technologies. *Oil & gas journal,* 105**,** 44-47.

SARI, A., XIE, Q., CHEN, Y., SAEEDI, A. & POORYOUSEFY, E. 2017. Drivers of low salinity effect in carbonate reservoirs. *Energy & Fuels,* 31**,** 8951-8958.

SCANZIANI, A., LIN, Q., ALHOSANI, A., BLUNT, M. J. & BIJELJIC, B. 2020. Dynamics of fluid displacement in mixed-wet porous media. *Proceedings of the Royal Society A,* 476**,** 20200040.

SCANZIANI, A., SINGH, K., BLUNT, M. J. & GUADAGNINI, A. 2017. Automatic method for estimation of in situ effective contact angle from X-ray micro tomography images of two-phase flow in porous media. *Journal of colloid and interface science,* 496**,** 51-59.

SCANZIANI, A., SINGH, K., BULTREYS, T., BIJELJIC, B. & BLUNT, M. J. 2018. In situ characterization of immiscible three-phase flow at the pore scale for a water-wet carbonate rock. *Advances in Water Resources,* 121**,** 446-455.

SCHLÜTER, S., SHEPPARD, A., BROWN, K. & WILDENSCHILD, D. 2014. Image processing of multiphase images obtained via X-ray microtomography: a review. *Water Resources Research,* 50**,** 3615-3639.

SECCOMBE, J. C., LAGER, A., WEBB, K. J., JERAULD, G. & FUEG, E. 2008. Improving Wateflood Recovery: LoSalTM EOR Field Evaluation. *SPE Symposium on Improved Oil Recovery.* Tulsa, Oklahoma, USA: Society of Petroleum Engineers.

SELEM, A. M., AGENET, N., BLUNT, M. J. & BIJELJIC, B. Pore-Scale Imaging of Tertiary Low Salinity Waterflooding in a Heterogeneous Carbonate Rock at Reservoir Conditions. SPE Annual Technical Conference and Exhibition, 2021a. D031S059R003.

SELEM, A. M., AGENET, N., BLUNT, M. J. & BIJELJIC, B. 2022. Pore-scale processes in tertiary low salinity waterflooding in a carbonate rock: Micro-dispersions, water film growth, and wettability change. *J Colloid Interface Sci,* 628**,** 486-498.

SELEM, A. M., AGENET, N., GAO, Y., RAEINI, A. Q., BLUNT, M. J. & BIJELJIC, B. 2021b. Pore-scale imaging and analysis of low salinity waterflooding in a heterogeneous carbonate rock at reservoir conditions. *Scientific Reports,* 11**,** 15063.

SHABANINEJAD, M., MIDDLELTON, J. & FOGDEN, A. 2018. Systematic pore-scale study of low salinity recovery from Berea sandstone analyzed by micro-CT. *Journal of Petroleum Science and Engineering,* 163**,** 283-294.

SHEHATA, A. M. M., ALOTAIBI, M. B. B. & NASR-EL-DIN, H. A. A. 2014. Waterflooding in Carbonate Reservoirs: Does the Salinity Matter? *SPE Reservoir Evaluation & Engineering,* 17**,** 304-313.

SINGH, K., BIJELJIC, B. & BLUNT, M. J. 2016. Imaging of oil layers, curvature and contact angle in a mixed-wet and a water-wet carbonate rock. *Water Resources Research,* 52**,** 1716-1728.

SMALLEY, P. C., MUGGERIDGE, A. H., AMUNDRUD, S. S., DALLAND, M., HELVIG, O. S., HØGNESEN, E. J., VALVATNE, P. & ØSTHUS, A. EOR screening including technical, operational, environmental and economic factors reveals practical EOR potential offshore on the Norwegian Continental Shelf. SPE Improved Oil Recovery Conference, 2020. OnePetro.

SMALLEY, P. C., MUGGERIDGE, A. H., DALLAND, M., HELVIG, O. S., HØGNESEN, E. J., HETLAND, M. & ØSTHUS, A. 2018. Screening for EOR and Estimating Potential Incremental Oil Recovery on the Norwegian Continental Shelf. *SPE Improved Oil Recovery Conference.*

SOHRABI, M., MAHZARI, P., FARZANEH, S. A., MILLS, J. R., TSOLIS, P. & IRELAND, S. 2017. Novel Insights Into Mechanisms of Oil Recovery by Use of Low-Salinity-Water Injection. *SPE Journal,* 22**,** 407-416.

STRAND, S., HØGNESEN, E. J. & AUSTAD, T. 2006. Wettability alteration of carbonates—Effects of potential determining ions (Ca2+ and SO42−) and temperature. *Colloids and Surfaces A: Physicochemical and Engineering Aspects,* 275**,** 1-10.

SUN, C., MCCLURE, J. E., MOSTAGHIMI, P., HERRING, A. L., MEISENHEIMER, D. E., WILDENSCHILD, D., BERG, S. & ARMSTRONG, R. T. 2020. Characterization of wetting using topological principles. *Journal of Colloid and Interface Science,* 578**,** 106-115.

SWEATMAN, R. E., CROOKSHANK, S. & EDMAN, S. 2011. Outlook and Technologies for Offshore CO2 EOR/CCS Projects. *Offshore Technology Conference.* Houston, Texas, USA: Offshore Technology Conference.

TANG, G.-Q. & MORROW, N. R. 1999. Influence of brine composition and fines migration on crude oil/brine/rock interactions and oil recovery. *Journal of Petroleum Science and Engineering,* 24**,** 99-111.

TANG, G. Q. & MORROW, N. R. 1997. Salinity, Temperature, Oil Composition, and Oil Recovery by Waterflooding. *SPE Reservoir Engineering,* 12**,** 269-276.

TANINO, Y. & BLUNT, M. J. 2012. Capillary trapping in sandstones and carbonates: Dependence on pore structure. *Water Resources Research,* 48.

TANINO, Y. & CHRISTENSEN, M. 2019. Imbibition capillary pressure and relative permeability of mixed-wet microporous rock: new insights from history matching. *Transport in Porous Media,* 129**,** 121-148.

TAUBIN, G. Curve and surface smoothing without shrinkage. Proceedings of IEEE international conference on computer vision, 1995. IEEE, 852-857.

TAWFIK, M., KARPYN, Z. & JOHNS, R. Multiscale study of chemically-tuned waterflooding in carbonate rocks using micro-computed tomography. IOR 2019–20th European Symposium on Improved Oil Recovery, 2019. European Association of Geoscientists & Engineers, 1-23.

TEKLU, T. W., ALAMERI, W., KAZEMI, H., GRAVES, R. M. & ALSUMAITI, A. M. 2017. Low salinity water–Surfactant–CO2 EOR. *Petroleum,* 3**,** 309-320.

TETTEH, J. T., BRADY, P. V. & BARATI GHAHFAROKHI, R. 2020. Review of low salinity waterflooding in carbonate rocks: mechanisms, investigation techniques, and future directions. *Advances in Colloid and Interface Science,* 284**,** 102253.

TOOLE, S. & GRIST, D. Oil and gas recovery behaviour in the UKCS basins. Offshore Europe, 2003. Society of Petroleum Engineers.

TREIBER, L. E. & OWENS, W. W. 1972. A Laboratory Evaluation of the Wettability of Fifty Oil-Producing Reservoirs. *Society of Petroleum Engineers Journal,* 12**,** 531-540.

UNSAL, E., RÜCKER, M., BERG, S., BARTELS, W. B. & BONNIN, A. 2019. Imaging of compositional gradients during in situ emulsification using X-ray micro-tomography. *Journal of Colloid and Interface Science,* 550**,** 159-169.

VAN POOLLEN, H. 1980. Fundamentals of enhanced oil recovery.

VLEDDER, P., GONZALEZ, I. E., CARRERA FONSECA, J. C., WELLS, T. & LIGTHELM, D. J. 2010. Low Salinity Water Flooding: Proof Of Wettability Alteration On A Field Wide Scale. *SPE Improved Oil Recovery Symposium.* Tulsa, Oklahoma, USA: Society of Petroleum Engineers.

WAGNER, O. & LEACH, R. 1959. Improving oil displacement efficiency by wettability adjustment. *Transactions of the AIME,* 216**,** 65-72.

WALSH, J. M. 2015. Produced-Water-Treating Systems: Comparison of North Sea and Deepwater Gulf of Mexico. *Oil and Gas Facilities,* 4**,** 073-086.

WEI, B., WU, R., LU, L., NING, X., XU, X., WOOD, C. & YANG, Y. 2017. Influence of Individual Ions on Oil/Brine/Rock Interfacial Interactions and Oil–Water Flow Behaviors in Porous Media. *Energy & Fuels,* 31**,** 12035-12045.

WILDENSCHILD, D. & SHEPPARD, A. P. 2013. X-ray imaging and analysis techniques for quantifying pore-scale structure and processes in subsurface porous medium systems. *Advances in Water Resources,* 51**,** 217-246.

WILSON, A. 2015. CO2 Low-Salinity Water Alternating Gas: A Promising New Approach for EOR. *Journal of Petroleum Technology,* 67**,** 84-86.

WU, Y., SHULER, P. J., BLANCO, M., TANG, Y. & GODDARD, W. A. A study of wetting behavior and surfactant EOR in carbonates with model compounds. SPE/DOE Symposium on Improved Oil Recovery, 2006. OnePetro.

YOUSEF, A. A., AL-SALEH, S. & AL-JAWFI, M. 2012a. Improved/Enhanced Oil Recovery from Carbonate Reservoirs by Tuning Injection Water Salinity and Ionic Content. *SPE Improved Oil Recovery Symposium*.

YOUSEF, A. A., AL-SALEH, S. H., AL-KAABI, A. & AL-JAWFI, M. S. 2011. Laboratory Investigation of the Impact of Injection-Water Salinity and Ionic Content on Oil Recovery From Carbonate Reservoirs. *SPE Reservoir Evaluation & Engineering,* 14**,** 578-593.

YOUSEF, A. A., LIU, J., BLANCHARD, G., AL-SALEH, S., AL-ZAHRANI, T., AL-ZAHRANI, R., AL-TAMMAR, H. & AL-MULHIM, N. 2012b. SmartWater Flooding: Industry's First Field Test in Carbonate Reservoirs. *SPE Annual Technical Conference and Exhibition*.

ZAHID, A., SHAPIRO, A. & SKAUGE, A. Experimental Studies of Low Salinity Water Flooding in Carbonate Reservoirs: A New Promising Approach. SPE EOR Conference at Oil and Gas West Asia, 2012. SPE-155625-MS.

ZHANG, P. & AUSTAD, T. 2006. Wettability and oil recovery from carbonates: Effects of temperature and potential determining ions. *Colloids and Surfaces A: Physicochemical and Engineering Aspects,* 279**,** 179-187.

ZHANG, P., TWEHEYO, M. T. & AUSTAD, T. 2007. Wettability alteration and improved oil recovery by spontaneous imbibition of seawater into chalk: Impact of the potential determining ions Ca2+, Mg2+, and SO42−. *Colloids and Surfaces A: Physicochemical and Engineering Aspects,* 301**,** 199-208.

Appendices

9.1 Appendix 1

Raw X-ray images illustrating the image acquisition process as well as additional illustration showing the image processing and analysis techniques.

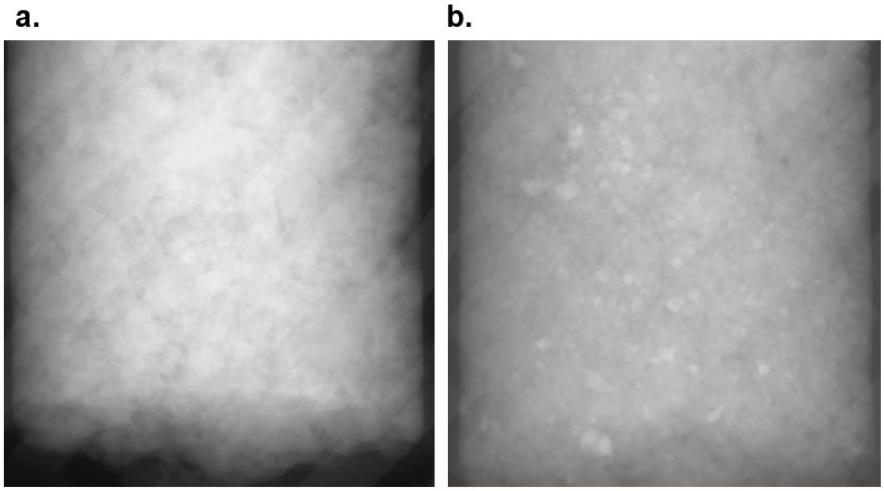

Figure 9.1: The two limestone samples; Estaillades (a) and reservoir (b), used in this study under X-rays.

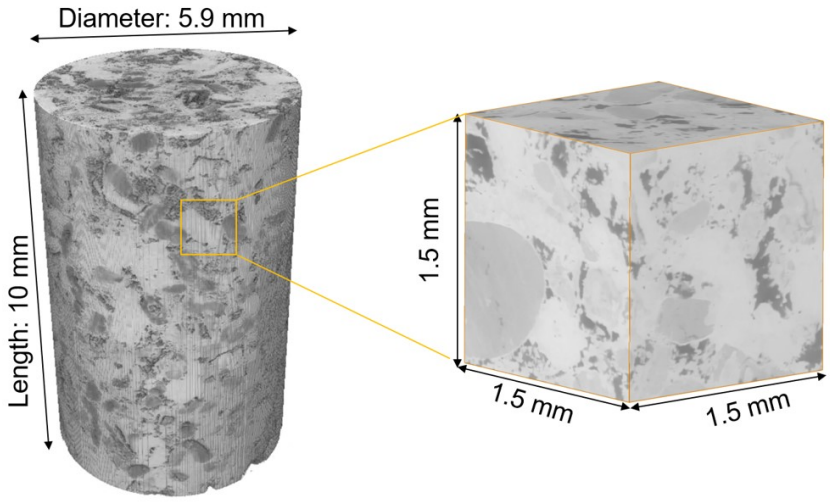

Figure 9.2: A tomogram of the sample used in this study with a total volume of 28.8 billion voxels. Contact angle and curvature measurements were performed on an extracted sub-volume (1.5 mm^3).

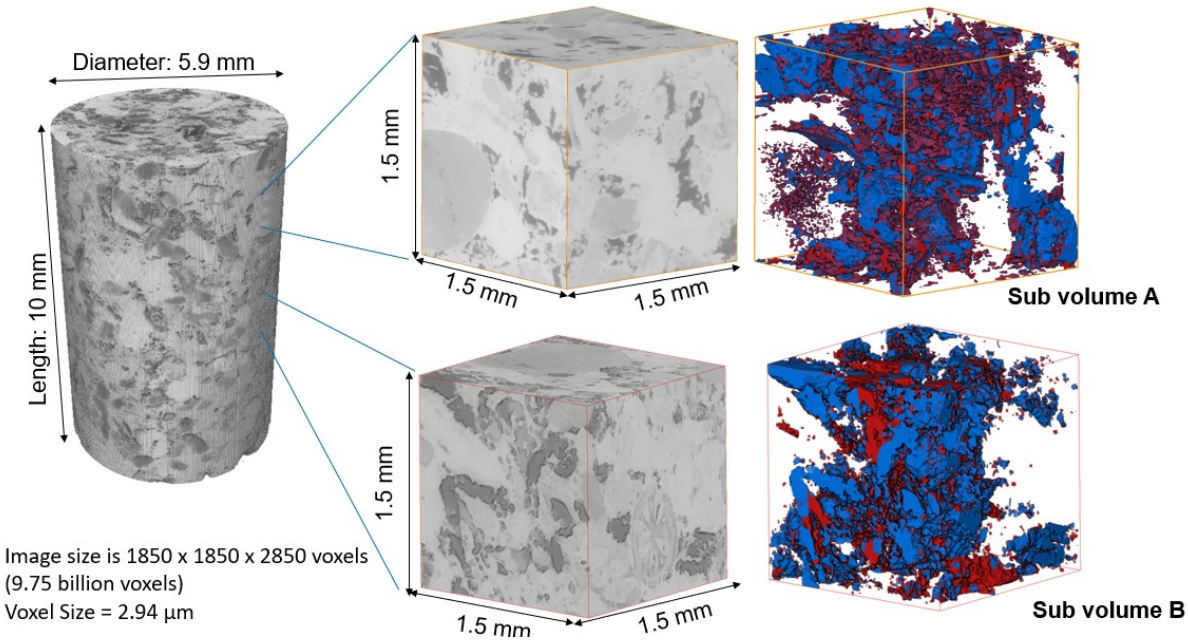

Figure 9.3: Multiple sub-volumes extracted to perform interfacial analyses. Blue is water and red is oil.

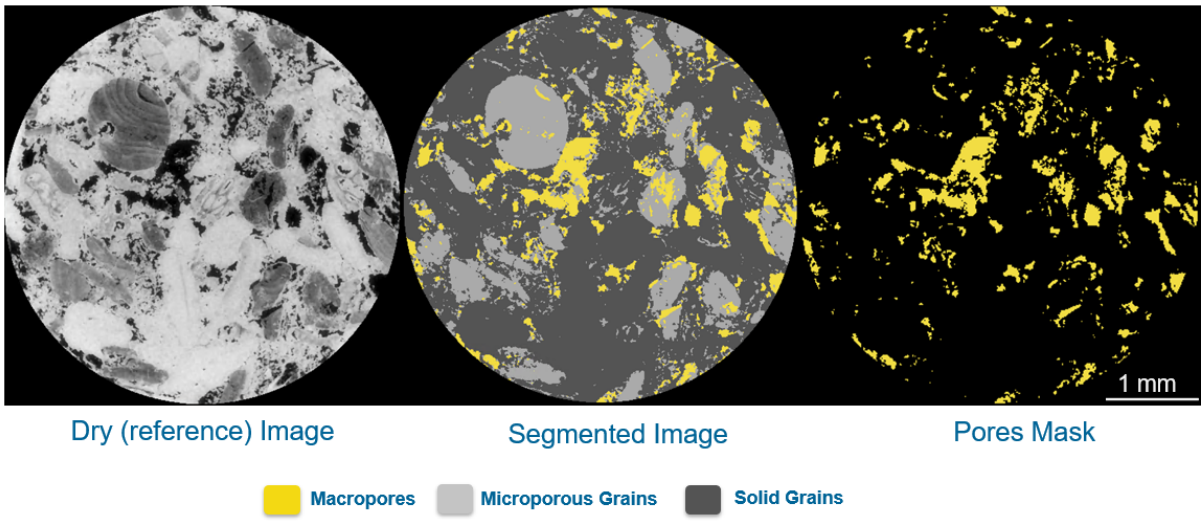

Figure 9.4: Pore mask application procedure to extract the pore network.

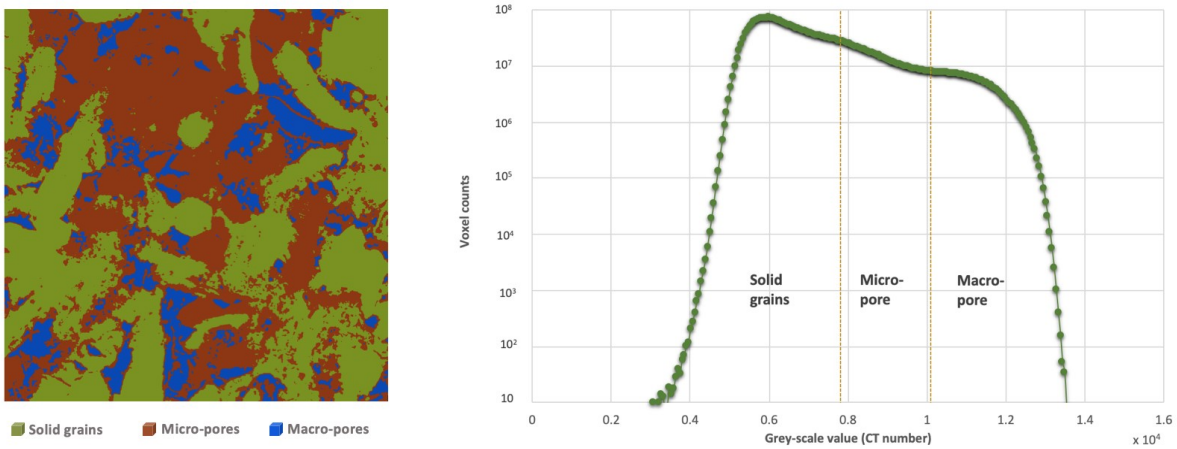

Figure 9.5: Segmentation of differential image to characterise rock dual porosity.

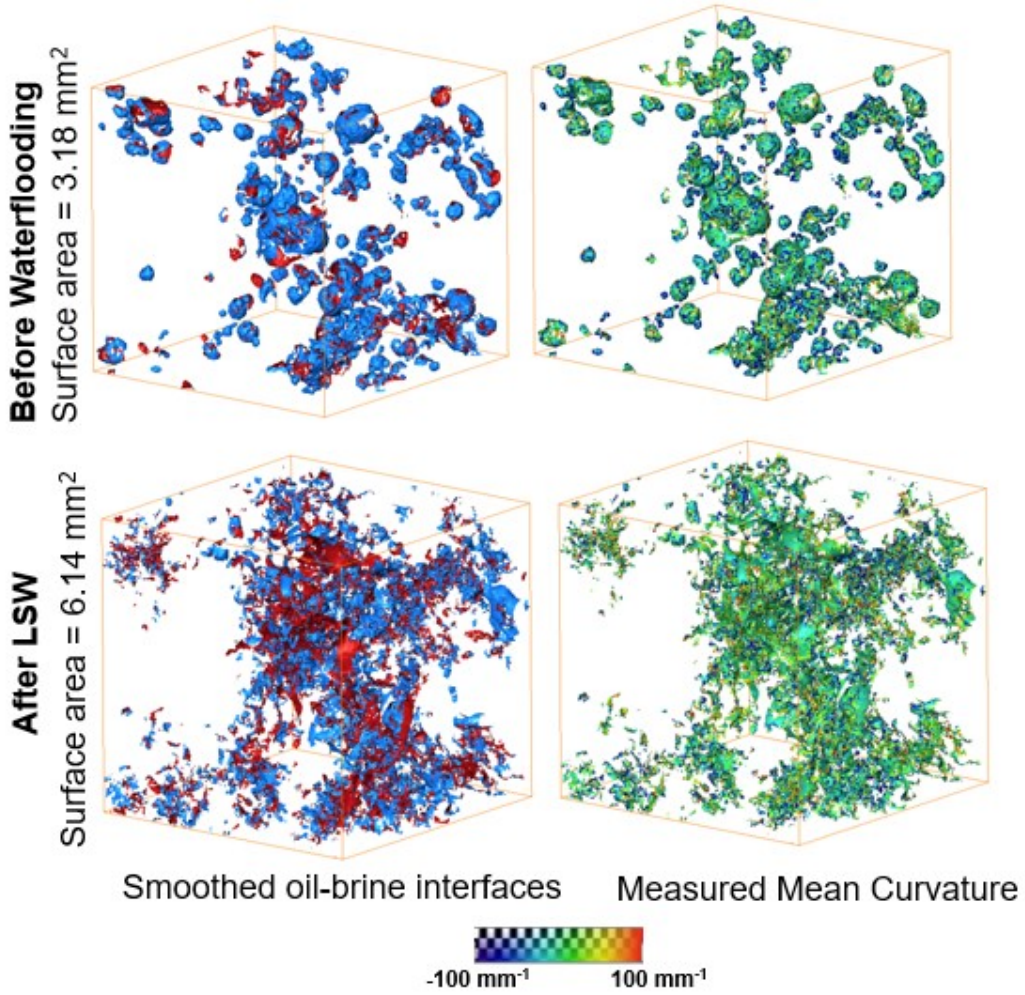

Figure 9.6: Mean curvature measurements from smoothed oil/brine surfaces.

9.2 Appendix 2

Additional image analysis results including greyscale and segmented images, and saturation profiles. Further examples from different pores are shown to highlight the oil displacement mechanisms during high and low salinity waterflooding.

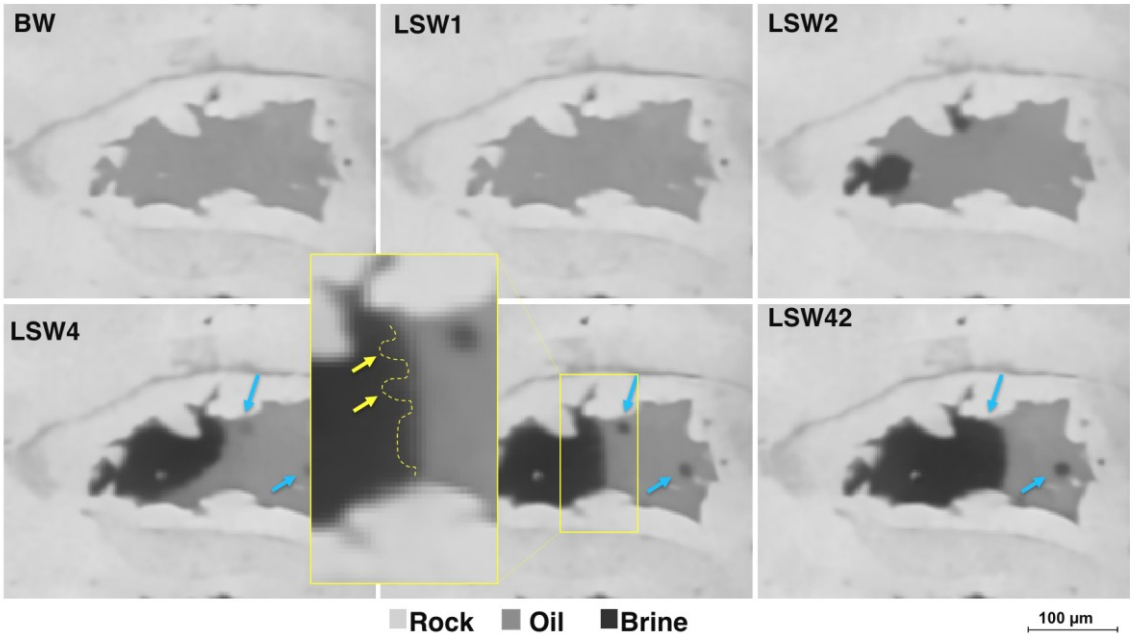

Figure 9.7: Water-in-oil oil micro-droplet radius was evaluated at 8 µm which is consistent with direct microscopic observation.

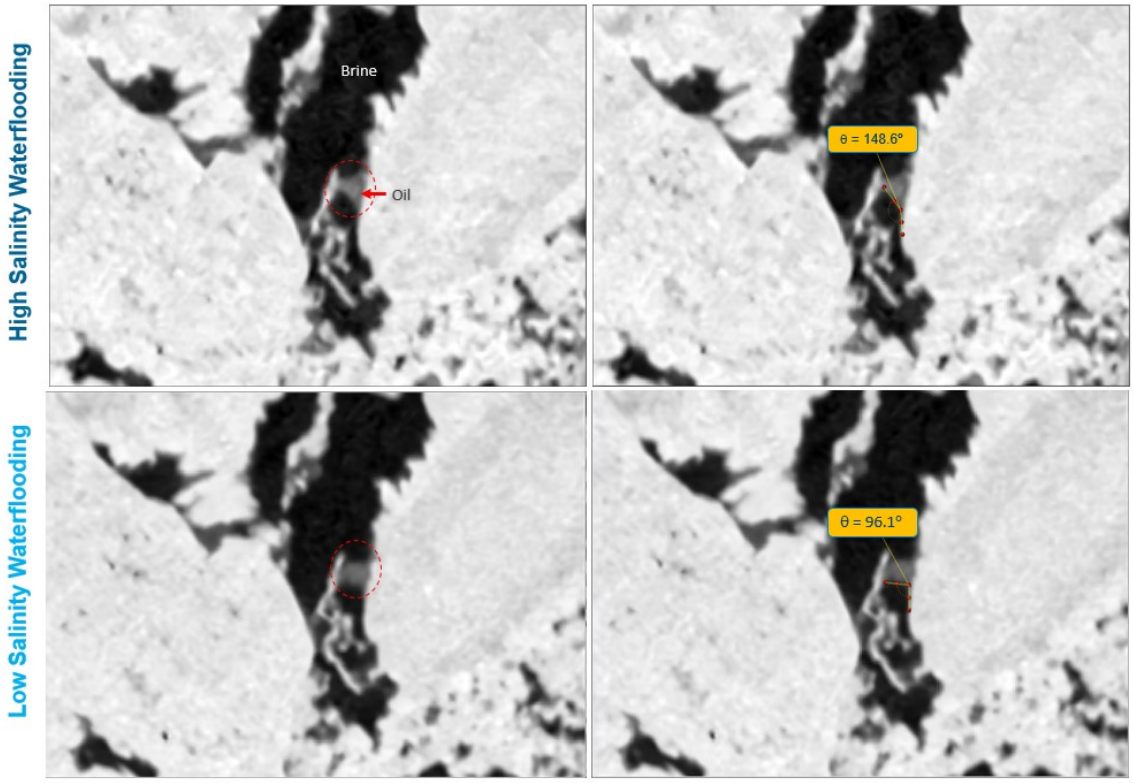

Figure 9.8: Manual measurement of contact angle in a pore shows a large change from 148 during HSW to 96 during LSW.

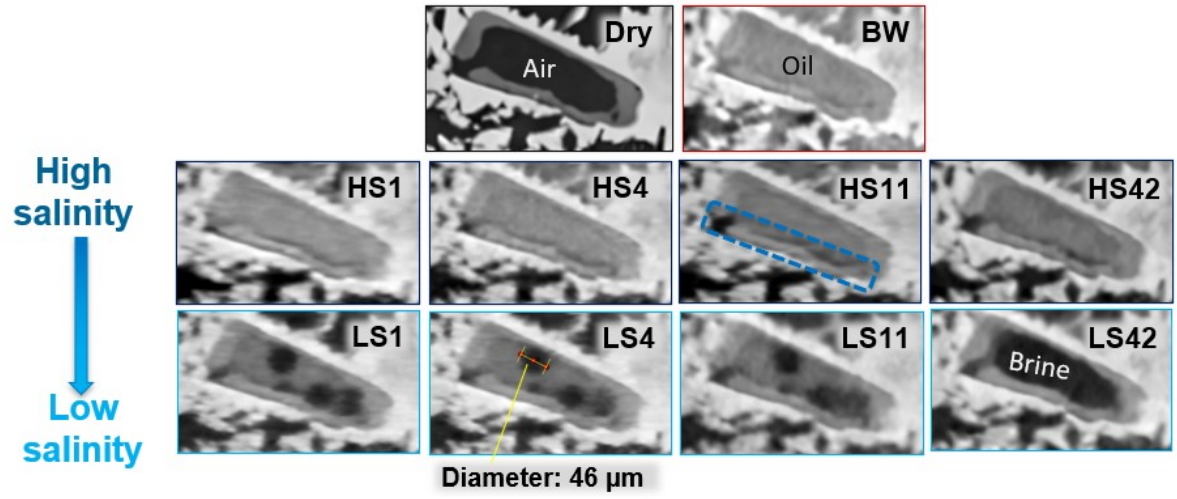

Figure 9.9: Displacement process investigation during tertiary LSW on Estaillades limestone.

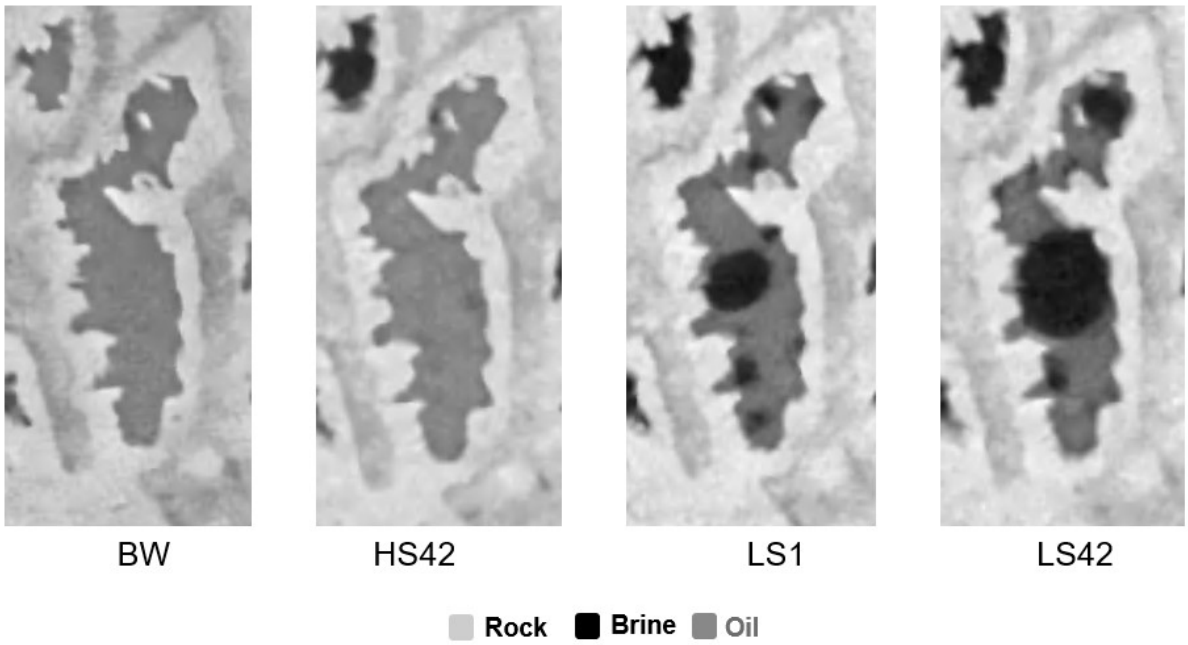

Figure 9.10: Incremental recovery from LSW in tertiary mode is driven by the development of micro-emulsion.

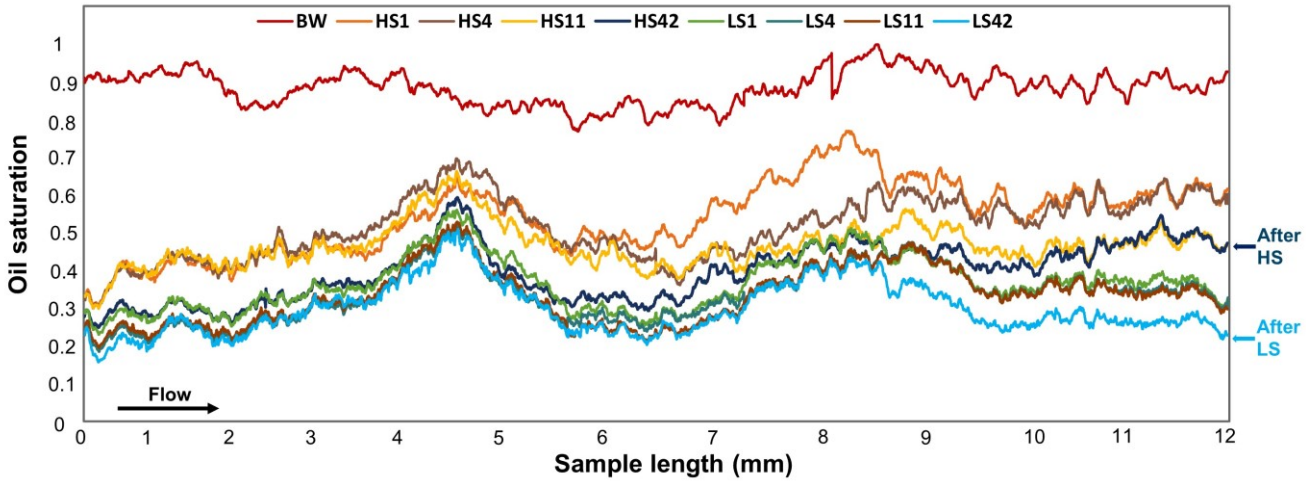

Figure 9.11: Oil saturation profiles across the sample from the left (inlet) to the right (outlet) before waterflooding and after HS and LS floods.

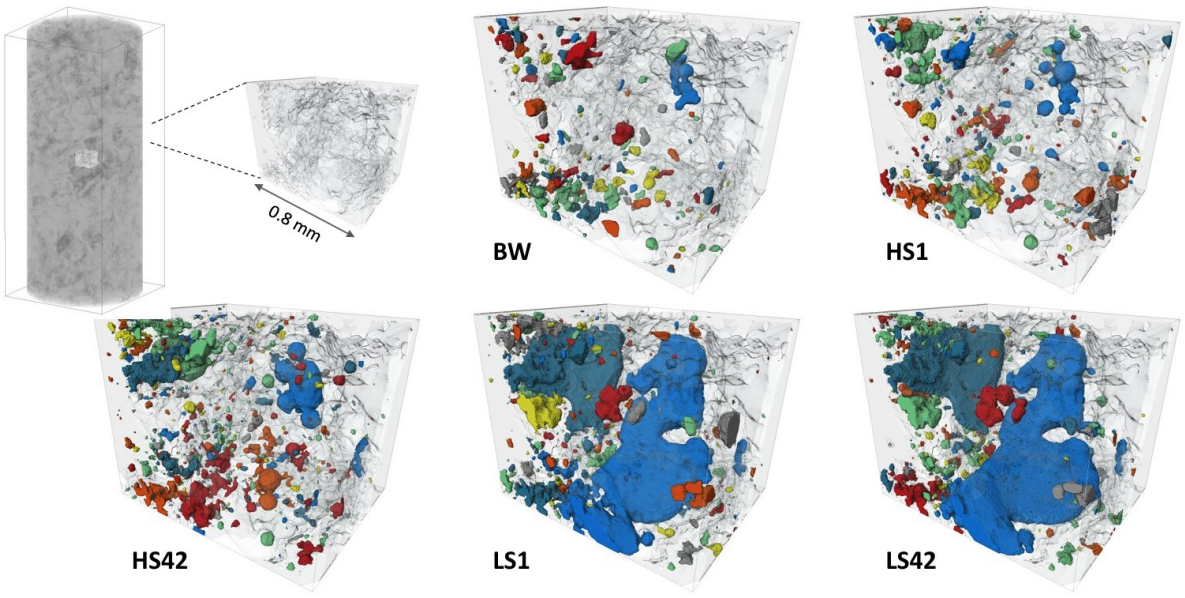

Figure 9.12: Growth of water micro-droplets and connectivity of water domains. Different colours represent different connected brine blobs. Oil is transparent and rock is semi-transparent.

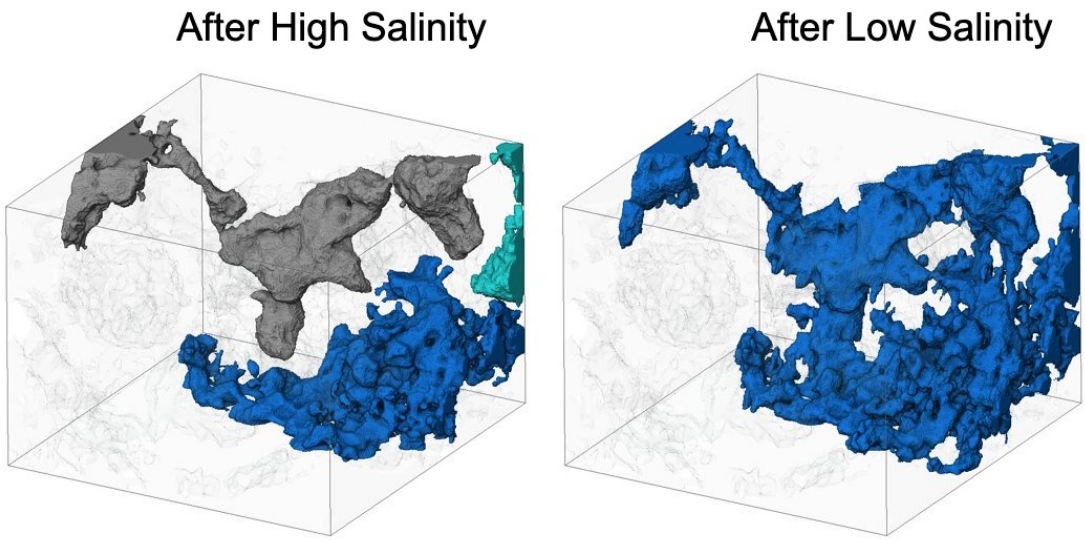

Figure 9.13: Connectivity of water blobs after LSW, indicating the displacement of trapped oil.

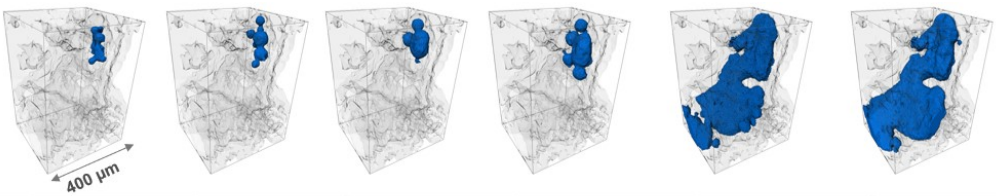

Stage	BW	HS1	HS4	HS42	LS1	LS42
Brine blob volume *(x 10^6 μm^3)*	*0.34*	*0.48*	*0.86*	*1.37*	*10.17*	*11.32*

Figure 9.14: The difference in growth rate of a water blob between HS and LS floods during tertiary LSW in Estaillades limestone. Images from left to right are taken before waterflooding (BW), after high salinity waterflooding at 1, 4 and 42 µL/min, HS1, HS4 and HS42, respectively. And images after low salinity waterflooding at rates 1 and 42µL/min, LS1 and LS42, respectively.

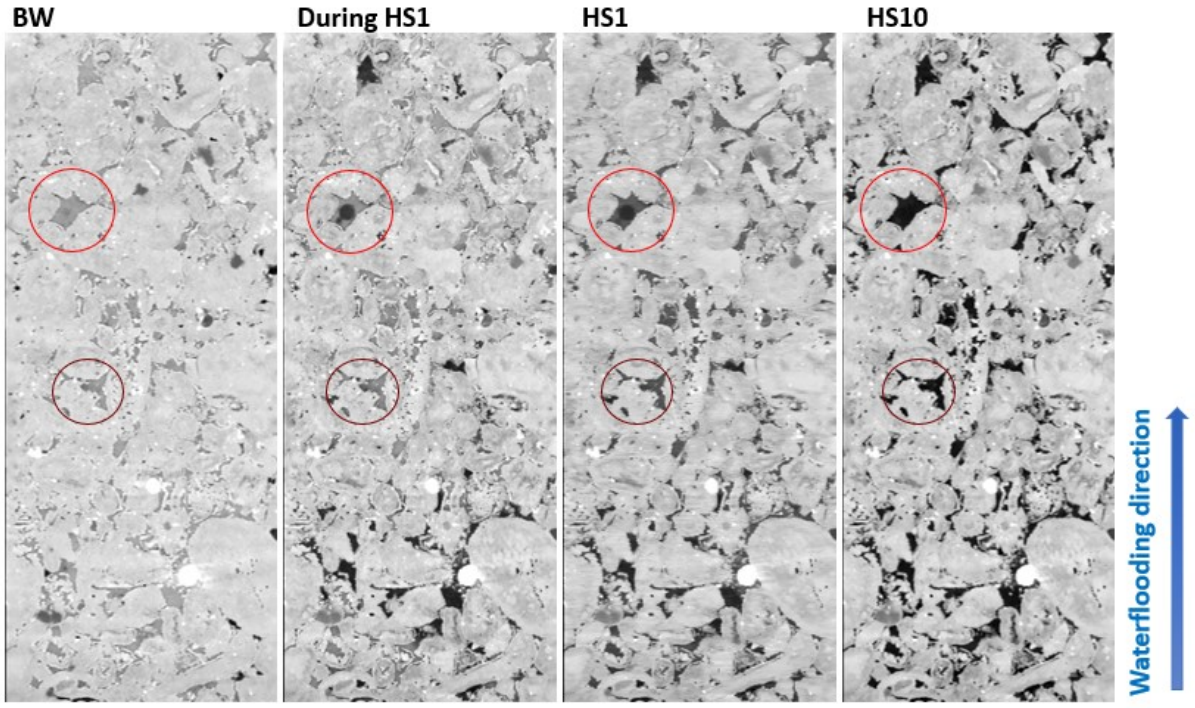

Figure 9.15: Cross-section of the reservoir sample tomogram during HS waterflooding (Ch. 6) showing the slower emulsification in the area further away from the inlet.

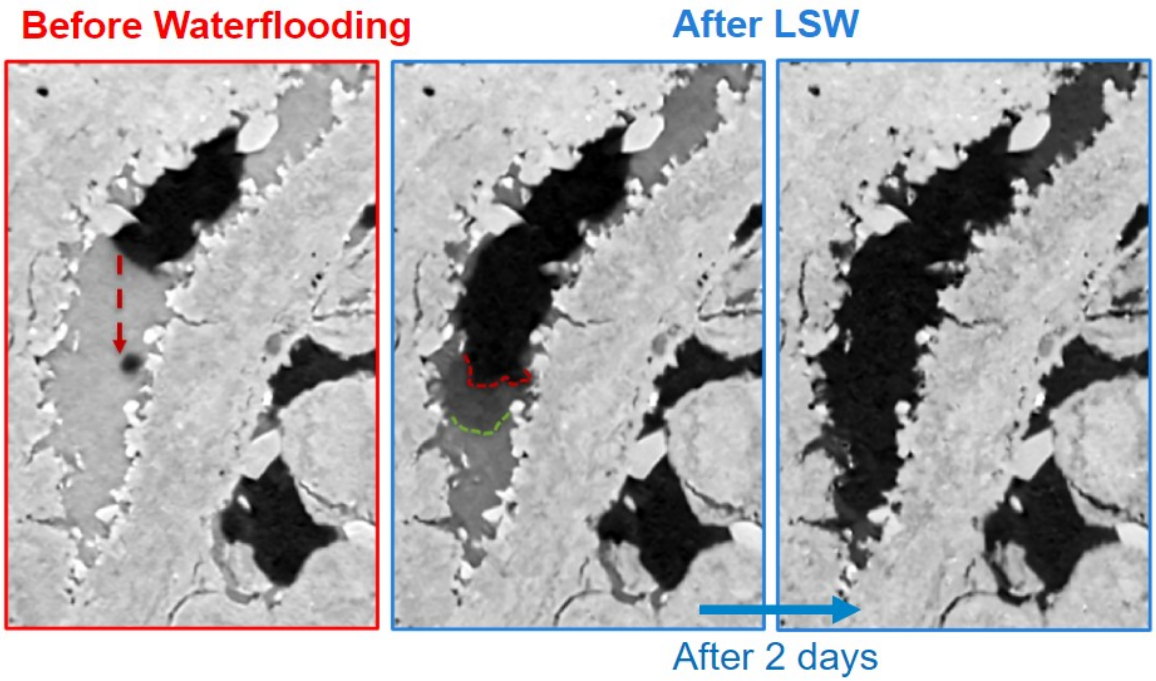

Figure 9.16: Cross-section from the reservoir sample tomogram showing the development of emulsion phase (dark grey) between the oil (light grey) and brine (black) during LS waterflooding.